

The impact of surface dust source exhaustion on the martian dust cycle, dust storms and interannual variability, as simulated by the MarsWRF General Circulation Model

Claire E. Newman*, Mark I. Richardson

Ashima Research, Suite 104, 600 South Lake Avenue, Pasadena, CA 91001, USA



ARTICLE INFO

Article history:

Received 25 March 2014

Revised 24 February 2015

Accepted 25 March 2015

Available online 16 April 2015

Keywords:

Mars

Mars, atmosphere

Mars, surface

Atmospheres, dynamics

Mars, climate

ABSTRACT

Observations of albedo on Mars suggest a largely invariant long-term mean surface dust distribution, but also reveal variations on shorter (seasonal to annual) timescales, particularly associated with major dust storms. We study the impact of finite surface dust availability on the dust cycle in the MarsWRF General Circulation Model (GCM), which uses radiatively active dust with parameterized 'dust devil' and wind stress dust lifting to enable the spontaneous production of dust storms, and tracks budgets of dust lifting, deposition, and total surface dust inventory. We seek a self-consistent, long-term 'steady state' dust cycle for present day Mars, consisting of (a) a surface dust distribution that varies from year to year but is constant longer-term and in balance with current dust redistribution processes, and (b) a fixed set of dust lifting parameters that continue to produce major storms for this distribution of surface dust. We relax the GCM's surface dust inventory toward this steady state using an iterative process, in which dust lifting rate parameters are increased as progressively more surface sites are exhausted of dust. Late in the equilibration process, the GCM exhibits quasi-steady state behavior in which few new surface grid points are exhausted during a 60 year period with constant dust lifting parameters. Complex regional-scale dust redistribution occurs on time-scales from less than seasonal to decadal, and the GCM generates regional to global dust storms with many realistic features. These include merging regional storms, cross-equatorial storms, and the timing and location of several storm types, though very early major storms and large amounts of late storm activity are not reproduced. Surface dust availability in key onset and growth source regions appears vital for 'early' major storms, with replenishment of these regions required before another large storm can occur, whereas 'late' major storms appear primarily dependent on atmospheric variability. For the parameter space explored, no simulation achieves a steady state with continuing major storms lasting longer than 60 years when a constant wind stress lifting threshold is used. However, such a long-term steady state is achieved when a variable threshold is introduced, in which the threshold increases as dust is removed. This negative feedback on lifting slows it sufficiently for a balance to be produced between dust removal and re-deposition, even in key source regions for major storms. One concern is that the long-term surface dust distributions produced in these simulations show significant differences to the observed northern hemisphere albedo map, in particular predicting Tharsis and NE Arabia to be relatively dust-free. Although some observed high albedo regions may not have significant mobile dust, others likely have a dust cover several meters thick. The mismatches may reflect deficiencies in the GCM or the iterative process used, or the existence of ancient deep dust deposits formed during a past climate epoch.

© 2015 Elsevier Inc. All rights reserved.

1. Introduction

The distribution of dust in the martian atmosphere is a major modifier of atmospheric heating and thus the entire circulation.

Atmospheric dustiness is determined by the balance between lifting and sedimentation, which changes over the course of a Mars year (henceforth this will be referred to simply as 'year') to yield a distinct seasonal cycle of dust loading. The mechanisms controlling this cycle, especially those associated with very large dust lifting events (major dust storms), are poorly understood, and as such it cannot yet be predicted with confidence. Given this, most current Mars General Circulation Models (GCMs) prescribe either

* Corresponding author.

E-mail addresses: claire@ashimaresearch.com (C.E. Newman), mir@ashimaresearch.com (M.I. Richardson).

the two-dimensional (zonally uniform) or three-dimensional atmospheric dust distribution (e.g. Lewis et al., 1999; Montmessin et al., 2004; Guzewich et al., 2013a), or the pattern of surface dust lifting (e.g. Kahre et al., 2009), as a function of season. These prescriptions are typically based upon either observations of the dust distribution or observations of temperature or radiance. In the latter cases the atmospheric or injected dust distribution is set such that the simulated temperatures or radiances match those observed. A prescribed approach provides the best means of forcing GCMs such that they simulate realistic circulations, and may also be used to infer aspects of the dust cycle, such as diagnosing where dust was likely injected (Kahre et al., 2009). However, a prescribed approach has two major disadvantages: (1) it offers almost no insight into the mechanisms that regulate net dust gains or losses at a particular grid point, and (2) there is no predictive component to the dust cycle. The lack of prognostic capability means that such models are of limited use with data assimilation systems, in Mars weather prediction studies, or in studies of paleoclimate.

The alternative is to simulate the dust cycle by parameterizing its key processes: dust lifting from the surface, mixing and transport within the atmosphere, and sedimentation through the atmosphere and (ultimately) back to the surface (e.g. Murphy et al., 1990; Wilson and Hamilton, 1996; Newman et al., 2002a,b, henceforth N02a,b; Basu et al., 2004, 2006, henceforth B04,06; Kahre et al., 2005, 2006, 2008, henceforth K05,06,08; Wilson and Kahre, 2009, henceforth WK09; Mulholland et al., 2013, henceforth M13). If these processes are parameterized correctly, a GCM should be able to spontaneously and self-consistently produce the observed range of dust cycles and dust storms, predict future dust activity, and more reliably predict how dust activity may have differed in the past. To date, however, no GCM using parameterized dust processes has reproduced all aspects of the observed dust cycle. In addition, in simulations in which the surface dust abundance is treated as finite – i.e., as an expendable rather than unlimited resource – no GCM has achieved a realistic steady state dust cycle without including an *ad hoc* dust resupply term and limiting the peak dust opacities allowed [WK09; M13; Section 5].

1.1. Observations of the martian dust cycle

There are three main observational constraints for the martian dust cycle: (a) the seasonal variation of dust opacity and air

temperature that describes the ‘background’ cycle; (b) the pattern, timing, evolution, and intermittency of large storm events; and (c) the evolution of surface dust deposits as revealed by mapping of surface property variations (such as spectral signatures, albedo, and/or thermal inertia). Each is used to evaluate model results, thus we provide a brief review of relevant observations here.

1.1.1. The background dust cycle

Following B04, we define the ‘background’ dust cycle as the variation of optical depth and air temperature in the absence of regional and global dust storms, which is rather repeatable from year to year (e.g. Colburn et al., 1989; Richardson, 1998; Smith, 2004). This cycle involves the well-known clearer, cooler northern spring and summer and the dustier, warmer southern spring and summer (see Fig. 1). To assess the realism of dust loading in our simulations, we use the ‘global T15’ metric based on mid-level air temperature weighted at ~25 km or ~50 Pa, as described further in B04 and Section 2.3. It is arguable whether it is better to use air temperature or dust optical depth for this purpose. A match to observed air temperatures suggests the modeled dust distribution is producing realistic radiative forcing and circulation response, which is key to realistic dust lifting, transport and deposition, and hence surface dust rearrangement. However, temperatures may also be strongly affected by aerosols not considered in this work, in particular water ice clouds in northern spring and summer. A good match to observed dust optical depths provides a more direct comparison. However, these datasets are generally sparser and noisier and involve a less certain retrieval process. Most importantly, a match to observed dust optical depths does not guarantee a match to the real radiative forcing, since this depends on the dust radiative properties in the model, which may be different to those in the real atmosphere. Since we are most interested in capturing the radiative forcing and circulation response correctly, we thus choose an air temperature metric here.

1.1.2. Dust storms

In this paper we define ‘major dust storms’ to include storms that show up as significant perturbations in zonal- and global-mean opacities or air temperatures, which thus includes ‘large regional storms’ as well as ‘global storms.’ We define ‘large regional storms’ as storms that raise dust opacities over most longitudes but over a limited latitude range, and raise global T15 values by 5–10 K above background levels (see Section 2.3). We define

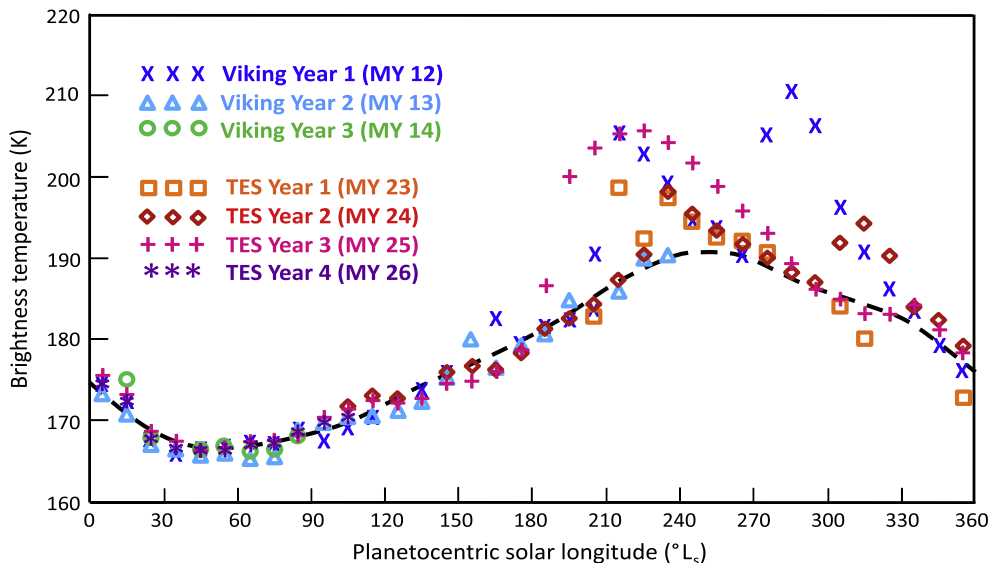


Fig. 1. Observed ‘global T15’ curves for nearly 7 Mars years, adapted from B04. See text for details.

'global storms' as storms that expand to cover all longitudes over a large latitude range involving both hemispheres, and produce sustained global T15 values >210 K. Realistic simulations should yield overall storm statistics similar to those observed in terms of range of onset times and locations, size and duration, and patterns of evolution. They should also reproduce the observed extent of inter-annual variability in storm type and activity. This variability is rather large, as discussed below, thus statistics on large storm behavior are limited by the extent of the observational record. As such, the large storm constraints are less complete than those imposed by the background dust cycle.

A thorough review of all telescopically-observed dust storms until 1993, plus the Mariner 9 and Viking Orbiter observations of the 1971 [MY9] and 1977 [MY12] global storms, is provided by McKim (1999), with a more concise review in Martin and Zurek (1993). Here we follow the Clancy et al. (2000) convention of Mars years ('MY'), with MY1 defined as the first Mars year in which a global storm was observed in significant detail by astronomers (1956). Smith (2004, 2009) provide a review of dust opacity observations from 1999 to 2008 [MY 24–29] by the TES and THEMIS instruments on respectively the MGS and Odyssey spacecraft. Strausberg et al. (2005), Cantor (2007) provide a detailed description of the 2001 [MY 25] global storm as observed by MGS MOC, while Wang and Richardson (2013) (henceforth WR13) describe the 2007 [MY 28] global storm as observed by MRO MARCI. Cantor et al. (2001), Wang et al. (2003) and WR13 provide details of regional and local storms observed by recent spacecraft. Whereas some local storms and dust devils occur year round, global and large regional storms have only been observed in southern spring and summer, from $L_s \sim 180^\circ$ to 360° , where L_s is areocentric solar longitude. Here we refer to this period as the 'storm season.'

No global storms have yet been confirmed to begin solely in the northern hemisphere, though cross-equatorial or 'flushing' regional storms (see below) propagating from north to south sometimes occur just prior to major storms. Also, significant dust lifting is likely triggered in the north during a global storm's growth phase. Prior to the MY 25 storm (which began at $L_s \sim 184^\circ$), the earliest global storm was observed to begin at $L_s \sim 204^\circ$ in MY 12, with most occurring between $L_s \sim 240^\circ$ and the end of the storm season. Prior to MY 25, all storms lasting >120 sols were observed to begin either early in the storm season ($L_s \sim 200$ – 210°) or near solstice ($L_s \sim 260$ – 270°), though short-lived storms began between these periods in other years. Global storms appear to occur in roughly a third of the years that have been sufficiently well observed. In terms of global storm onset, the general Hellas (~ 30 – $100^\circ E$, 30 – $60^\circ S$) and Thaumasia (~ 60 – $120^\circ W$, 30 – $60^\circ S$) regions of the southern mid-latitudes appear to dominate. Hellas may be a favored location due to the combination of seasonal cap circulations and topographic forcing along the basin rim.

Regional storms are more common than global ones. They may include a population that are simply failed global storms (i.e. of similar dynamical origin but smaller in size), but the mechanisms determining maximum size remain unknown. No two storms are exactly alike, and the number observed in detail is still rather low. However, WR13 provide a summary of the initiation and evolution of 65 large storms imaged by MOC and MARCI from MY 24–30. They note several 'families' of storms that follow specific patterns and can be differentiated according to their onset location, evolution, and season of occurrence. All but two of the storms originating in the northern hemisphere are observed in two seasonal windows at $L_s = 180$ – 240° and $L_s = 305$ – 350° , while all but two of those originating in the southern hemisphere are observed during $L_s = 135$ – 245° . Locations of preferred storm origination include Acidalia, Utopia and Arcadia in the northern hemisphere, and Hellas in the south. 'Flushing' type storms dominate northern hemisphere storm activity, and develop primarily in Utopia

Isidis and Acidalia–Chryse, with smaller storms in Arcadia–west of Tharsis (Cantor et al., 2001; WR13). They appear to begin in association with cap winds or baroclinic fronts in northern autumn, winter and early spring, then to travel or expand primarily north–south in three meridional 'channels' between the Tharsis, Syrtis, and Elysium regions of higher topography. This localization is consistent with a Western Boundary Current (WBC) intensification of the low-level 'monsoonal' southern summer return flow of the Hadley circulation here (Joshi et al., 1997). Moving south into the monsoonal flow from their onset region appears to require constructive interference between low pressure weather systems and the thermal tide (Wang et al., 2003, 2005). Unlike the northern storms, the expansion of southern storms appears to be largely east–west [WR13]. Storm sequences that overlap in time, such as flushing and southern hemisphere storms, often grow into larger scale events.

1.1.3. Surface dust variability

The variation of surface dust is less well constrained than that of atmospheric dust or temperature. However, using albedo as a proxy for dust cover, Szwast et al. (2006) showed that there was little large-scale change between the Viking (1970s) and MGS (2000s) time periods, although some small scale albedo features have evolved in shape (Geissler, 2005; Szwast et al., 2006; Cantor, 2007). Surface dust cover changes due to a major storm can be significant, temporarily brightening the surface in a global mean sense. Surfaces with generally high albedo are not brightened significantly by fresh dust fall, whereas generally dark surfaces that brighten as a result of storm fallout can result in regional temperature changes of several K (Smith, 2004), and global mean surface temperature increases of over 0.5 K (Fenton et al., 2007). However, claims of net decadal darkening and warming of Mars (Geissler, 2005; Fenton et al., 2007) appear to have resulted from misinterpreting short-period albedo changes (associated with dust storms) as long-period ones. Detailed analysis suggests that the highly modified dust cover in the wake of major storms typically relaxes to pre-storm patterns in less than a year, in some cases within weeks or months of the storm's end (e.g. Szwast et al., 2006). This apparent rapid stabilization is consistent with a roughly repeatable annual atmospheric dust cycle on Mars when averaged over several years. Other datasets relevant to surface dust cover include thermal inertia maps and the Dust Cover Index (DCI) (Ruff and Christensen, 2002). The DCI exploits a short wavelength feature of TES spectra, in which relatively strong absorptions are attributed to the presence of surface silicate particles much smaller than 100 μm in diameter. It is more direct than thermal inertia or albedo measurements, with a high (low) DCI indicating relatively dust-free (dust-covered) surfaces.

1.2. Prior numerical modeling of dust storms and cycles

Early modeling studies focused on the impact of a prescribed dust distribution on the atmospheric state, or the evolution of storms initiated via prescribed dust lifting, using a range of tools from analytical models to three-dimensional GCMs (Gierasch and Goody, 1973; Schneider, 1983; Murphy et al., 1990, 1993, 1995; Wilson and Hamilton, 1996).

1.2.1. Results of previous modeling assuming infinite surface dust

As understanding grew, and increases in computing power enabled longer and more complex simulations, efforts shifted to the prediction of dust storms and the dust cycle using parameterized dust lifting, sometimes called 'interactive dust' [N02a,b; B04,06; K05,06; M13]. In this case, model winds and the near-surface thermal state are used to predict the dust lifted at all times and locations, after which the lofted dust is transported

by the atmospheric circulation as it gradually falls out. If these simulations are also ‘radiatively active,’ complex non-linear behaviors and feedbacks are possible due to coupling between atmospheric dust and the model’s radiative transfer scheme (i.e., the heating and cooling of the atmosphere and surface), which in turn modifies the circulation and hence the near-surface winds and thermal structure. The specific dust lifting parameterizations used in our model, MarsWRF, are described in Section 2.2. However, the basic approach taken by most modelers can be summarized as follows: (a) background dust lifting, sometimes called ‘dust devil’ or ‘small scale convective’ lifting, is set proportional to a function containing variables such as the surface sensible heat flux and boundary layer thickness, with the main parameter being a constant of proportionality (which scales the dust devil lifting rate); and (b) above a chosen wind stress threshold, dust lifting due to model-resolved winds is set proportional to a function of density, wind stress and threshold, with the main two parameters typically a constant of proportionality (which scales the wind stress lifting rate) and the threshold wind stress.

N02a,b used the Oxford Mars GCM with a combination of dust devil and wind stress lifting to produce self-consistent, multi-annual dust cycles. These contained spontaneous dust storms, including flushing storms, but had limited interannual variability in major storm types. In addition, positive feedbacks between dustiness and wind stress lifting led to ‘runaway’ global storms with unrealistically high opacities, causing the radiative transfer scheme to crash whenever a global storm was produced. MarsWRF simulations using the Oxford GCM’s vertical layers (not shown) suggest that small layer thicknesses near the surface may have led to this instability. M13 (using a later version of the same GCM) note that they shut off dust lifting for columns with optical depth >10 to maintain model stability, perhaps to mitigate this issue if the same vertical layers were used.

Using the GFDL SKYHI Mars GCM, B04,06 were able to extend these results, producing a more complete spectrum of dust cycle behavior that also included the stable simulation of interannually-varying global dust storms when very high (0.052–0.058 Pa) wind stress thresholds were used. However, their model could not produce global storms early in the storm season ($L_s = 180\text{--}240^\circ$). In addition, their global storms continued until the end of the storm season when a seasonal “spin down” of the circulation occurs as equinox nears, in conflict with observations of storms shutting down much earlier.

Using the NASA Ames Mars GCM, K06 were able to reproduce an annual dust cycle similar to that of N02a,b and the lower stress threshold simulations of B04,06. K06 also examined the high stress region of parameter space, but unlike B04,06 found no increase in storm interannual variability, and noted that their local dust storm statistics deviated significantly from those observed (Cantor et al., 2001) if such high thresholds were used.

1.2.2. Rationale for using finite surface dust when modeling the dust cycle

The N02a,b, B04,06, and K06 studies all assumed an infinite abundance of surface dust. However, in all of these simulations the primary source regions experienced far more dust loss (via lifting) than dust gain (via fallout), as demonstrated in Section 3.3.2. This suggests that in reality the key dust source regions would have been exhausted over time, unless a massive dust deposit existed there to begin with (a possibility we discuss in Section 5.1). Thus it is clear that in many regions – particularly those with high wind stress thresholds – the assumption of infinite surface dust may result in huge biases if dust is continuously lifted from surfaces that are basically permanently dust-free on Mars.

The inability to capture temporary lack of dust availability will cause biases too. On Mars, the atmosphere is capable of

resupplying sufficient dust to markedly brighten many generally dark surfaces on sub-annual time scales (Christensen, 1988; Geissler, 2005; Szwast et al., 2006; Geissler et al., 2008). Thus replenishment of dust to such regions likely plays a role in permitting storm onset, and/or in increasing the size or duration of storms when they occur. Szwast et al. (2006) describe significant clearing of dust from Daedalia, a major source region (Strausberg et al., 2005) during the MY25 global storm, and ask whether a global (rather than only regional) storm might have developed in MY26 too had surface dust availability not been greatly depleted in the previous year.

Fundamentally, if no region can be exhausted of dust this means that an implicit artificial replenishment mechanism is at work, effectively resupplying regions that would otherwise experience net loss. The existence of this ‘hidden’ resupply mechanism means that the atmosphere plus surface dust distribution is not in a *self-consistent* long term steady state. Note that here we define a long term steady state as one in which the short-term mean surface dust distribution (averaged over several years to remove inter-annual variability effects) does not vary over a much longer period (decades to centuries).

1.2.3. Why re-tuning the dust parameters is necessary when using finite surface dust

The dust cycles in all interactive dust Mars GCMs are ‘tuned’ in some way, meaning that their free parameters – such as those described in Section 1.2.1 – are adjusted until the simulated dust cycle shows the best match to that observed on Mars itself. Section 2.3 describes the tuning process used in MarsWRF to find the best fit dust lifting parameters for a given threshold choice. If only a fraction of the surface has dust available, however, it should be obvious that the lifting rate parameters will need to increase and/or the threshold decrease to produce the same amount of dust lifting globally. If a simulation is begun with uniform but limited surface dust and surface regions are allowed to deplete, then the best fit dust lifting parameters will change over time. I.e., once several source regions have been exhausted (either permanently or e.g. in certain seasons), the best fit parameters will be very different to those when dust was available everywhere at all times.

1.2.4. Results of previous modeling assuming finite surface dust

K05 and M13 both found that if the surface were initialized with a uniform, finite amount of dust, the primary source regions were rapidly exhausted, causing dust storms to cease after only a few Mars years. Increasing the initial dust cover did not affect the final result, merely the time required to reach it. M13 concluded that model limitations or lack of small-scale process parameterizations prevented a steady state from being found. They suggested that GCM biases in the frequency of simulated southern global storms versus northern cross-equatorial storms resulted in more net south-to-north transport than occurs on Mars. To compensate, they included an *ad hoc*, globally-uniform dust resupply scheme, tuned such that major dust storms would continue to occur roughly every three years. The implications of such a scheme are discussed in Section 5. However, M13 did not explore re-tuning the dust lifting parameters after regions of the surface had been exhausted (though they included a variable threshold parameterization, see Section 5.2).

K05 did explore restarting from the end of a ten-year simulation – during which many source regions had been exhausted – with an increased wind stress lifting rate parameter. Their intent was to see if the new primary source regions would be resupplied cyclically, unlike the original set. However, K05 found that they were not cyclically resupplied either, and did not continue past this point. Based on their results, K05 suggested that a steady state surface dust distribution does not exist on Mars. Instead, they suggested

that primary source regions do experience net dust removal over time, but are simply so deep that it does not matter; i.e., dust there is effectively infinite. In this scenario, most primary source regions would date from a past orbital epoch, one in which dust lifting and transport patterns were sufficiently different that net accumulation occurred where net removal occurs now. This in turn implies that the dust cycle closes on far longer timescales (see also the discussion in Section 5.1).

By contrast, albedo observations indicate that changes in surface dust availability over seasonal or annual timescales play a role in the current dust cycle, with both loss and replenishment occurring in many primary source regions for storms. For example, Daedalia was depleted (dark) when observed by Viking after the second MY 12 global storm, but was dusty again (bright) by the time it was observed again by MGS in MY 24; this dust cover was then almost completely removed during the MY 25 global storm, but showed signs of slow replenishment over the next two years (Szwest et al., 2006). And while Syrtis experienced significant brightening as a result of the MY 25 storm, this dust cover was largely removed, and the shape of Syrtis restored to its pre-storm shape by winds which are apparently common in late southern summer (Szwest et al., 2006). Much of the zonal band in the southern mid-latitudes that was low albedo in MY 24 was similarly brightened following the MY 25 storm and returned to near pre-storm values less than a year later (Szwest et al., 2006). These three examples, and many others, suggest that at least some major dust source locations are not ancient, and can be resupplied by natural variations within the current dust cycle over a few Mars years.

1.3. The goals of this work and structure of this paper

The main goal of this work is to test the hypothesis that a self-consistent long term steady state dust cycle exists for present day Mars, using the MarsWRF GCM as a proxy for real Mars. Such a dust cycle consists of (a) a finite surface dust distribution that varies from year to year but is constant in a long-term (~decadal) sense and in balance with current dust redistribution processes, and (b) a set of dust lifting parameters that produce continuing major storms for this distribution of surface dust. As described in Sections 1.2.3 and 4.1, dust lifting parameters are iteratively ‘re-tuned’ in the transient stages of our simulations, to compensate for the decrease in source region dust availability that occurs as surface dust is rearranged over time *en route* to its steady state distribution, at which point the parameters are held fixed. K05 performed one iteration of this type, but we argue that further iterations are needed to achieve primary source regions that are indeed cyclically resupplied. A preliminary attempt to do so was described in Newman (2001), while the bulk of this paper describes new work in which seventeen iterations were performed. Our other goal is to investigate the impact on – and realism of – dust cycles, storms and interannual variability when finite surface dust is used in MarsWRF.

In Section 2 we describe the MarsWRF GCM and provide details of the dust lifting parameterizations used. In Section 3 we demonstrate that MarsWRF produces regional and global dust storms and cycles with interannual variability when high wind stress thresholds and infinite surface dust are used. These baseline results are similar to B04,06 but differ from N02a,b and K06 (who failed to produce global storms and interannual variability, respectively). In Section 4 we present results from a *finite* surface dust simulation with a threshold wind stress of 0.02 Pa, and describe the difficulties in finding a steady state surface dust distribution with continuing major storms. We also examine the seasonal and interannual variability in the dust cycles, dust storms, and surface dust distribution produced during a quasi steady state period lasting ~60 years, and

compare these results with observations. In Section 5 we present results from a finite dust simulation in which the threshold varies according to surface dust cover, and show that a steady state solution with continuing major storms can then be found. Finally, in Section 6 we summarize our results, and present and discuss our conclusions.

2. Model description

2.1. The MarsWRF GCM v3.0.1.2

MarsWRF is the Mars flavor of planetWRF, a multi-scale planetary model developed from the widely-used Earth-based Weather Research and Forecasting (WRF) model (Skamarock et al., 2008). Details of its development are given in Richardson et al. (2007), Guo et al. (2009), Toigo et al. (2012), and Guzewich et al. (2013a). The simulations presented here were conducted using model version 3.0.1.2, with additional dust process parameterizations (see Section 2.2). As detailed in prior MarsWRF papers, this version includes a prognostic CO₂ cycle tuned to matched the Viking Lander pressure curves, and a ‘wide band model’ (WBM) radiative transfer scheme that follows algorithms in Haberle et al. (1982), Briegleb (1992) for dust, and Hourdin (1992), Forget et al. (1999) for CO₂, in the thermal infrared and solar bands, respectively. The WBM scheme is essentially identical to that used in the SKYHI GCM, thus this work and the B04,06 studies share common dependence of radiative heating on atmospheric dust opacity. However, while we model dust sedimentation (impacting the vertical dust distribution) using a single particle diameter of 4 μm (see Section 2.2.5), B04,06 used a two-particle scheme. Note that later versions of planetWRF include several improvements, such as more sophisticated radiative transfer options. However, the simulations shown here represent several Mars millennia of simulated dust cycles and were thus conducted over a long period of time, hence we used version 3.0.1.2 throughout for consistency.

2.2. Dust process parameterizations used in this work

Following N02a,b we parameterize dust lifting from the surface by two physical mechanisms: dust devils (Section 2.2.1) and near-surface wind stress (Section 2.2.2). The lifted dust is first injected into the lowest layer of the atmosphere then mixed by MarsWRF’s planetary boundary layer (PBL) scheme (Section 2.2.3), advected by GCM winds (Section 2.2.4), and sedimented downward under gravity (Section 2.2.5).

2.2.1. Lifting of dust via dust devils

N02a considered two parameterizations of lifting by dust devils. The best match to the seasonal cycle of background dustiness was given by a scheme utilizing the Renno et al. (1998) treatment of them as convective heat engines. We therefore use this scheme, in which dust lifting is set proportional to a ‘dust devil activity’ defined by Renno et al. as:

$$\Lambda \approx \eta F_s \quad (1)$$

where F_s is the surface sensible heat flux (the heat input to the base of the vortex) and η is the thermodynamic efficiency of the dust devil convective heat engine (the fraction of the input heat turned into work). The lifted dust flux, Q_{ddev} (in kg m⁻² s⁻¹), is given by:

$$Q_{ddev} = \alpha_D \eta F_s \quad (2)$$

where α_D is the dust devil lifting rate parameter (in units of kg J⁻¹). This formulation results in fluxes that increase predominantly with (a) the surface to air temperature difference, on which F_s largely

depends, and (b) the thickness of the convective boundary layer, with larger boundary layers resulting in larger η . Predicted dust devil lifting thus peaks in local summer, and is greatest in early afternoon when peak surface-to-air temperature gradients occur, as well as the most developed convective boundary layers.

The dependence on surface to air temperature difference results in a negative feedback on dust lifting by dust devils: in general, as more dust is lifted, the daytime atmosphere warms as more solar radiation is absorbed, while the surface cools as more solar radiation is blocked via absorption or scattering [N02a]. This response to increased dust loading is opposite to that produced during onset of storms, when dust lifting rapidly ramps up. In combination with observations showing no correlation between dust devils and dust storm occurrence (e.g. Cantor, 2007), this suggests that dust devils are key to the maintenance of the background dust cycle but do not contribute significantly to storms.

2.2.2. Lifting of dust via wind stress and saltation

N02a also considered two parameterizations of lifting by wind stress, both of which assumed that dust particles were lifted during saltation (lifting followed by rebounding to the surface) of more easily moved sand-sized particles above a given saltation threshold. The second parameterization included a representation of wind gustiness, which led to more widespread, less threshold-sensitive dust lifting. However, N02a found that any significant amount of gustiness resulted in too gradual dust storm onset compared to reality, hence we use the first parameterization in this work. The lifted vertical dust flux is set proportional to the horizontal saltation flux using the formula of White (1979):

$$Q_{\text{nsws}} = \max[0, \alpha_N(\rho/g)u_{\text{drag}}^3(1 - u_{\text{drag}}^t/u_{\text{drag}})(1 + u_{\text{drag}}^t/u_{\text{drag}})^2] \quad (3)$$

where ρ is near-surface air density, g is acceleration due to gravity, u_{drag} is the drag (friction) velocity at the surface, u_{drag}^t is the threshold drag velocity required for saltation to occur, and α_N is the dimensionless wind stress lifting rate parameter. (Note that there is a typographical error in White's equation 22; the above follows White's equations 11–19 in which the form of the flux equation is derived.) The drag velocity is defined as:

$$u_{\text{drag}} \cong (\tau/\rho)^{1/2} \quad (4)$$

where τ is the wind stress at the surface and ρ is the air density. τ is calculated in MarsWRF's surface layer parameterization, which links the net eddy stress (and fluxes of momentum, heat and tracers) to model-resolved winds and the thermal structure in the surface layer. The parameterization used for these simulations is the original version of the WRF SFCLAY Monin–Obukhov scheme (Jimenez and Dudhia, 2012). The surface layer is defined as the lowest portion of the atmosphere in which the fluxes are invariant with height (practically, where they vary by less than about 10% in magnitude). The roughness length scale, z_0 , for the stress calculation comes from MOLA pulse width maps generated by Garvin et al. (1999), as discussed in detail by Heavens et al. (2008). B04,06 and K05,06 used a globally uniform, constant threshold wind stress, τ^t , converted to threshold drag velocity via $u_{\text{drag}}^t = (\tau^t/\rho)^{1/2}$. N02a instead used a globally uniform, constant saltating particle size and interparticle cohesion, then found u_{drag}^t via a set of iteratively-solved semi-empirical equations. However, the spatio-temporal variation in u_{drag}^t found using both methods was nearly identical, thus we use the simpler (constant τ^t) approach here.

Unlike dust devils, wind stress lifting generally has a strong positive feedback response, both on local scales (as thermal gradients and hence winds increase at the edge of dust clouds) and in a global sense (as the global circulation intensifies for large dust loadings), see e.g. N02a. This response is in line with the rapid

onset of dust storms, suggesting that wind stress lifting is largely responsible for them.

2.2.3. Dust vertical mixing

We use WRF's 'MRF PBL' scheme (named after the model in which it was first used), as described in Hong and Pan (1996). The scheme includes both local and non-local mixing, and uses the following equation for the mixing of a tracer C :

$$\partial C / \partial t = \partial / \partial z [K_c (\partial C / \partial z) - \gamma_c)] \quad (5)$$

where K_c is the eddy diffusivity coefficient and γ_c is a correction to the local gradient term designed to incorporate the contribution of large-scale eddies to the total flux (i.e., the impact of non-local deep mixing). Within the boundary layer, K_c and γ_c both depend on the atmospheric stability, and γ_c also depends on the surface tracer flux. Above the boundary layer, however, only local mixing occurs, K_c is roughly proportional to the vertical wind shear, and $\gamma_c = 0$. Note that using the MRF PBL vertical mixing scheme removes the need for a 'convective adjustment' scheme, as it already deals with the effect of instability on mixing and vertical gradients, and does so in a more physical manner.

A more realistic parameterization of non-local mixing would require a representation of sub-grid scale processes, such as concentration of dust in plumes, solar absorption by dust during lifting, and the impact of steep topographic features on vertical velocities (see e.g. Rafkin et al., 2002; Michaels et al., 2006; Goldenson et al., 2008; Davy et al., 2009; Heavens et al., 2011; Rafkin, 2012). Observations of the vertical dust distribution (Heavens et al., 2011; Guzewich et al., 2013b) indicate elevated dust maxima, suggesting a much larger amount of non-local dust mixing than predicted by MRF PBL. However, since parameterizations of deep dust injection are still under development, we continue to employ the more restricted non-local mixing allowed by the MRF PBL scheme.

2.2.4. Dust advection

MarsWRF uses 5th order advection in the horizontal and 3rd order in the vertical. The advection scheme assumes that the distribution of tracers and wind within a grid cell can be represented by the grid cell value, an assumption that is nearly ubiquitous in Mars GCMs. Lian et al. (2012) recently demonstrated that more complex tracer advection schemes show significantly increased skill in capturing tracer transport, especially in regions of sharp tracer gradients. However, given the many other large uncertainties in modeling the dust cycle, and the fact that many of our simulations were completed before the Lian et al. (2012) study, we use only WRF's native advection scheme here.

MarsWRF is a finite difference model on a latitude-longitude grid. It thus has Fourier filtering as grid points converge (i.e., grid spacing shrinks) at high latitudes, to prevent numerical instability without the need for greatly reduced time steps. This filtering by definition smooths high latitude tracer fields. Similar filtering is required in dust studies using the SKYHI [B04,06] or Ames [K05] GCMs, but not in studies using the spectral-core Oxford GCM [N02a,b; M13] or the FMS GCM's cubed-sphere grid [WK09].

2.2.5. Dust sedimentation and deposition on the surface

Sedimentation of dust is controlled by the terminal velocity, which is calculated from the Stokes equation with the Cunningham correction for a rarefied atmosphere (Rossow, 1978) and assuming 4 μm particle diameter. The terminal velocities are applied to the dust tracers within an advection scheme that calculates the distance that a 'package' of particles, initially present in a given grid cell, will fall in the model timestep. The novelty of this scheme, written for the LMD GCM by Le Van, Hourdin, and Forget (Forget et al., 1999), is that it implicitly allows advection

Table 1

MarsWRF's vertical structure shown as the eta coordinate (see Section 2.4 for details) at the middle of each model layer, from the layer nearest the surface (layer 1) to the uppermost layer (layer 20).

Model layer	Mid-layer eta value	Model layer	Mid-layer eta value
1	0.9817	11	0.03622
2	0.9290	12	0.01847
3	0.8427	13	0.008049
4	0.7265	14	0.002813
5	0.5897	15	8.863×10^{-4}
6	0.4426	16	3.450×10^{-4}
7	0.3032	17	1.525×10^{-4}
8	0.1910	18	6.500×10^{-5}
9	0.1137	19	2.985×10^{-5}
10	0.06548	20	9.850×10^{-6}

across multiple layers in one timestep. This scheme was used in the Oxford GCM by N02a,b since 4 μm particles could fall over 5 m in a roughly 300 s time step, which exceeded the depth of the lowest level in that GCM (Lewis et al., 1999). In early MarsWRF simulations we also used this 25-layer structure, but subsequently adopted the 20-layer structure used in B04,06 (see Table 1) in which the lowest level is significantly deeper, thus fall through multiple layers in a single time step is no longer possible. However, the more complex scheme was retained to avoid unnecessary changes to the physical parameterizations between simulations.

2.3. Calibration procedure for all MarsWRF dust cycle simulations

As detailed in Sections 2.2.1 and 2.2.2, there are three free parameters involved in our dust lifting parameterizations: dust devil and wind stress lifting rate parameters, α_D and α_N , respectively, and threshold wind stress for lifting, τ_t . As in B04,06 we calibrate the model by adjusting these parameters until we produce the best match between our simulated 'global' T15 temperature cycles and those observed on Mars. Here T15 refers to the broad-band atmospheric (15 μm) channel of the Viking Orbiter Infrared Thermal Mapper (IRTM) instruments (Martin and Kieffer, 1979). This channel measured temperatures over roughly the altitude range 10–40 km, centered at ~25 km and ~50 Pa. It is possible to directly synthesize T15 from TES radiance observations (e.g. Liu et al., 2003; B04), thus a long baseline of direct (non-retrieved) observations is available as a summary reference for targeting simulations. The full rationale for choosing this 'brightness temperature' metric was discussed in Section 1.1.1.

Synthetic T15 values are generated from the GCM using the IRTM T15 weighting function, following Wilson and Richardson (2000). Here we define 'global T15' as T15 values averaged over the day-night cycle and (with area weighting) over the region 40°S to 40°N. Fig. 1 shows global T15 curves for almost 7 Mars years of observations by Viking and TES. Also shown is the 'climatological background' – effectively the global T15 curves with storm peaks removed – giving a hypothetical year with no major storms.

Following B04,06, we assume that the background dust load is produced entirely by dust devils, and that wind stress lifting is primarily responsible for producing storms. We therefore calibrate the dust devil lifting by running MarsWRF with $\alpha_N = 0$, and find α_D such that simulated global T15 curves match the climatological background. We next calibrate the wind stress lifting by choosing a value of τ_t and running MarsWRF with both dust devil and wind stress lifting activated, then adjusting α_N until simulated global T15 curves fall within the observed range of peak dust storm values. We finally repeat this procedure for different τ_t values until we obtain the best match to reality in terms of the observed extent

of interannual variability, range of storm onset times and locations, etc. In finite dust simulations this calibration procedure is greatly extended by the need to retune the lifting rates as surface grid points are exhausted of dust (see Section 4.1).

A major assumption here is that the wind stress threshold and both lifting rate parameters are globally uniform, whereas in reality they would likely vary spatially too. For example, running the GCM at much higher horizontal resolution better captures strong mesoscale circulations in some regions, impacting the fraction of winds exceeding threshold by a given amount (Toigo et al., 2012). A more sophisticated parameterization could attempt to vary α_N spatially to account for this, but is beyond the scope of this work.

2.4. Model setup

The simulations described in this paper use a regular latitude-longitude grid with a grid spacing of 5.625° in longitude and 5° in latitude. The vertical grid is defined in eta coordinates, where $\text{eta} = [P - P_{top}]/[P_{surf} - P_{top}]$, and P_{top} and P_{surf} correspond to the pressure at the model top and at the surface, respectively. However, P_{top} is sufficiently small that the coordinate is effectively sigma, where $\text{sigma} = P/P_{surf}$. We use the same vertical grid spacing as in the 20-layer SKYHI GCM [B04,06], shown in Table 1. It provides rather uniform resolution across the domain in terms of layer thickness in meters. The layers are thinner in the boundary layer, but without the very thin lowest layers used in the 25-layer Oxford Mars GCM, which were likely the primary cause of instabilities found by N02a,b during rapid storm growth. Such thin layers near the surface violate the basic assumption of PBL parameterization, i.e., that the surface layer is contained within the lowest model layer (e.g. Shin et al., 2012), although the relevant definition of the surface layer for Mars may imply that the daytime surface layer does remain very shallow (Sorjan et al., 2009).

All simulations are initialized from states previously 'spun up' both dynamically and in terms of the seasonal cycle of CO₂ (pressure). Simulations are generally run for at least a decade with constant dust lifting parameters to determine the extent of dust storm interannual variability, although their duration varies significantly as described in the text.

3. Results using infinite surface dust

Our main interest here is the effect of a finite surface dust supply on the martian dust cycle. In this section, however, we first briefly show MarsWRF results for infinite surface dust. These results provide a baseline for when dust availability is not a factor (e.g. the location of primary source regions and extent of interannual variability), and allow us to compare MarsWRF's 'infinite' dust cycles with those produced using other GCMs.

3.1. Dust cycles and storms in MarsWRF using infinite surface dust

As described in Section 2.3, we first ran MarsWRF with only dust devil lifting to calibrate the dust devil lifting scheme, giving $\alpha_D = 2 \times 10^{-9} \text{ kg J}^{-1}$, before turning on wind stress lifting. Using infinite surface dust, B04,06 produced global dust storms and significant interannual variability for high wind stress thresholds, in the range 0.052–0.058 Pa. We performed a series of experiments for τ_t ranging from 0.04 to 0.06 Pa to explore a similar high threshold regime. For $\tau_t = 0.04\text{--}0.046$ Pa, as α_N is increased the simulated dust cycle transitions from no storms to storms with reasonable global T15 to storms with overly high global T15. An example is shown in Fig. 2 for $\tau_t = 0.044$ Pa. Each α_N increase only affects southern summer, consistent with the fact that only then are wind

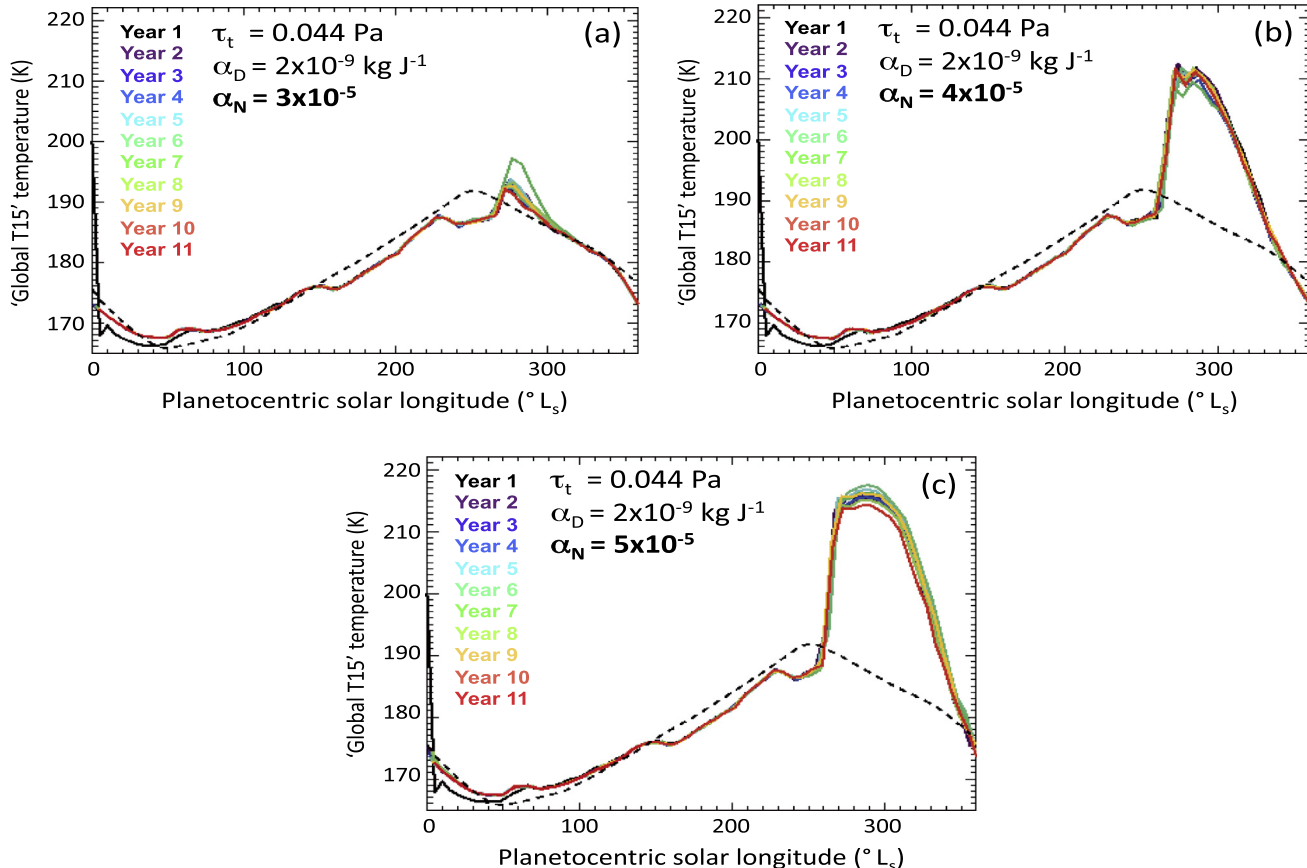


Fig. 2. ‘Global T15’ temperatures (see text) for three 10-year simulations showing the effect of increasing the wind stress lifting rate parameter, α_N , with the dust devil lifting rate parameter, α_D , and wind stress threshold, τ_t , held constant. The dashed line shows the observed climatological background (see text).

stresses strong enough to exceed these relatively large τ_t values sufficiently often. The resulting storms begin abruptly and only ‘spin down’ as the strong southern summer circulation weakens on the approach to equinox. Increasing α_N greatly increases the amount of dust lifted and hence peak air temperatures in southern summer, with the response to even a small increase being magnified by the positive feedbacks discussed in Section 2.2.2. However, for a given value of α_N there is no significant interannual variability, with MarsWRF’s dust cycle repeating almost identically each year.

For $\tau_t = 0.046\text{--}0.049$ Pa, however, MarsWRF produces significant dust cycle interannual variability for certain ranges of α_N . Fig. 3 shows results for $\tau_t = 0.047$ Pa and $\alpha_N = 3, 4$ and 5×10^{-5} . Although τ_t is only 6% higher than in the simulations shown in Fig. 2, this is enough to enter the variable global storm regime. For the smallest α_N value (Fig. 3a), global storms occur in 3 out of 10 years with no storm activity in other years. For the intermediate value (Fig. 3b), similar sizes of global storms occur, but do so more often, in 8 out of 10 years. The largest α_N value (Fig. 3c), however, takes us out of the regime of variable global storms, with unrealistically large storms in all years. Simulations with $\tau_t > 0.049$ Pa produce either no global storms (for small α_N) or runaway global storms that reach extremely high global T15 and (typically) cause the simulation to crash (for larger α_N). When infinite surface dust is assumed, MarsWRF thus produces large interannual variability in global storms for high wind stress thresholds in the range 0.046–0.049 Pa. This is qualitatively the same result found by B04,06, but for slightly lower thresholds. The difference may reflect differences in the modeled range of surface wind stresses,

or may be due to slight differences in the dust parameterizations used.

3.2. The source of interannual variability in infinite surface dust simulations

Interannual variability in these simulations is due entirely to intrinsic atmospheric variability – i.e., the fact that the surface wind stress distribution is slightly different at the same L_s in different years. Such differences are typically small (other than those produced by dust storms themselves). For low thresholds, wind stress dust lifting is fairly common and widespread, and relatively small α_N values are needed to produce realistic peak global T15. In this case, small year-to-year differences in wind stress at any lifting site have little impact on the total amount of dust lifted at any time. However, as the threshold is increased, the number of lifting sites and frequency of lifting events decrease, and larger α_N values are needed to produce the same amount of total dust lifting and realistic global T15. Now year-to-year differences in wind stress at lifting sites have a far greater impact on the dust cycle. Positive feedbacks on wind stress lifting enhance this effect. For example, consider a grid point with the highest wind stresses in a given region, at which τ_t is not exceeded in one year but is briefly exceeded in the next. In the first year, no lifting occurs over the entire region. However, in the second year lifting occurs at this grid point, and – for large enough α_N – increases local temperature gradients and wind stresses enough to trigger lifting at nearby grid points which were previously below threshold, resulting in a large

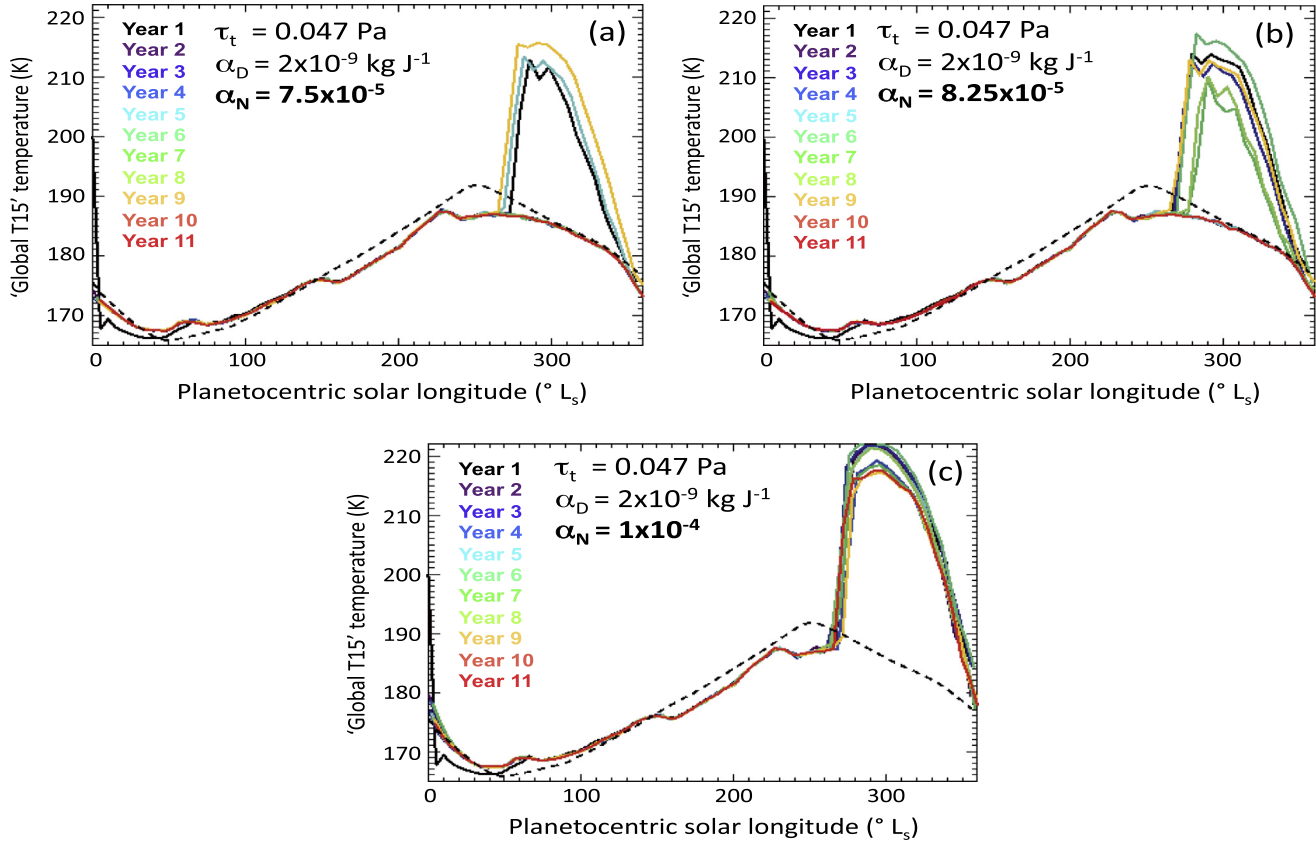


Fig. 3. As Fig. 2, but now demonstrating the impact of increasing α_N at a higher threshold, $\tau_t = 0.047 \text{ Pa}$. Figure (a) is our most realistic infinite surface dust simulation, referred to as simulation INFDUST.

dust lifting event. This explains why high τ_t combined with large enough α_N leads to interannual variability in dust storms.

3.3. Deficiencies of MarsWRF's infinite surface dust simulations

As in the previous studies described in Section 1.2.1, our infinite surface dust simulations capture some but not all aspects of the observed dust cycle, and also pose problems in terms of a long-term dust cycle because primary source regions are not replenished between storms and are depleted over time (Section 1.2.2). We briefly discuss these two deficiencies here, focusing on the simulation shown in Fig. 3a, henceforth referred to as INFDUST.

3.3.1. Unrealistic dust cycles

While some high threshold simulations, such as INFDUST, show significant interannual variability, they still capture only a fraction of the observed range of storm types, onset times, and sizes. All storms begin between $L_s \sim 265^\circ$ and 280° , with a maximum difference of only $\sim 10 \text{ K}$ in peak global T15 reached by different storms, whereas observed storms begin as early as $L_s \sim 184^\circ$ and show far more variability in size and onset time. If we reduce τ_t below 0.04 Pa (not shown), also reducing α_N to maintain realistic T15 values, then more wind stress lifting does occur earlier in the storm season. However, such simulations are very unrealistic in other respects: there is no interannual variability, and dust lifting increases far too gradually in southern spring, producing far smoother increases in dustiness and temperatures than observed. B06 produced slightly more variability in storm size and onset timing, yet still failed to reproduce several storm types or onset before $L_s \sim 240^\circ$. The range of storm types and onset regions is also much

smaller than observed. Figs. 4 and 5 demonstrate that a small number of grid points dominate wind stress lifting in INFDUST, representing a tiny fraction of the surface. This is inconsistent with observations indicating numerous and relatively widespread dust source regions, such as the significant lifting observed along the seasonal polar cap edge. Finally, as also found by B06, the larger simulated storms do not fully decay until the end of southern summer, rather than exhibiting the faster decay rates observed. In particular, lifting over Tharsis and Alba Patera continues long after the original source regions have shut down. A number of factors likely contribute to these deficiencies (see e.g. discussion in Section 4.6), though here we focus on the assumption of infinite surface dust.

3.3.2. Lack of primary source region replenishment

It is straightforward to demonstrate that the pattern of dust lifting in INFDUST could not be maintained long term without very deep deposits of source dust. Fig. 4 shows the mean wind stress lifting and change in surface dust over all 10 years of INFDUST. (Note that while we set a finite initial dust cover of 100 kg m^{-2} to allow us to track surface dust changes, this dust cover was effectively infinite since surface dust was never exhausted at any grid point.) The regions of peak wind stress lifting, on the northern slopes of the Hellas basin and Alba Patera, show up as areas of greatest net surface dust loss. Net loss also occurs over much of Tharsis and in a zonal collar from ~ 22 to 37°S , and at several longitudes from ~ 22 to 37°N . While there is net gain over the rest of the surface (peaking in central Hellas, to the east of the Alba Patera lifting sites, and poleward of $\sim 60^\circ\text{N}$), note that the contour intervals are 15 times smaller than the ones showing loss.

Fig. 5 focuses on the top dust contributors, showing the 100 surface grid points (out of 2304 total) responsible for contributing the

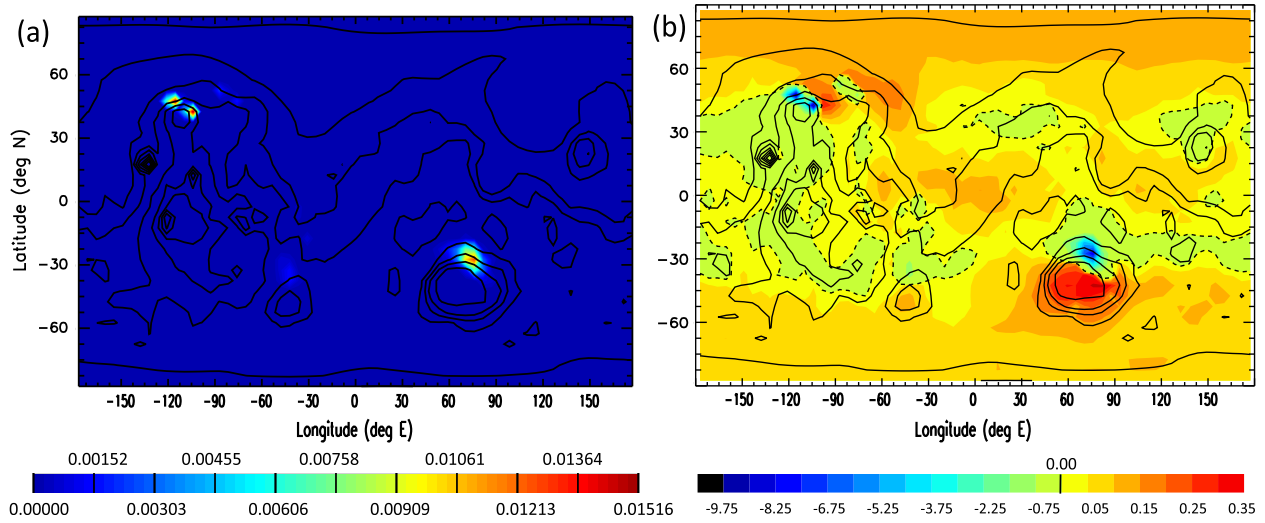


Fig. 4. (a) Wind stress dust lifting averaged over all 10 years of INFDUST (in kg m^{-2} per 10 sols), and (b) the change in surface dust cover by the end of INFDUST, as a percentage of the initial uniform surface dust cover of 100 kg m^{-2} . Also shown is topography (solid contours) and (for plot b) the zero change line (dashed contour). Note that the contour interval is 15 times smaller for dust gains (positive) versus dust losses (negative) in plot (b).

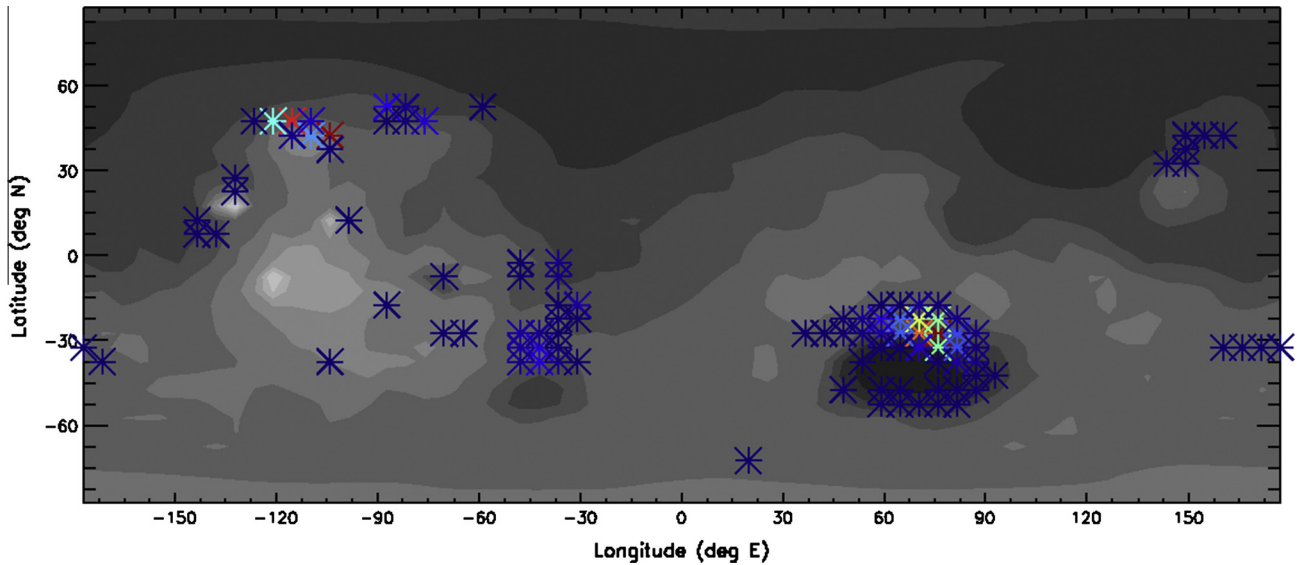


Fig. 5. Plots of the top 100 dust source grid points, colorized according to the fraction of dust mass contributed over all 10 years of INFDUST. Deep red shows the top ranked grid points, while the dark blue points indicate the lowest contributions within the top 100. See text for more details. (For interpretation of the references to color in this figure legend, the reader is referred to the web version of this article.)

greatest dust mass to the atmosphere in INFDUST. Using total mass (in kg) rather than dust flux (in kg m^{-2}) avoids biasing the ranking toward high latitude grid points, which represent a smaller surface area as grid spacing shrinks toward the poles. We are left with a slight bias toward low latitude grid points, but given the non-uniform grid some bias is inevitable when ranking by individual points. Collectively, the top 100 grid points contribute 99.6% of the total dust lifted. However, the top 6 ranked grid points (red) alone contribute over 50% of the dust lifted, whereas the deep blue grid points each contribute less than 0.02%. Most of the top 100 sit on the slopes of impact basins (particularly Hellas) and volcanoes (particularly Alba Patera, Olympus Mons and Elysium Mons), where strong slope winds occur. Other factors such as seasonal cap-edge flows (which affect Hellas) also play a role. Other top-100 grid points are located in regions subject to strong WBC (to the east of Tharsis), summer westerly ($\sim 30^\circ\text{S}$) or baroclinic eddy (seasonal cap edge, $\sim 45^\circ\text{N}$) flows.

The top three points (deep red) each contribute over 11% of the total dust mass lifted, with mean lifted dust fluxes of (i) $1.014 \text{ kg m}^{-2} \text{ yr}^{-1}$ at $104^\circ\text{W}, 42.5^\circ\text{N}$ (E slope of Alba Patera), (ii) $0.965 \text{ kg m}^{-2} \text{ yr}^{-1}$ at $115^\circ\text{W}, 47.5^\circ\text{N}$ (NNW slope of Alba Patera), and (iii) $0.854 \text{ kg m}^{-2} \text{ yr}^{-1}$ at $76^\circ\text{E}, 27.5^\circ\text{S}$ (NNE slope of Hellas). However, the mean deposited dust fluxes at these points are far smaller, only (i) 0.043, (ii) 0.039, and (iii) $0.048 \text{ kg m}^{-2} \text{ yr}^{-1}$. Assuming a dust density of 2500 kg m^{-3} , these lifting and deposition rates combine to give mean net loss rates of (i) 0.388, (ii) 0.370, and (iii) 0.322 mm yr^{-1} . This implies that a mm of dust would be lost from each of these grid points in about 3 years, with 10 m of dust lost in about 30,000 years. Hence for these grid points to represent long-term dust sources on real Mars over orbital time-scales they would need to be tens of meters deep. The Hellas location has a DCI above the upper limit given for 'dust-free' surfaces by Ruff and Christensen (2002), suggesting that such high lifting rates could not be maintained there for more than a few years.

The situation is less certain at the Alba Patera grid points, where results from imaging and spectroscopy are ambiguous. The high albedos and low thermal inertias could indicate it is mantled in several meters of mobile dust, but are also consistent with it being duststone or covered in dust aggregates too large to suspend, with relatively little mobile dust on the surface (Bridges et al., 2010). While the former would enable such high dust lifting rates to continue for tens of thousands of years, the latter would not. We discuss this further in Section 4.6.

Fig. 6 shows the surface dust mass every 10 sols (left column), and the total mass of dust lifted by wind stress and deposited over the previous 10 sols (middle and right columns, respectively), at the 1st, 3rd, 19th and 43rd ranked grid points over the first 9 years of INFDUST. At the 1st ranked grid point (on the slopes of Hellas),

three large depletion events occur in each year with a global storm, and correspond to large, sustained wind stress lifting events during the storm season in those years, with negligible changes in surface dust at all other times. By contrast, the 3rd ranked grid point (on the slopes of Alba Patera) has significant depletion due to wind stress lifting events in every storm season, though they are far larger in global storm years. Although deposition also peaks during these lifting events, it is at least an order of magnitude smaller, since most of the dust lifted is transported elsewhere rather than being re-deposited locally. Gradual deposition also occurs outside of the big lifting events and is mostly associated with increased regional dustiness due to widespread dust devil lifting, peaking during local summer for the four grid points shown. However, local dust devil lifting (not shown) slightly exceeds deposition at the

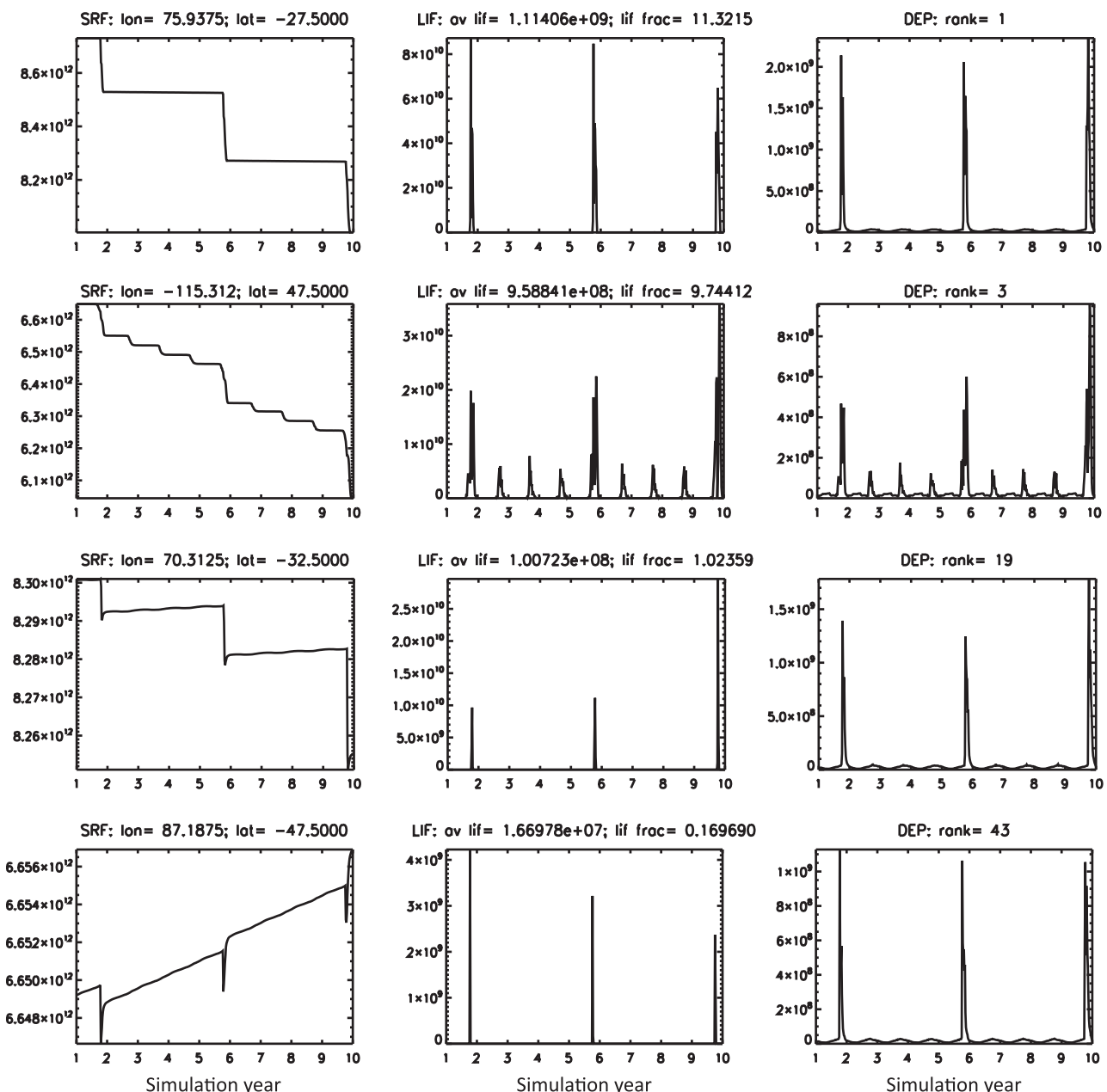


Fig. 6. Area-weighted surface dust cover in kg (left column), and total wind stress dust lifting (middle column) and dust deposition (right column) over the previous 10 sols in kg/10 sols, for INFDUST years 1–9, at the surface grid points ranked 1st (top row), 3rd (second row), 19th (third row) and 43rd (bottom row) in terms of their total dust mass contribution during INFDUST. Also given are the locations, the total mass and fraction of the top-100 amount lifted by wind stress, and the grid point ranking. (NB: the initial dust cover was globally uniform in terms of mass per unit area but not total dust, hence differs with latitude.)

first two points shown here, resulting in a very slow (imperceptible on these plots) decrease in dust, even between the large depletion events.

Unlike the 1st and 3rd ranked points, the 19th point has periods of dust accumulation too. Rapid accumulation occurs immediately after big depletion events, due to lifting shutting down locally while the storm still rages with its associated larger deposition rates. However, this accumulation is shortlived and recovers only a small percentage of the dust lost to the storm. Gradual accumulation occurs annually in late southern summer, due to increased regional dustiness associated with dust devil lifting, with local dust devil lifting slightly exceeded by deposition at this grid point. Despite these modes of accumulation, however, the big depletion events still dominate the overall trend in surface dust, resulting in net loss over the years shown. Not until the 43rd ranked point is there an upward trend in surface dust cover, with peak deposition rates only a few times smaller than peak lifting rates here. It shows the same two accumulation modes as the 19th ranked grid point, but with comparable amounts of dust received as lost during global storms, and with greater gradual replenishment during local summer. However, it contributes less than 0.2% of the total dust mass lifted, thus has little impact on the dust cycle as a whole.

In summary, in infinite surface dust simulation INFIDUST, nearly a third of the total dust mass is contributed by only three grid points, each representing a $5^\circ \times 5.625^\circ$ region of surface. Mean net loss rates of dust from these primary source regions is equivalent to losing 10 m of dust cover in about 30,000 years, which is orders of magnitude larger than the inferred dust cover for at least one of the points. There is also persistent transfer of dust away from the grid points contributing ~98% of the raised dust. In combination with the failure (Section 3.3.1) of any infinite surface dust simulation to capture the full observed range of dust source regions, storm onset times and durations, and interannual variability, this strongly motivates the finite surface dust studies described below.

4. Dust cycle simulations with finite surface dust and a constant stress threshold

As described in Section 1.3 we seek a self-consistent long term steady state consisting of (a) an invariant long-term mean finite surface dust distribution, and (b) a set of dust lifting parameters that support continuing major storms. In Section 4.1 we describe our approach to seeking such a steady state, while Section 4.2 provides an introduction to our most realistic finite dust simulation, FINDUST, and an overview of results. In Section 4.3 we focus on the realism of dust storms during a ‘quasi steady state’ period near the end of FINDUST, and in Section 4.4 we use this period as a proxy for potential real behavior on Mars to investigate the impact of surface dust rearrangement on storm type and interannual variability. In Sections 4.5 and 4.6 we examine the mean surface dust distribution by the end of FINDUST and its implications, then in Section 4.7 we ask if the surface dust distribution at a given time could be used to make dust storm predictions.

4.1. Our approach to seeking a steady state solution

The steady state lifting parameters will only produce realistic dust storms and cycles for the steady state surface dust distribution. However, the steady state surface dust distribution is created by the rearrangement of surface dust, which itself depends on the lifting parameters: a ‘Catch 22’ situation. Even if we could guess the steady state lifting parameters, we could not use them in a radiatively active dust simulation begun with surface dust available everywhere, as they would produce far too much dust lifting.

And it is not possible to guess the steady state surface dust distribution anyway. It may seem reasonable to base it on observations, but this idea is flawed for two reasons: estimating the thickness of mobile dust deposits everywhere, based on e.g. remotely sensed albedo or DCI maps, is currently impossible, as such variables cannot be easily or uniquely mapped to dust cover (see Section 4.6 iv); also, what we really need is the steady state in the GCM, which likely differs from that on Mars, as MarsWRF is not a perfect representation of the real system.

The approach we use is therefore designed to gradually iterate toward the steady state surface dust distribution and lifting parameters at the same time, maintaining somewhat realistic atmospheric dust opacities and hence circulations as we move toward steady state. We begin with globally uniform surface dust cover and tune the lifting parameters to produce the most realistic dust cycle possible. We then use the GCM to evolve the surface dust distribution, at intervals re-tuning the lifting rate parameters such that the simulation continues to produce the most realistic dust cycle as more source regions are exhausted. This exhaustion may be either ‘temporary’ or ‘permanent.’ In the former case, grid points are exhausted seasonally or during a storm, but are subsequently replenished enough to act as major sources again. In the latter case, once grid points are exhausted they never regain enough dust to contribute significantly. We continue this process until the surface dust distribution no longer changes in a long-term sense, no further grid points are permanently exhausted, and realistic dust cycles continue to be produced with no further changes in lifting parameters required. We leave a discussion of the advantages and disadvantages of this approach to Section 4.6 (ii).

As in our precursor study (Newman, 2001) we choose to hold the wind stress threshold constant and increase the dust devil and wind stress lifting rate parameters as necessary to maintain realistic (a) background global T15 cycles and (b) peak global T15 values during storms. α_D is adjusted infrequently compared to α_N as source regions exhaust. This is because exhaustion of a given grid point has little impact on total dust devil lifting, which is widespread and varies gradually with location, thus depletes the surface relatively slowly and evenly. A large number of grid points must be exhausted before the background global T15 is affected. Conversely, dust exhaustion at a single grid point can have a huge impact on total wind stress lifting, if it is one of the relatively few points where the threshold stress is often and/or greatly exceeded. Note that the increases in α_N and α_D do not map to real physical processes, but are merely a numerical tool to seek the steady state solution, which by definition is the point at which no further long-term changes in surface dust occur and hence no further lifting rate increases are required.

Fig. 7 shows the approach schematically. Starting with globally uniform surface dust cover, we (i) run MarsWRF until the primary source regions are exhausted and dust storms cease – this is referred to as a ‘Stage’ of the simulation – then (ii) increase α_N until storms of the observed magnitude occur again, with peak lifting now coming from new primary source regions. Occasionally step (ii) is combined with or replaced by an increase in α_D so as to maintain realistic background global T15. Steps (i) and (ii) are repeated until the final primary source regions are those that gain (over several years) as much dust via deposition as they lose via lifting. At this hypothetical end point, the surface dust cover and hence dust cycle is in long term steady state, and no further increases in lifting rate parameters are required for major storms to continue to occur.

We show results from our longest finite dust simulation, FINDUST, lasting 374 years. The steady state we seek requires a pattern of lifting that can be offset by the pattern of deposition over several years. High thresholds produce lifting concentrated at relatively few, typically widely spaced source grid points,

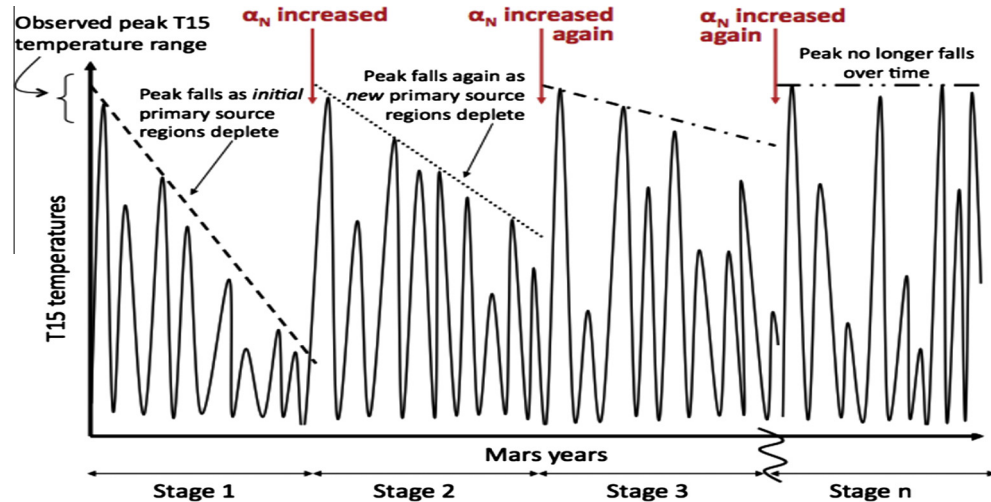


Fig. 7. Each Stage of a finite dust simulation restarts from the end of the previous Stage (i.e., using the final surface dust distribution) with the same wind stress lifting threshold but a higher lifting rate parameter, usually the wind stress rate, α_N (and/or the dust devil rate, α_D , on occasion). This continues until the simulation is 'stable' – i.e., continues to produce major storms with no further lifting rate increase required.

Table 2

Lifting rates, duration, and results (in terms of storms produced) for all 17 Stages of simulation FINDUST. Major, global and large regional storms are defined in Section 1.1.2. In all cases, major storms had been absent for at least 5 years before the lifting rate parameter was increased and a new stage began.

Stage	α_N	$\alpha_D (\times 10^{-10} \text{ kg J}^{-1})$	Year range	# of yrs	Types of dust seasons produced among all years of a given stage			
					Years without major storms	Years with 1 large regional storm	Years with 1 global storm	Years with >1 major storm
A	3.5	7.	1–10	10		X	X	
B	5.5	"	11–20	10		X	X	
C	8.5	"	21–30	10		X	X	
D	10.	"	31–40	10		X	X	
E	16.	"	41–70	30	X	X	X	
F	20.	"	71–88	18	X	X	X	
G	25.	"	89–108	20	X	X	X	
H	"	20.	109–118	10	X	X		X
I	37.5	"	119–137	19	X	X	X	
J	50.	"	138–167	30	X	X	X	
K	57.5	"	168–187	20	X	X	X	
L	67.5	"	188–206	19	X	X	X	X
M	80.	"	207–246	40	X	X	X	X
N	100.	"	247–276	30	X	X	X	X
O	120.	"	277–356	80	X	X	X	
P	140.	40.	357–364	8	X			
Q	180.	"	365–374	10	X	X	X	

making it hard to see how the more widespread deposition of dust following a global storm could manage to replenish them. FINDUST therefore uses a relatively low threshold of $\tau_t = 0.02 \text{ Pa}$, in order to activate a larger fraction of the surface. The threshold wind stress on Mars has been estimated in the laboratory, e.g. wind tunnel measurements of the fluid threshold required to initiate saltation (Greeley et al., 1980), and theoretically, e.g. numerical modeling showing that the impact threshold when saltation has begun may be orders of magnitude lower than the fluid threshold (Kok, 2010). However, we are most interested here in the threshold appropriate for use with $\sim 5^\circ$ resolution winds. A recent study used MarsWRF winds at this resolution to predict the seasonal variation of sand fluxes in the Nili Patera dune field for different assumed thresholds, and found the best match to the observed seasonality of dune movement at a threshold of $\sim 0.008 \text{ Pa}$ (Ayoub et al., 2014). The threshold used in FINDUST is more than twice this value, but far lower than the thresholds of $0.046\text{--}0.05 \text{ Pa}$ needed to produce large interannual variability in our infinite surface dust simulations (Section 3). We note that K05 used a similar value ($\tau_t = 0.022 \text{ Pa}$) in their finite dust simulations. In Section 5.1 we use $\tau_t = 0.026 \text{ Pa}$ as the initial threshold value in our variable

threshold simulations, while M13 and WK09 used respectively 0.025 and (in a higher resolution simulation) 0.028 Pa in theirs.

4.2. Overview of finite surface dust simulation FINDUST

Simulation FINDUST was initialized with a globally uniform surface dust cover of 2 kg m^{-2} , equivalent to 0.8 mm depth. This value was chosen such that exhaustion of grid points began after only a few Mars years. FINDUST consists of 17 Stages, summarized in Table 2 and Fig. 8, each of which ran until no global storm had occurred for at least 5 years. In addition to increases in α_N , α_D was also increased twice, whenever enough grid points were exhausted to impact even the background global T15. Not shown are the calibration runs needed to find the new value of α_N (and/or α_D) at the start of each Stage.

To demonstrate the process, Fig. 9 shows global T15 curves for a 40-year portion of FINDUST, from the start of Stage G to midway through Stage I. For clarity, results are shown in 10-year increments. Major storms had ceased by the end of Stage F, thus at the start of Stage G α_N was increased by 25% to increase wind stress lifting such that major storms resumed. During the first half of

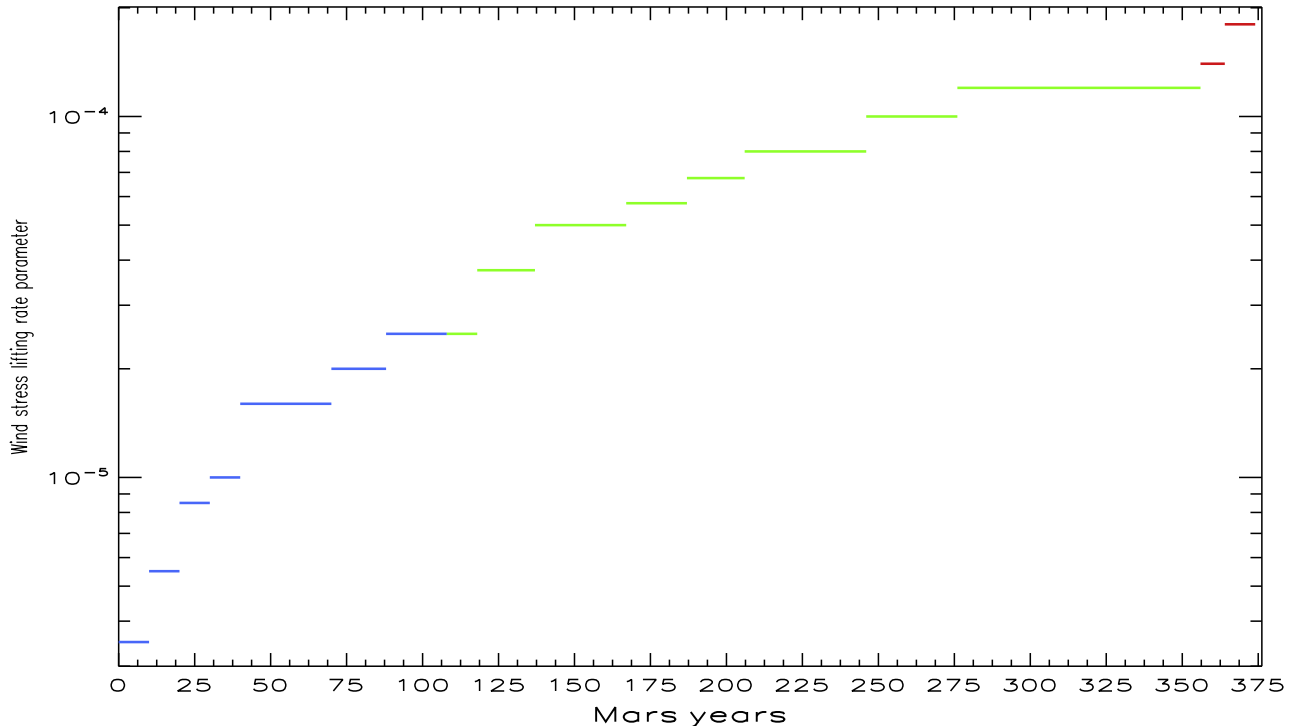


Fig. 8. Graphical representation of Table 2, showing the 17 Stages of FINDUST. Each horizontal line of one color represents a different Stage, with its duration indicated on the horizontal axis; the vertical axis indicates values of α_N ; while color changes indicate the (infrequent) times when α_D was increased (blue indicates $\alpha_D = 7 \times 10^{-10}$, green $\alpha_D = 2 \times 10^{-9}$, and red $\alpha_D = 4 \times 10^{-9} \text{ kg J}^{-1}$). (For interpretation of the references to color in this figure legend, the reader is referred to the web version of this article.)

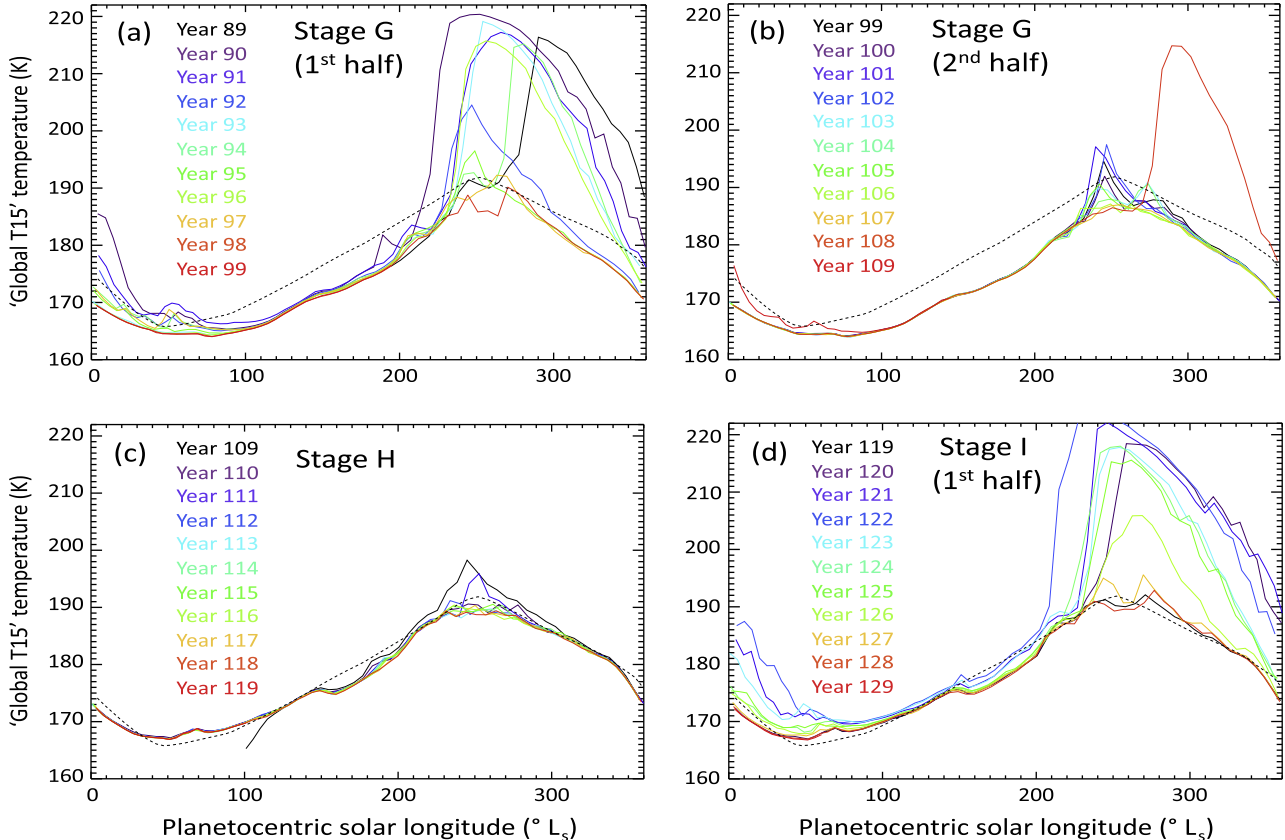


Fig. 9. Global T15 curves as in Fig. 2, but for Stages of simulation FINDUST, as labeled. See Table 2 for details of how the lifting parameters change with Stage. Years shown are from the start of FINDUST.

Stage G (Fig. 9a), major storms occurred with a range of sizes. However, an overall downward trend in storm size over time had become clear by the second half of Stage G (Fig. 9b), with a gap of 11 years between major storms, thus another increase in α_N was due. In addition, background global T15 had fallen several K below observed values, thus an increase in α_D was required too. Stage H (Fig. 9c) involved a nearly threefold increase in α_D only, bringing background global T15 back into agreement with observations. α_N was then increased by 50% at the start of Stage I (Fig. 9d), causing global storms to resume. Note that the decay rate of most of these global storms is slower than observed on Mars (Fig. 1), and also slower than storms simulated in the later Stages of FINDUST (e.g. Stage O, shown in Fig. 10).

Although the rate of exhaustion of source regions slows as FINDUST continues, it ultimately reaches a point at which the surface dust distribution no longer supports realistic storms. Beyond the final stage (Stage Q), further increases in α_N produced either no storms (for small increases in α_N) or runaway lifting and unrealistically huge peaks in global T15 (for larger increases in α_N). Effectively, the only steady state solution possible by the end of FINDUST was one unable to support continuing major storms. This may be a result of deficiencies in MarsWRF, though it is also possible that the GCM is capable of achieving a self-consistent, long term steady state with continuing dust storms, but that our iterative method failed to locate it. Both options are discussed further in Section 4.6.

4.3. The dust cycle and dust storms in simulation FINDUST Stage O

Despite not reaching a steady state with continuing major storms, Stage O runs for almost 80 years before storms cease. This indicates a very gradual loss of primary source regions, and

suggests that this Stage may exhibit quasi-steady state behavior, potentially providing a proxy for steady state behavior on Mars itself. In this section we demonstrate the quasi-steady state nature of Stage O, identify families of storms and briefly examine their onset, growth and decay phases, and compare them with families of storms observed. For simplicity, we refer to years 1–80 of Stage O rather than years 277–356 of FINDUST.

4.3.1. Overview of Stage O

Fig. 10 shows T15 curves from Stage O years 1–31 (Fig. 10a–c) and 61–71 (Fig. 10d). Over the first 30 years there are 10 years (1, 2, 10 to 14, 23, 24 and 29) with global dust storms, and another 6 years (3, 4, 15, 16, 25 and 30) with large regional storms. The last major storm of Stage O occurs in year 70. Unlike the major dust storms produced in our infinite dust simulations (Section 3), these show a far wider range of onset times. The earliest begins in year 11 at $L_s \sim 200^\circ$, which is still later than the earliest observed storm onset (at $L_s \sim 184^\circ$ in MY 25) but represents a major improvement on INFIDUST, in which the earliest storms begin at $L_s \sim 265^\circ$. In INFIDUST, peak lifting and storm onset correlates with peak wind stresses, which occur later in the storm season. In FINDUST, however, the timing of peak lifting and thus storm onset is determined both by wind stresses and surface dust availability. By Stage O, most high wind stress regions are exhausted, and the new primary source regions are ‘active’ (i.e. have wind stresses that exceed threshold) more evenly across the storm season (see Sections 4.4.3 and 4.4.4).

In terms of storm evolution, while global T15 values do not return to background levels until the end of the storm season in some years, decay occurs much sooner in others. Compare e.g. the late versus early decay in respectively years 23 and 24 (Fig. 10c). Overall, storm decay remains slower than observed on

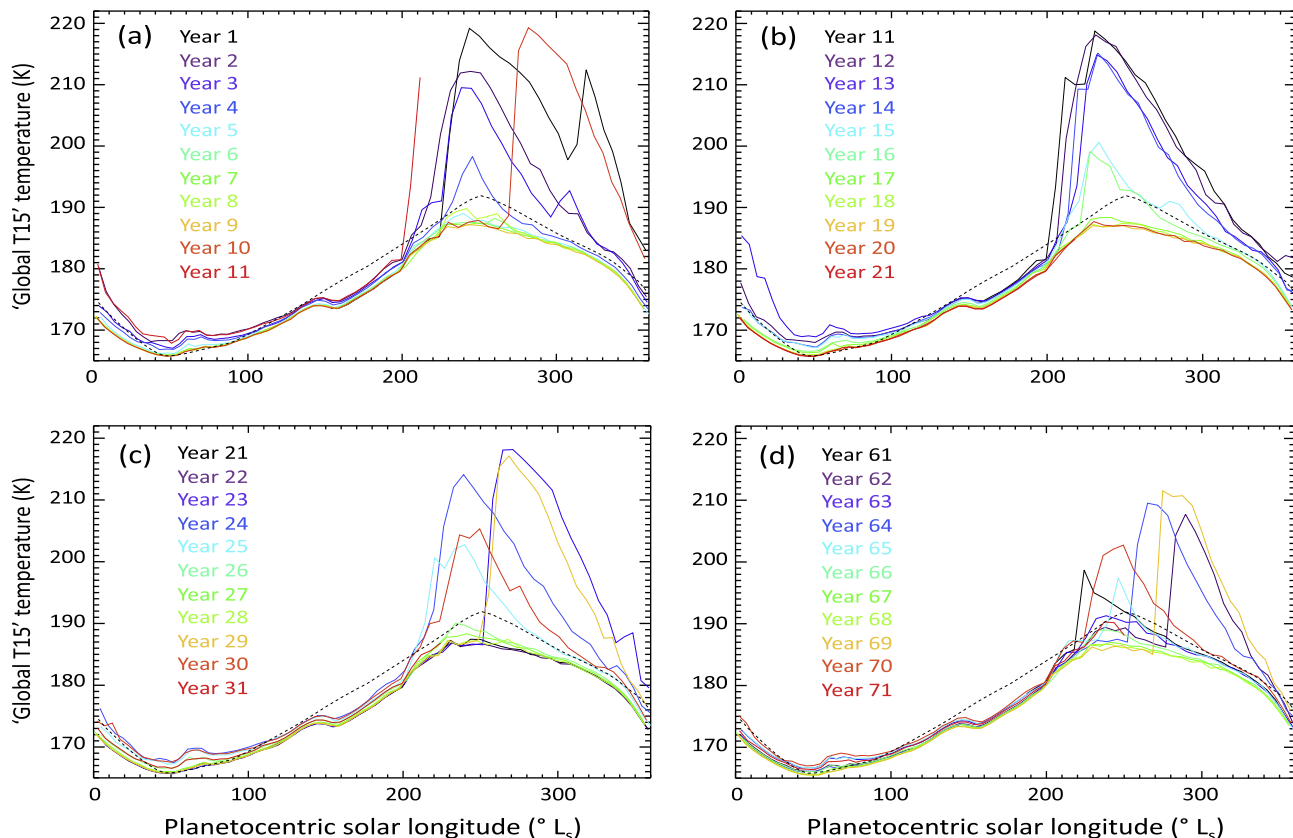


Fig. 10. Global T15 curves as in Fig. 2, but for 10-year increments of FINDUST Stage O: (a) years 1–11; (b) years 11–21; (c) years 21–31; and (d) years 61–71. Note that α_N and α_D are held constant throughout, and that the years shown are now years of Stage O rather than years from the start of FINDUST.

Mars, but is much faster than in our infinite surface dust simulations, and early storm decay has now become possible.

4.3.2. To what extent is Stage O in a quasi-steady state?

There is no obvious decrease in peak global T15 or range of storm types produced over the first 60 years of Stage O (the first 30 years of which are shown in Fig. 10a–c), despite several grid points being permanently exhausted during this time. E.g., 4 of the top 100 ranked points (in terms of dust mass lifted) in years 21–30, together contributing ~4.5% of the total dust lifted over that period, are permanently exhausted by the end of it. The relatively low fractional contribution of the source regions lost may explain why global storms continue to occur, and why the next 30 years (years 31–60) are not very different in terms of the storms produced. By contrast, Fig. 10d shows distinctly different dust cycles in years 61–70. Storms are more confined temporally, with only one peaking above 210 K. By the end of year 70, 18 of the top 100 ranked grid points in years 21–30 – which contributed ~19% of the total dust in that period – have been permanently exhausted. Years 71–80 produced no major storms at all, suggesting exhaustion of too many source regions to produce further major storms without another increase in α_N . In summary, the number of grid points that exhaust permanently (or temporarily for the first time) – and the impact on results – is very small over the first 60 years of Stage O. This suggests we may be able to treat this period as being in a quasi-steady state, and use it to investigate processes and mechanisms connected to finite dust availability. Rather than analyze the entire period, we focus on dust cycles and storms in years 21–30 of Stage O.

4.3.3. Overview of major dust storms in years 21–30 of Stage O

The five major dust storms produced in Stage O years 21–30 may be generally broken into two types: ‘early’ (onset in the range $L_s \sim 210\text{--}220^\circ$) and ‘late’ (onset at $L_s \sim 252^\circ$). There are late global storms in years 23 and 29, an early global storm in year 24, and early large regional storms in years 25 and 30. Figs. 11 and 12 show respectively the zonal mean column visible dust opacity above the 610 Pa pressure level, and the zonal mean wind stress dust lifting, for the period containing all of these storms. Some northern hemisphere lifting is associated with the major storms, but peak zonal mean lifting and opacities occur in the southern hemisphere. The late storms reach the south pole, since by then the seasonal cap has receded enough to permit lifting from high southern latitudes. In every year shown, increased zonal mean lifting follows the retreating south polar cap edge from $L_s \sim 220^\circ$ to 255° , and the growing north polar cap edge from $L_s \sim 190^\circ$ to 220° , though the latter is far weaker. Section 4.3.5 examines the onset and growth (expansion) of these major storms in more detail, and compares them to the smaller storms described in Section 4.3.4.

4.3.4. Regional dust storms in years 21–30 of Stage O

Hundreds of smaller regional storms also occur in years 21–30 of Stage O. These can be grouped into seven general types, which are described below and listed in Table 3 in order of their earliest onset times, beginning at the start of the storm season at $L_s = 180^\circ$.

Type 1 ‘Northern frontal’ regional storms: In autumn, strong temperature gradients in the vicinity of the growing northern cap edge lead to significant baroclinic wave activity in the GCM and associated strong surface winds every year. From $L_s \sim 187^\circ$ to 228° these

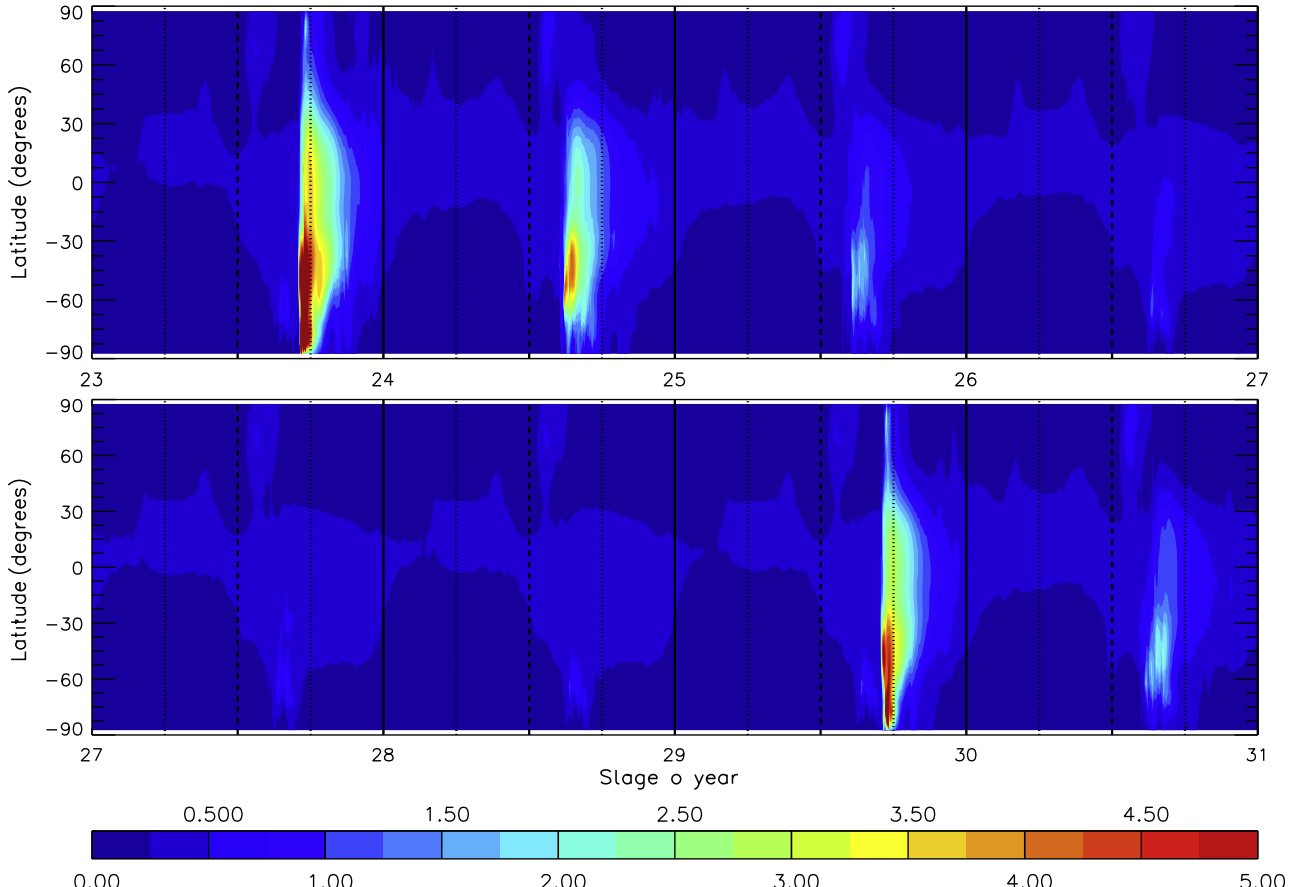


Fig. 11. Zonal mean visible dust opacity at 610 Pa for years 23–30 of FINDUST Stage O. Solid vertical lines show $L_s = 0^\circ$, dashed lines $L_s = 180^\circ$, dotted lines $L_s = 90^\circ$ and 270° . Late global storms occur in years 23 and 29, an early global storm occurs in year 24, and early large regional storms occur in years 25 and 30.

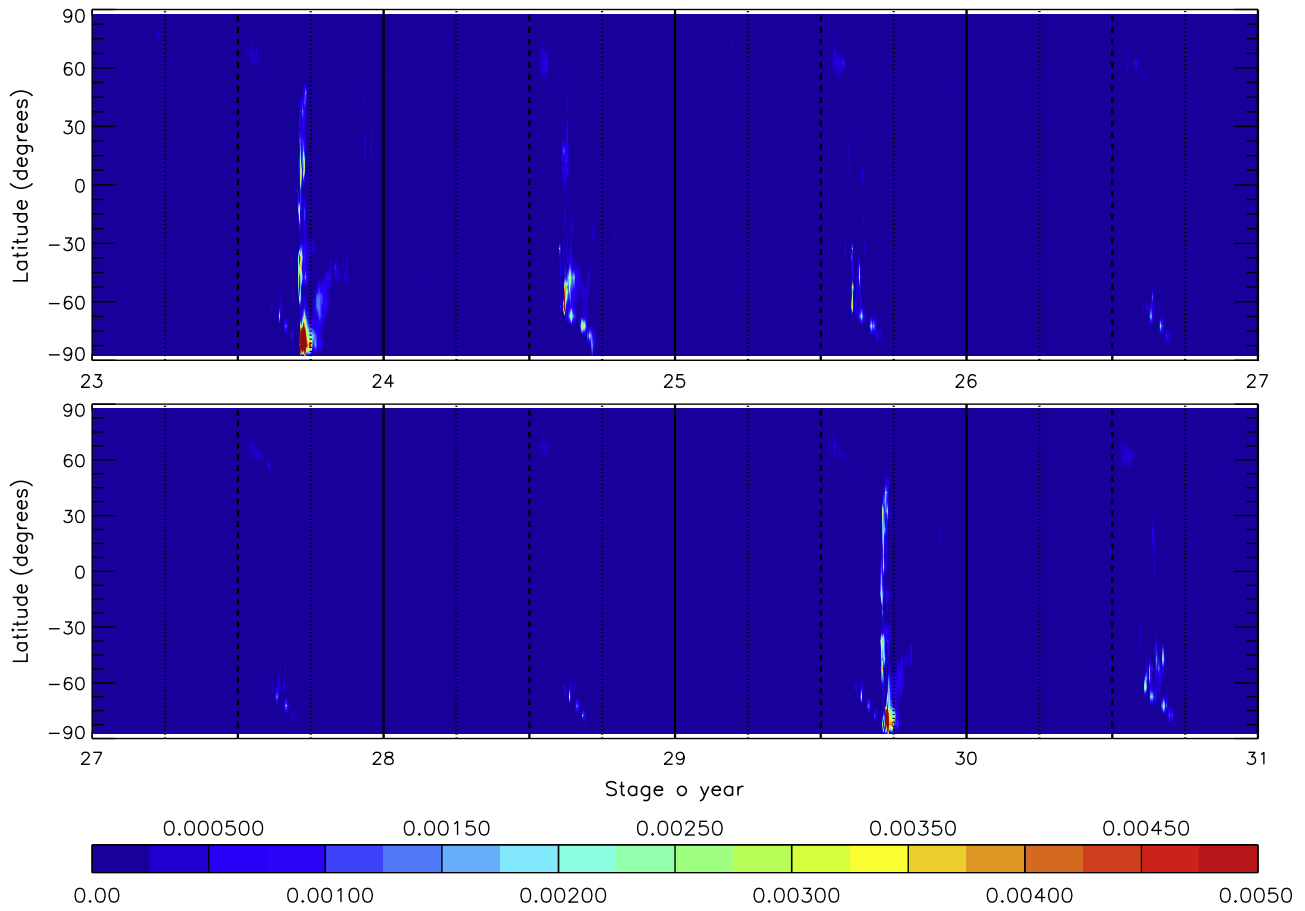


Fig. 12. As Fig. 11, but showing zonal mean wind stress dust lifting in kg m^{-2} per 10 sols.

Table 3

Summary of simulated regional storm types in FINDUST Stage O years 21–30.

Regional storm	Name	L_s range ($^\circ$)	Onset location(s)
Type 1	Northern frontal	187–228	Acidalia–Chryse, Utopia–Isidis and Arcadia–west of Tharsis
Type 2	Noachis/Hellas	209–220	Noachis/NW of Hellas
Type 3	Southern cap edge/Hellas	226–250	Southern cap edge/slopes of Hellas
Type 4	Late winter northern	308–358	Chryse, Isidis and west of Tharsis
Type 5	Early northern spring	0–40	Tharsis, Elysium and Argyre
Type 6	Late winter southern basin	158–179	Southern cap edge/slopes of Argyre and Hellas
Type 7	Pre-spring Hellas	171–185	West and NW of Hellas

strong winds trigger increased lifting along the cap edge, and numerous dust clouds form over northern high latitudes. Most show frontal behavior as the raised dust is advected by waves, and over a dozen sequences can occur during this period, with visible opacities exceeding 2 about half the time. As with the observed storms described in Section 1.1.2, some of these clouds evolve into flushing or cross-equatorial storms moving through one of three meridional corridors between high topography, in Acidalia–Chryse, Utopia–Isidis, or Arcadia–west of Tharsis. Fig. 13 shows a year 21 cross-equatorial storm, beginning in Acidalia. The storm grows larger in Chryse and expands just into the southern hemisphere, then dissipates due to lack of low-latitude lifting. Fig. 14 shows a similar sequence during onset of the year 24 global storm, but now lifting continues into the southern hemisphere and the storm does not fade. Years 21–30 produce a similar number of Utopia–Isidis and Acidalia–Chryse storms, whereas observations indicate two or three times more in the Acidalia–Chryse ‘corridor.’ However, the simulated Acidalia–Chryse storms are generally

more intense and a larger fraction of them expand, which may explain the disparity if only larger storms were observed. In agreement with observations, far fewer storms occur in the Arcadia–west of Tharsis corridor than in the other two.

Type 2 ‘Noachis/Hellas’ regional storms: In some years, strong simulated lifting in mid-southern spring ($L_s \sim 209\text{--}217^\circ$) produces dust clouds in the general Noachis region to the NW of Hellas, triggering more lifting further south in Noachis and around Hellas. The dust cloud often shifts into Hellas, and sometimes grows to cover the entire Noachis/Hellas region. Fig. 14 shows two such ‘Noachis/Hellas’ storms, the first a small regional one at $L_s \sim 209^\circ$, and the second forming part of the onset of the year 24 global storm. Unlike the type 1 and 3 regional storms, there are several years in which no Noachis/Hellas storms occur despite the atmosphere being relatively dust-free (i.e., in which their occurrence is not prevented by a major storm already being active). Their initiation mechanism thus exhibits more interannual variability than type 1 and 3 storms.

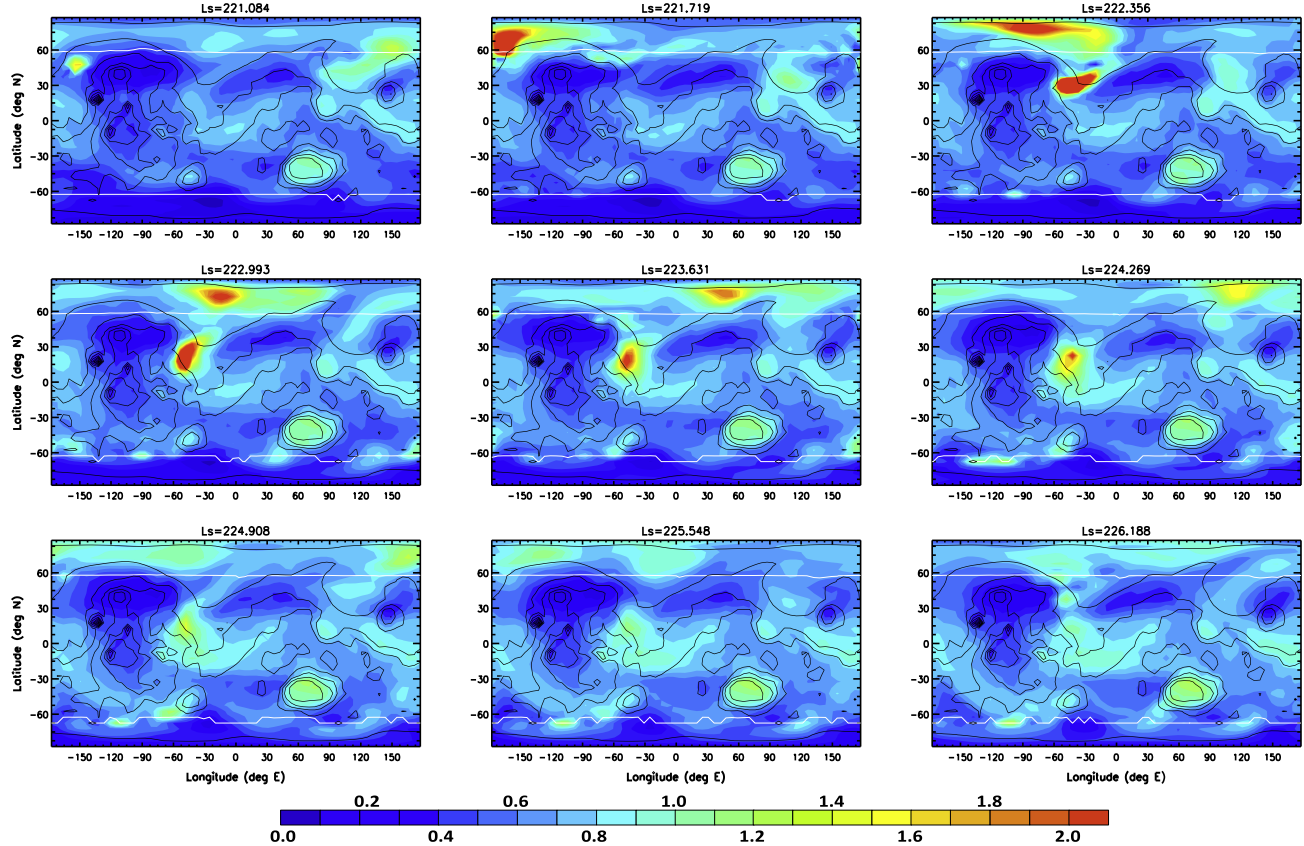


Fig. 13. Maps of visible dust opacity every sol from $L_s \sim 221^\circ$ to 226° in year 21 of FINDUST Stage O, showing the development of a type 1 Acidalia–Chryse regional storm. Note that the colored contours saturate above 2. Also shown is topography (black contours) and residual CO_2 cap edge (white contours). (For interpretation of the references to color in this figure legend, the reader is referred to the web version of this article.)

Type 3 ‘Southern cap edge/Hellas’ regional storms: Enhanced lifting occurs every year from $L_s \sim 221^\circ$ to 251° along the edge of the retreating south polar cap, due to strong winds associated with large temperature gradients there. This results in cap edge regional storm onset at $L_s \sim 226$ – 230° , except in years when a larger storm is already active. The storm grows as dust moves into the Hellas basin, with more lifting triggered mostly on its SE/E slopes. An example is shown in Fig. 15. The main storm dissipates within 10 – 20° of L_s , and leaves raised dust levels in Hellas for another 10 – 20° of L_s . Occasionally, similar but usually weaker behavior occurs in association with the Argyre basin in the same period.

Type 4 ‘Late winter northern’ regional storms: Weaker, more localized storms occur in some years in Chryse, Isidis or west of Tharsis in the period $L_s \sim 308$ – 358° . Unlike the type 1 storms, the (now retreating) cap edge is simulated to cover latitudes down to at least $\sim 50^\circ\text{N}$ throughout this later period, thus all dust lifting associated with these storms occurs at lower latitudes in the meridional corridors, rather than in Acidalia, Utopia or Arcadia (which are covered with CO_2 ice). Interestingly, these storms are larger and more active in years when a major storm has occurred. This suggests either that their primary source regions require replenishment of surface dust during fallout from an earlier major storm, and/or that winds here are stronger during the period of dust storm decay. Similar feedbacks that may affect major storm occurrence are discussed in Section 4.4.

Type 5 ‘Early northern spring’ regional storms: Small regional storms occur in some years in the Tharsis, Elysium or Argyre regions between $L_s \sim 0^\circ$ and 40° . As with the type 4 storms, these show dependence on recent major storm activity, in this case being larger and more active in years following a late major storm. This

suggests replenishment of surface dust and/or dynamical changes associated with big late storms is critical to them.

Type 6 ‘Late winter southern basin’ regional storms: In some years, short storms occur during $L_s \sim 158$ – 179° , involving lifting around the southern cap edge into Argyre or Hellas.

Type 7 ‘Pre-spring Hellas’ regional storms: Small regional storms lasting at most a few degrees of L_s occur every year in late southern winter (onset between $L_s \sim 171^\circ$ and 176°), and consist of lifting to the west of Hellas, with the dust raised being advected into the Hellas region. Fig. 16 shows a sequence of these storms from year 24. The first two are typical examples, while the third is the largest produced in years 21–30 and includes stronger lifting to the NW of Hellas, though still does not activate further lifting on other Hellas slopes. As with the type 3 storms, occasionally similar (though typically weaker) behavior is also produced in association with the Argyre basin during the same period.

4.3.5. The link between regional and major storms in years 21–30 of Stage O

In this section we consider whether our simulated major storms are regional storms that grew larger or combined, or whether they have distinctly different onset behavior.

4.3.5.1. Early major storms. Onset and expansion of the year 24, $L_s \sim 217^\circ$ global storm is shown in the lower two thirds of Fig. 14. It consists of nearly simultaneous type 2 (Noachis/Hellas) and type 1 (Acidalia/Chryse) regional storms followed by further lifting in both hemispheres (primarily in Chryse, Elysium, and 45 – 60°S) as the storm expands. Fig. 17 shows the pattern of dust lifting corresponding to the onset and growth phases. Onset of

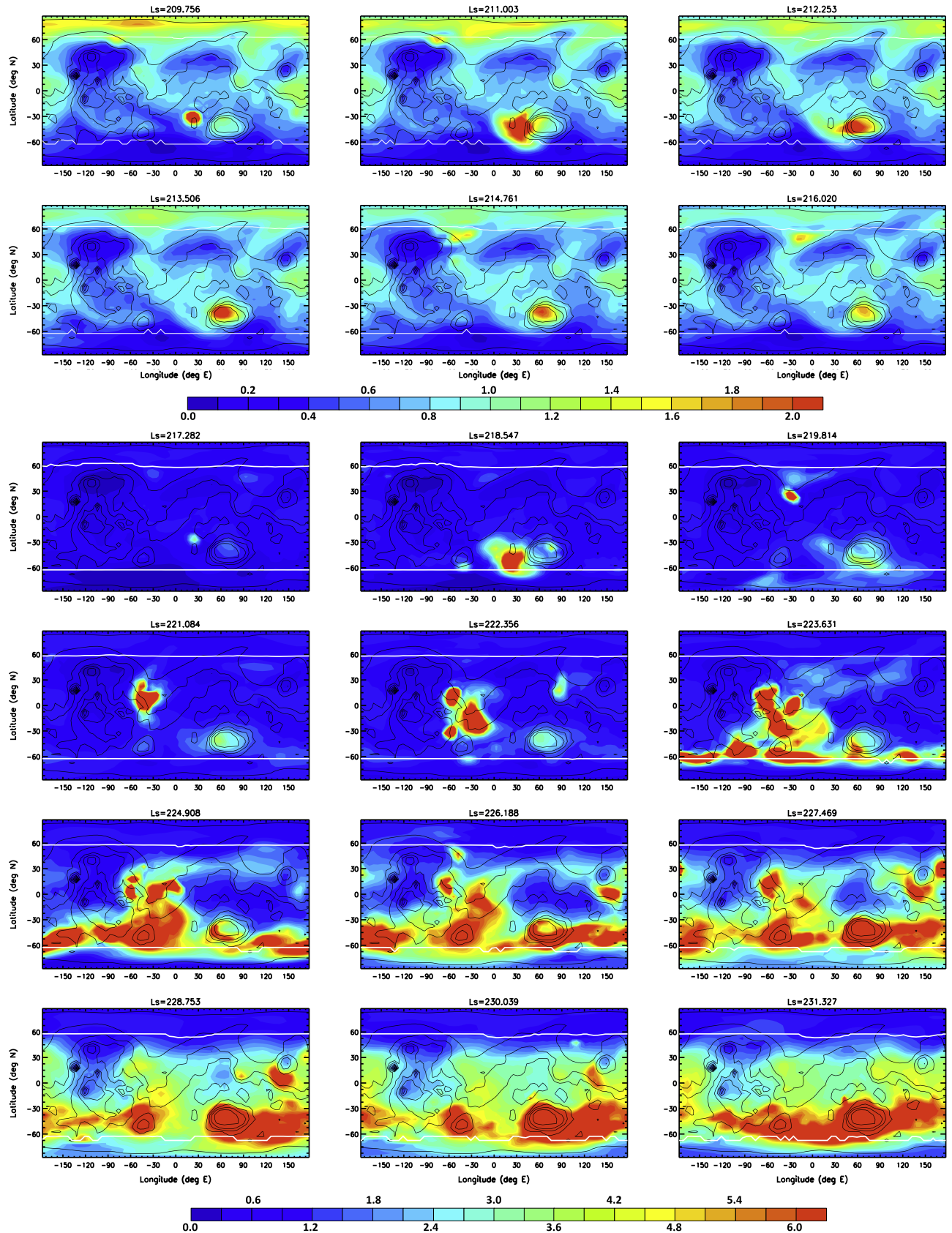


Fig. 14. As Fig. 13, but showing dust opacity every two sols for $L_s \sim 210\text{--}231^\circ$ in year 24. The second of two type 2 Noachis/Hellas regional storms combines with a type 1 Acidalia–Chryse regional storm and leads to onset of an early global storm. Note that the second type 2 storm is more intense than the first; contour intervals are tripled after the first type 2 storm, to better show onset and growth of the global storm.

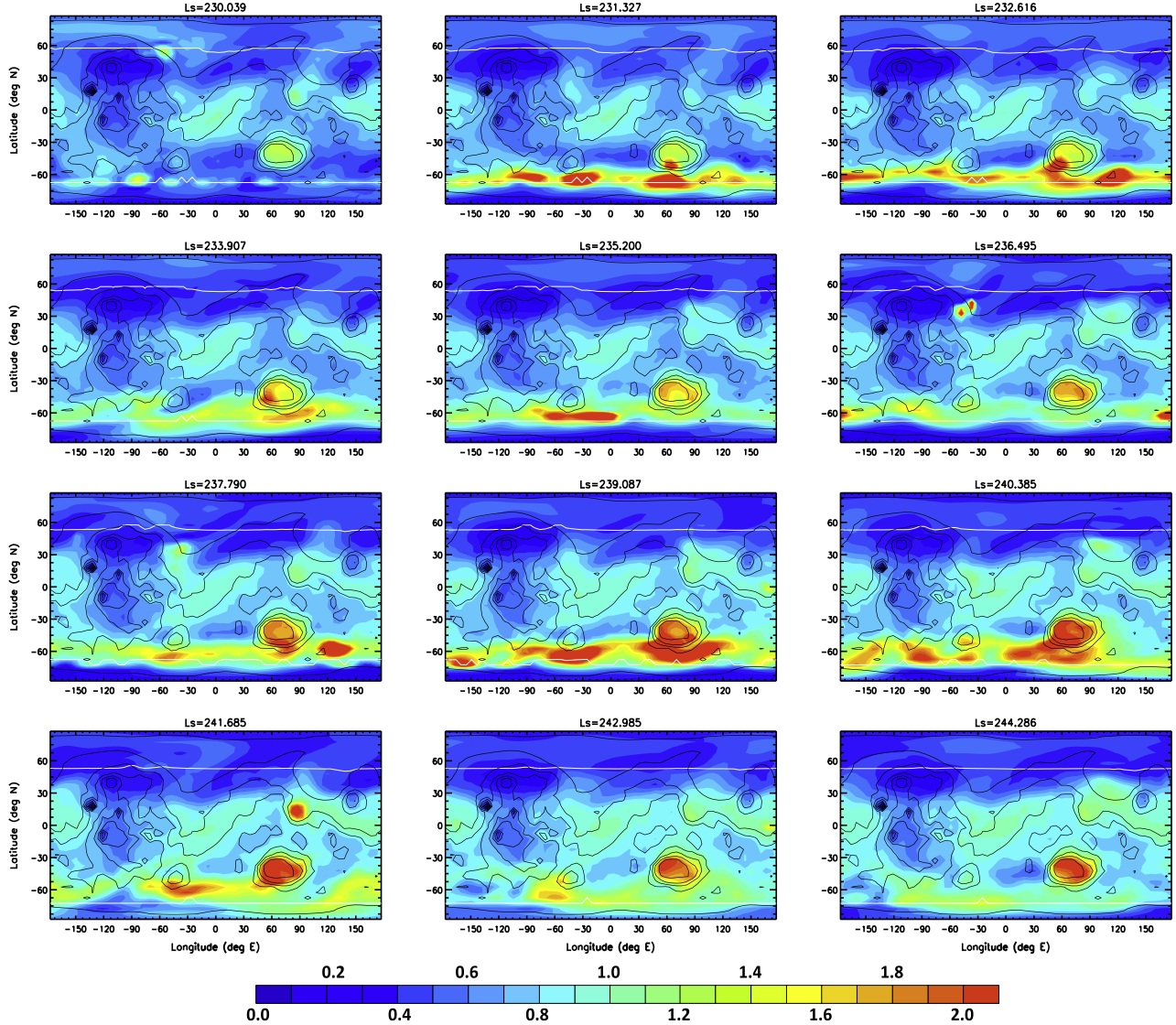


Fig. 15. As in Fig. 13, but showing dust opacity every two sols from $L_s \sim 230^\circ$ to 244° in year 21, showing the development of a type 3 southern cap edge/Hellas regional storm.

the year 25 large regional storm is nearly identical, though occurs slightly earlier at $L_s \sim 210^\circ$ and produces little subsequent lifting in the north and weaker lifting overall. By contrast, the year 30 large regional storm begins slightly later at $L_s \sim 220^\circ$, and consists of a type 2 (Noachis/Hellas) followed by a type 3 (cap edge/Hellas) regional storm, with further lifting largely restricted to the southern hemisphere, mostly along the polar cap edge. Latitudes poleward of $\sim 50^\circ\text{N}$ remain relatively dust-free during all three storms, but whereas the year 24 global storm activates significant northern hemisphere lifting, the year 25 and 30 large regional storms do not and are largely confined to the south.

In summary, all three early major storms begin as large regional storms of type 1, 2 and/or 3 at $L_s \sim 210\text{--}220^\circ$ – with the same onset timings and locations as in years without major storms. These then combine and expand to form either (a) a large regional storm or (b) a global storm if sufficient additional northern and southern lifting sites are activated.

4.3.5.2. Late major storms. Onset and expansion of the year 23 and 29 global storms is nearly identical. Figs. 18 and 19 show year 23 visible dust opacities and wind stress lifting, respectively. The

storm begins as a dust cloud in the Isidis/Tyrrhena/Hesperia region at $L_s \sim 252^\circ$ due to lifting to the SE of Isidis, then expands as lifting spreads to more northern and southern low and mid-latitudes, as the Hadley circulation (already strong as Mars approaches southern summer solstice) and associated zonal winds increase in strength due to the greater dust forcing. Once the storm becomes global, the strongest lifting occurs at high southern latitudes, where dust-driven tidal forcing results in strong surface winds, and where the simulated cap edge sits at this time of year. Unlike the early global storm, the late global storms have truly planet-wide dust coverage, due largely to stronger south–north high latitude transport by the meridional circulation at the later time of year. Also unlike the early major storms, the late major storms do not match any regional storm type in time or location. Type 1 and 4 regional storms include dust clouds in Isidis, but occur much earlier or later, and result from lifting inside (not SE of) Isidis. Type 3 storms are closest in time, ending shortly before $L_s \sim 252^\circ$, but involve southern cap edge lifting.

In summary, both late major storms begin as lifting to the SE of Isidis, and expand by activating more lifting in low-to-mid northern and mid-to-high southern latitudes. Their onset pattern does not match any regional storm type, and they occur in a

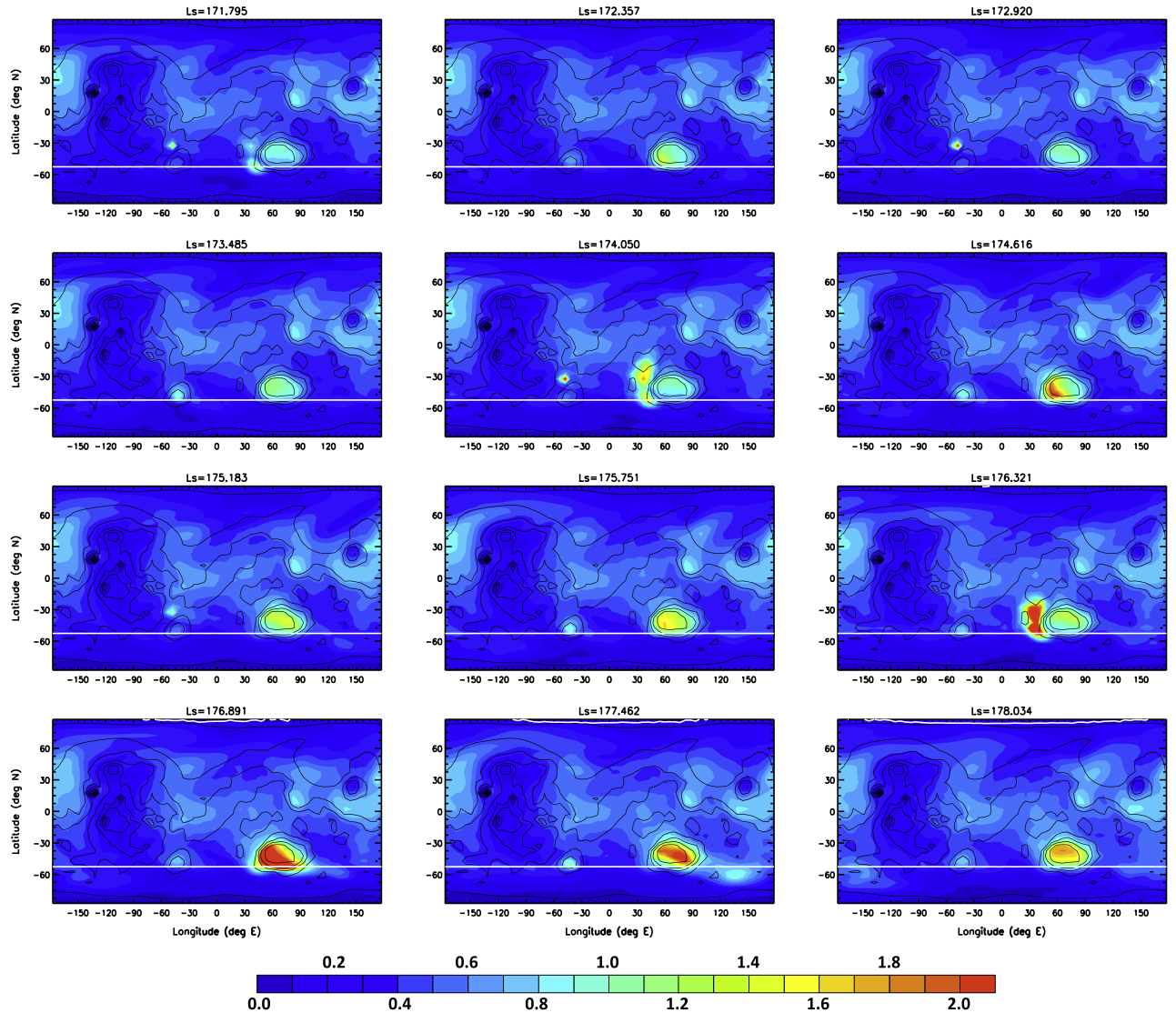


Fig. 16. As in Fig. 13, but showing dust opacity every sol from $L_s \sim 172^\circ$ to 178° in year 24, showing the development of three type 7 pre-spring Hellas regional storms.

period ($L_s \sim 250$ – 308°) lacking any simulated regional storm activity. A potential explanation for the lack of regional storms – at least over the start of this period – may be the relatively uniform, moderately high background dustiness in most years. Storm onset involves positive feedbacks on wind stress lifting, but localized lifting has less impact (in terms of producing strong temperature gradients and hence winds) in a dusty versus a clear atmosphere. Onset of the late global storms may thus be due to unusually strong initial dust lifting at this time in some years, triggering far stronger positive feedbacks on wind stress lifting, and overwhelming the moderating effects of the background dust loading.

4.3.6. Comparison with observed regional and major dust storms

Fig. 20 shows a comparison between storms simulated in Stage O years 21–30 and storms observed in MY 24–30 as identified in WR13. Points of agreement include: type 1 (northern frontal) storms are simulated from $L_s \sim 187^\circ$ to 228° , similar to the observed period of $L_s \sim 180$ – 240° ; no storms are simulated or observed from $L_s \sim 40^\circ$ to 135° , and only global storms from $L_s \sim 250^\circ$ to 305° ; as observed, late global storms are simulated during a period when no regional storms occur; simulated type 4

(late winter northern) storms match the timings of those observed; small storms are simulated and observed in both hemispheres in early northern spring (type 5 storms), though the number of observed storms is fewer; and southern regional storms are simulated and observed in the period $L_s \sim 158$ – 185° (type 6 and 7 storms). However: the size and number of simulated type 4 (late winter northern) storms are much smaller than those observed; more southern hemisphere type 2 or 3 regional storms are simulated than observed from $L_s \sim 209^\circ$ to 250° ; no regional storms are simulated from $L_s \sim 135^\circ$ to 158° , despite numerous (mostly southern) regional storms being observed; and although simulated storm types 6 and 7 involve southern hemisphere lifting just before southern spring equinox, none develop into very early global storms as observed in e.g. MY 25. The timing and location of type 7 (pre-spring Hellas) storms, simulated every year with varying intensity, are particularly suggestive of the earliest global storms observed, yet none expand to become global. This suggests we may be missing a process that effectively ‘weights’ more wind stress lifting to occur earlier in the year. Kahre et al. (2012) suggest this could be produced by the inclusion of radiatively active water ice clouds, though investigating this is beyond the scope of the present work.

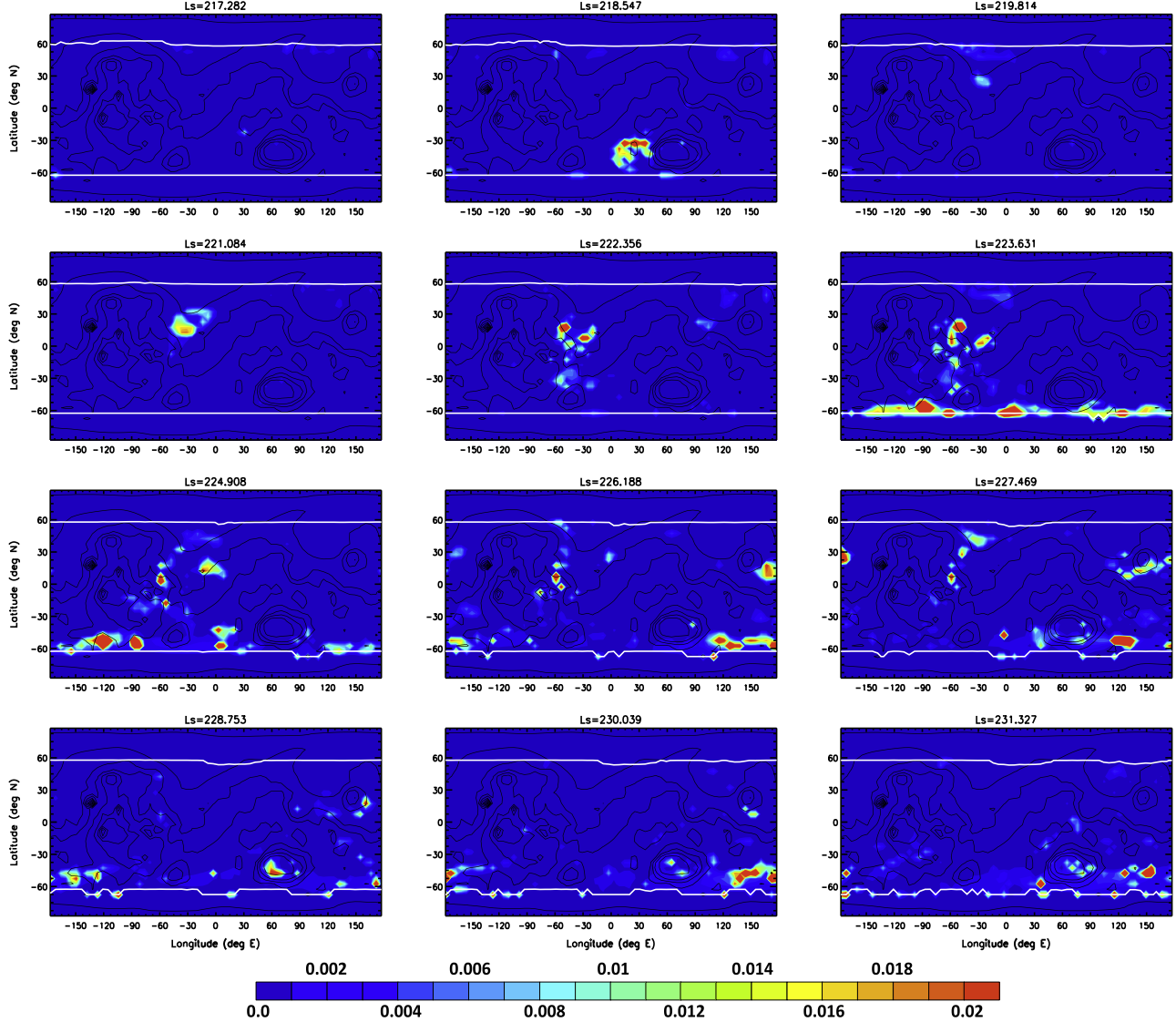


Fig. 17. Maps of cumulative wind stress dust lifting (in kg m^{-2} over the preceding 2-sol period) shown at intervals of 2 sols from $L_s \sim 217^\circ$ to 231° in year 24 of FINDUST Stage O, covering the onset and growth phases of the year 24 early global storm. Visible dust opacities for the same period are shown in the lower four panels of Fig. 14. Note that color contours saturate above 0.02 kg m^{-2} per 2 sols. (For interpretation of the references to color in this figure legend, the reader is referred to the web version of this article.)

The low frequency of major storms and consequent lack of good statistics makes it difficult to assess the plausibility of our simulated major storms. Table 4 shows a summary of observed and simulated global storm onset times and locations. We simulate three early major storms beginning between $L_s \sim 210^\circ$ and 220° with initial dust clouds in Noachis/Hellas and (in two cases, one being the global storm) Acidalia–Chryse, which could possibly be consistent with the MY –24 (1909) global storm (observed to begin at $L_s \sim 207^\circ$, possibly in Hellas), though seems inconsistent in terms of onset region with the first MY 12 global storm, which was observed to begin at $L_s \sim 204^\circ$ but in SW Thaumasia (at $\sim 85^\circ\text{W}$, 45°S). The simulated onset regions appear more consistent with storms observed later in the storm season, e.g. at $L_s \sim 249^\circ$ in MY 1 and at $L_s \sim 260^\circ$ in MY 9 and 28. Onset of the MY 28 storm in particular is strikingly similar to that of our simulated year 24 storm, with both seeming to initiate from a combination of Chryse and Noachis regional events. As noted, however, the timing does not match.

While we do simulate storms later in the storm season, they instead begin in the Isidis/Tyrrhena/Hesperia region. This region has been noted as one of several preferred onset locations of global

dust storms (e.g. Cantor, 2007), but is not as common as Noachis/Hellas from $L_s \sim 250^\circ$ to 270° , or in the western hemisphere (e.g. Solis/Thaumasia) from $L_s \sim 270^\circ$ to 300° . The lack of simulated global storm onset in the western hemisphere implies a bias in MarsWRF toward dust lifting in the region to the SE of Isidis rather than in Solis/Thaumasia. This may be due to either unrealistic MarsWRF wind stresses in one or both regions, or an unrealistic lack of surface dust at the observed onset locations by this Stage of FINDUST. On the other hand, we agree with observations in that these later storms appear to develop in periods when no regional storms occur.

Overall, the simulation captures many of the observed regional storm ‘families’ as well as two large gaps in regional storm activity and onset of late major storms in a normally storm-free period. Onset and growth of simulated major storms also match many aspects of those observed, although there are mismatches in either onset times or locations. The simulation also overpredicts southern regional storm activity in local spring, underpredicts late winter storm activity in both hemispheres, and does not capture the onset timing of the earliest major storms observed, although small Hellas

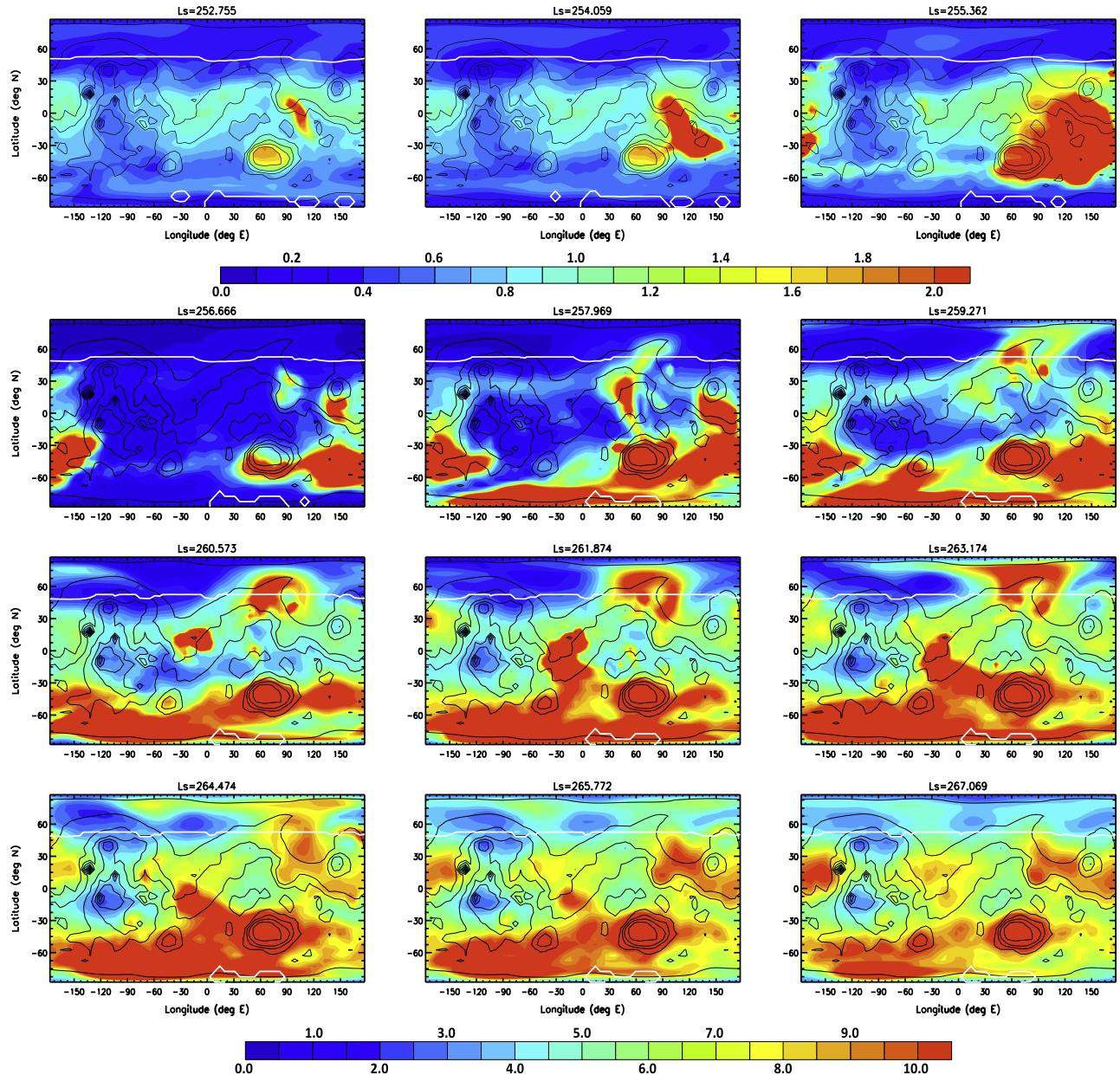


Fig. 18. As Fig. 13, but showing dust opacity for year 23, $L_s \sim 253\text{--}267^\circ$, covering onset and growth of a late global storm. Note a fivefold increase in contour intervals after onset to better show the growth phase.

storms simulated around southern spring equinox are suggestive of their initial stages.

4.4. Surface dust rearrangement, modes of surface dust replenishment, and interannual variability in years 21–30 of FINDUST Stage O

The similarities to observed storms suggest that FINDUST Stage O may be useful as a proxy for the real martian dust cycle. In this section we examine the underlying dust lifting processes and feedbacks responsible for both evolution and interannual variability of the simulated storms, focusing on the impact of time-varying, finite surface dust cover.

4.4.1. Finite surface dust and interannual variability

As the primary source regions change over decades of surface dust rearrangement, interannual variability increases in FINDUST.

One cause is the permanent exhaustion of grid points at which predicted lifting greatly exceeds deposition due to the low (0.02 Pa) threshold being exceeded too much. At the new primary source grid points, peak wind stresses exceed threshold relatively little, allowing deposition to balance lifting, and producing increased sensitivity to slight variations in wind stress. This greater interannual variability exists when the threshold is comparable to peak wind stresses in primary source regions. Note that interannual variability in infinite dust simulations occurs by the same mechanism, except in that case the primary source regions are regions with the highest wind stresses, thus a much higher threshold is required. The second cause of interannual variability is the temporary exhaustion of some source grid points, which then have dust available at a certain L_s in some years but not others. Thus the high interannual variability in the dust storms produced in simulation FINDUST is due both to:

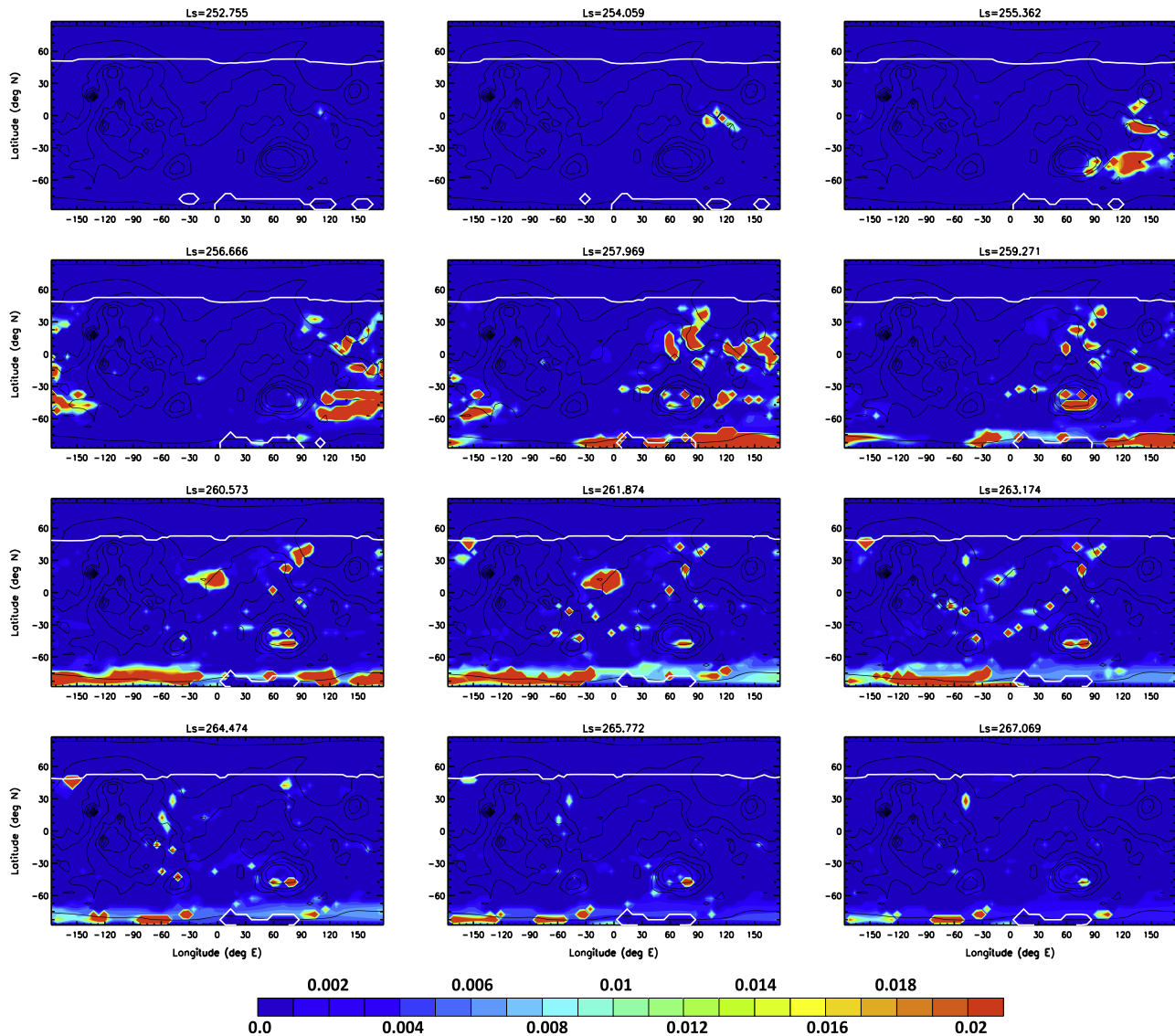


Fig. 19. Wind stress lifting as in Fig. 17, but now showing the same period as in Fig. 18 (year 23, $L_s \sim 253\text{--}267^\circ$) covering the onset and growth phases of the year 23 late global dust storm.

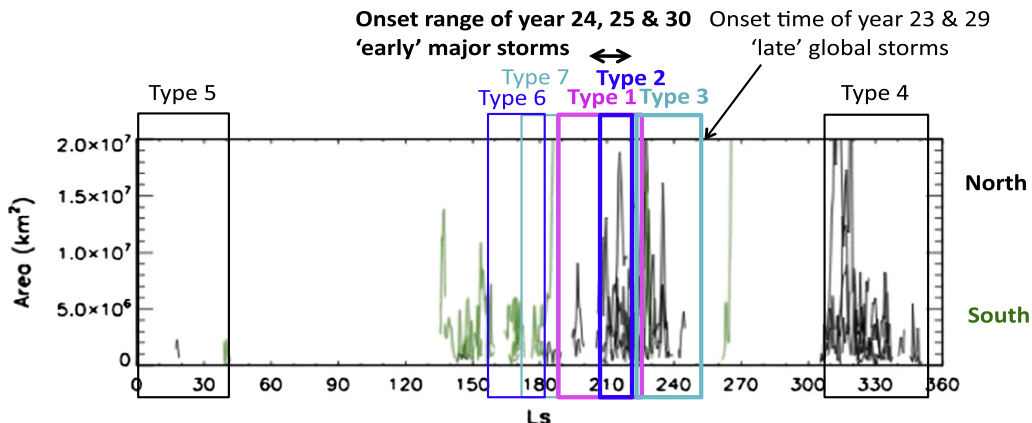


Fig. 20. Adapted from Fig. 3 of WR13 showing daily total areas of thick dust contributing to dust storm sequences as a function of L_s for the 65 large dust storms identified in MOC and MARCI images in MY24–30. Northern and southern sequences are in black and green respectively. Overlaid on the original figure are boxes showing the seasonal timings of the 7 simulated regional storm types identified in Section 4.3.4. Also shown are the onset times of the simulated early and late major storms in Stage O years 21–30. (For interpretation of the references to color in this figure legend, the reader is referred to the web version of this article.)

Table 4

Summary of observed global storm onset since 1908 (see Section 1.1.2 for references), and global storms simulated in years 21–30 of FINDUST Stage O. Onset locations observed telescopically (denoted by *) are typically less accurate than those observed by spacecraft, which permit better resolution and viewing angles making it easier to see earlier stages of the storm. Note that the temporal spacing between observed storms often reflects availability of good observations (rather than frequency of global storm occurrence) outside of periods with continuous spacecraft observations, i.e., prior to 1977 and between 1982 and 1997.

Mars year (Earth year)	Onset time (in L_s) (°)	Onset location(s)
<i>Observed global storms</i>		
–24 (1909)*	207	Possibly Hellas
–16 (1924)*	311	NW Hellas
1 (1956)*	249	NE Noachis/to the NW of Hellas
9 (1971)	260	NW of Hellas/NW Hellas
10 (1973)*	300	NW Solis/Claritas-Daedalia
11 (1975)*	270	S Thaumasia
12 (1977a)	204	SW Thaumasia
12 (1977b)	268	NE Thaumasia
15 (1982)*	208	Probably southern hemisphere
25 (2001)	184	Southern cap edge/Hellas
28 (2007)	260	Noachis/Hellas and Chryse
FINDUST Stage O year	Onset time (in L_s) (°)	Onset location(s)
<i>Simulated global storms</i>		
Year 23	217	Noachis/Hellas and Acidalia–Chryse
Year 24	252	Isidis/Tyrrhena/Hesperia
Year 29	252	Isidis/Tyrrhena/Hesperia

I Enhanced sensitivity to intrinsic atmospheric interannual variability when the new primary source grid points are such that thresholds are less regularly exceeded, and/or

II Changes in the pattern of surface dust availability from one year to the next.

Interconnections between depletion and future lifting, storms, the circulation, and replenishment of dust at source locations make it impossible to completely separate (I) and (II). For example, lack of sufficient surface dust at a key location during storm onset will impact the amount and distribution of dust lifted, and hence the circulation, and may determine whether a global storm develops or not, regardless of dust availability at grid points that form the primary source regions over the course of the entire storm.

Despite these complications, we attempt to identify the dominant contributor to the interannual variability of major storms in FINDUST Stage O in Sections 4.4.3 and 4.4.4.

4.4.2. Overview of surface dust cover changes in years 21–30 of FINDUST Stage O

Fig. 21 shows the top 100 dust contributors over years 21–30 of Stage O. The top ranked grid point and several other top contributors are located in Eridania (~120–180°E, 30–65°S), within the southern hemisphere ‘zonal collar’ of peak winds associated with the southern summer Hadley circulation. The second ranked grid point and many other top contributors are located on the slopes of Hellas, where seasonal, slope and cap edge winds combine to produce strong flows. The third ranked grid point and some other top contributors are located in the Utopia–Isidis meridional corridor running to the east of Syrtis Major, a region with strong WBC flows. Other top contributors are in Aeolis (~120–180°E, 0–30°S), Chryse, and in the WBC region between Elysium and Tharsis.

Fig. 22 shows the variation of surface dust, wind stress lifting and dust deposition over years 21–30 at the top three ranked grid points, which together contribute just over 5% of the dust lifted during this period. This is far lower than the ~33% contributed by the top three grid points in INFIDUST, due to the less concentrated and more widespread wind stress lifting in FINDUST Stage O. The general behavior is similar to that described for lower ranked dust contributors in INFIDUST (Section 3.3.2): rapid depletion during major dust storms, often followed by rapid accumulation if dust fallout exceeds lifting during the storm’s later stages, and gradual accumulation between storms, often with a strong seasonal dependence. The difference is that in FINDUST Stage O even the top ranked grid points show dust accumulation as well as depletion, since the primary source regions experience far greater replenishment than in INFIDUST. The top three grid points differ in terms of their dust contribution to the major storms, with the 2nd and 3rd ranked points contributing far more to the late storms but the 1st point contributing more equally to both types. The 2nd point is temporarily exhausted by the year 23 and 29 storms, so finite dust availability may have hastened their end. However, replenishment is rapid at this location, hence the small amount of lifting in other years was not due to lack of dust but variability elsewhere.

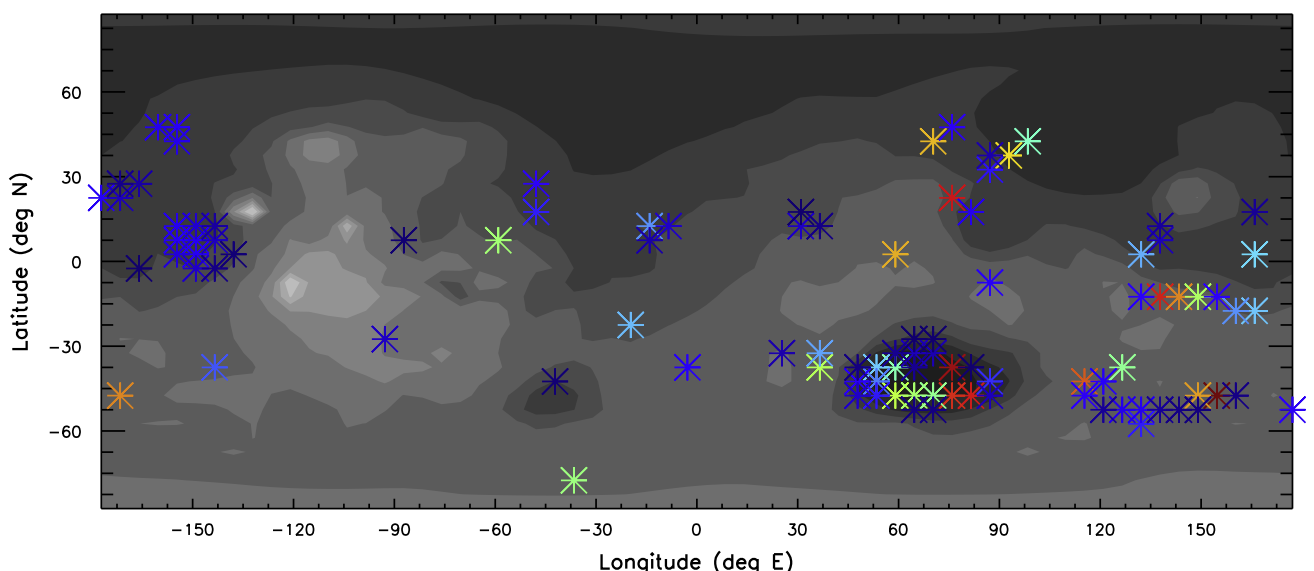


Fig. 21. As in Fig. 5, but showing the top 100 dust contributors for years 21–30 of FINDUST Stage O.

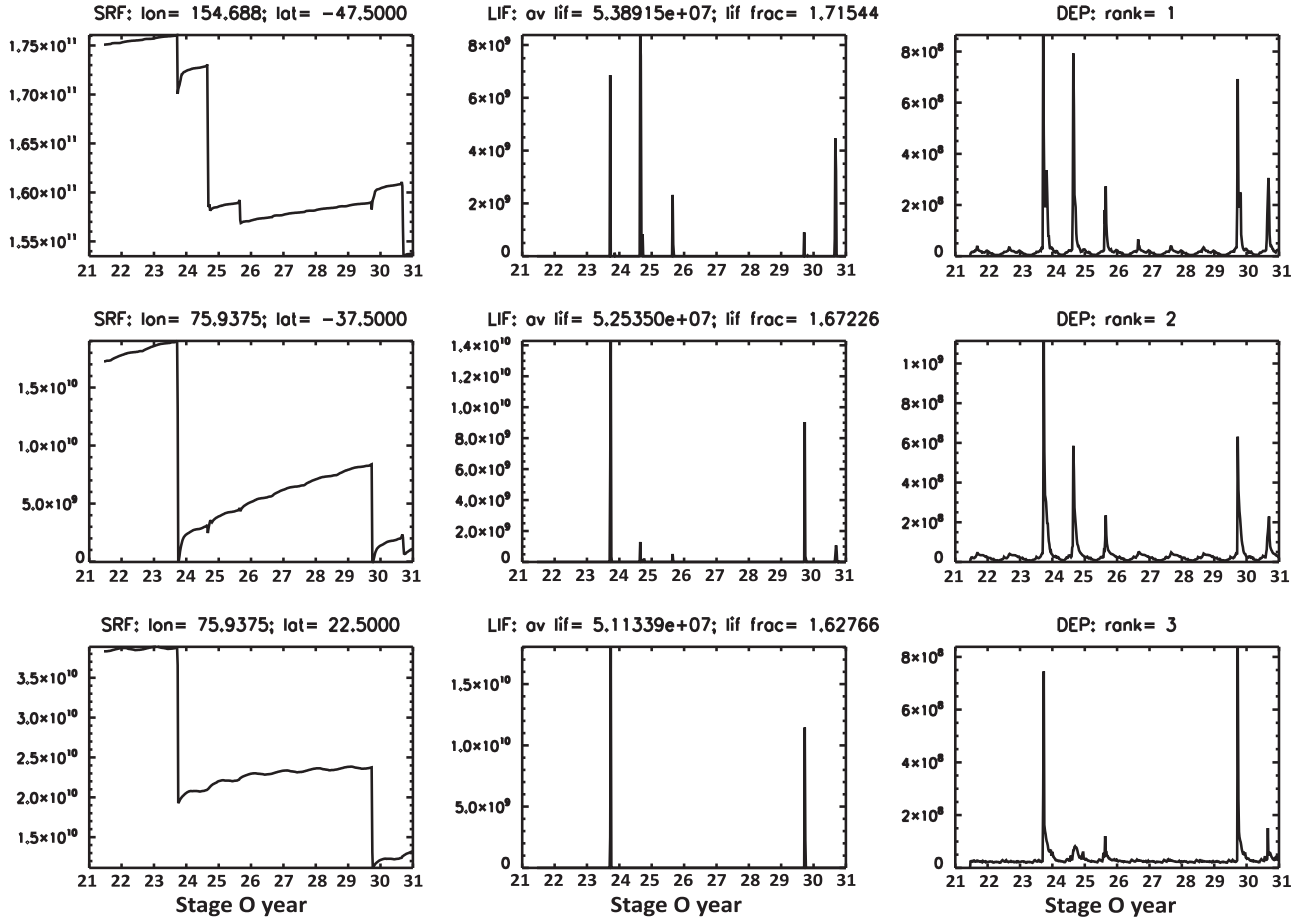


Fig. 22. As Fig. 6, but now showing the surface, lifted, and deposited dust over years 21–31 of FINDUST Stage O, for the top 3 dust contributor grid points over that entire period. Top row: 1st ranked. Middle row: 2nd ranked. Bottom row: 3rd ranked. Note the different y-axes between plots; e.g., the y-axis does not begin at zero for the 1st and 3rd ranked grid points, as they do not fully deplete during this period.

Note that temporary exhaustion of dust at a grid point does not preclude significant contributions to future storms. The complete time evolution of surface dust must be considered to assess a region's role in the dust cycle, rather than merely the instantaneous (or even annual mean) dust cover there. Fig. 23 shows the long-term behavior of surface dust at the top ranked grid points in years 21–30, now shown over the whole of Stage O (80 years). The 2nd ranked grid point is temporarily exhausted many times, but often has periods of several years without any rapid depletion events. This lets gradual accumulation build up enough dust for it to become a primary contributor again. Fig. 24 shows more examples, now for the grid points ranked 32nd, 47th and 66th over years 21–30. Unlike the top ranked points, these have large dust gains during storm seasons and are dust-free for a significant portion of the year. In the case of the 32nd ranked point, on the NW slopes of Hellas, peak lifting (resulting in exhaustion) occurs in northern summer during southern cap-edge lifting, although some depletion also occurs due to strong wind stress enhancement during major storms. However, dust lost during such storms is soon replenished by rapid accumulation during storm decay, or by gradual accumulation which occurs here over most of the year. The 47th ranked point, just west of Tharsis, both gains and loses the most dust during the storm season. The surface here is dust-free nearly all year, but gains so much dust due to fallout of the year 23, 24 and 29 global storms that it shows up as a major contributor during the later stages of the same storms, when all the dust deposited is removed again. A hybrid situation occurs at the 66th ranked point, which gains significant dust every storm season (more so when a large

storm occurs), but loses all of it near the start of the following year, rather than during the storm season itself.

By contrast, dust at the 3rd ranked point shows a clear downward trend when all years of Stage O are considered (Fig. 23). Once exhausted for the first time (in year 32), it never recovers sufficiently, even over multiple decades, to contribute significantly again. Such behavior at this and other grid points leads to the eventual cessation of storms by the end of Stage O (Section 4.3.2). The 1st ranked point is never exhausted during Stage O, thus lack of dust cannot explain why dust lifting here is greatly reduced in later years. Rather, depletion of other grid points in Stage O leads to less lifting elsewhere and thus fewer and/or weaker storms, resulting in less intensification of the Hadley circulation and associated surface wind stresses in the southern mid-latitudes where the 1st ranked point is located. Changes in dust cover and lifting at one grid point can affect results for all, even distant ones, via changes in dust loading that impact both the global circulation and worldwide dust deposition. Such interconnections are why success – in the sense of achieving a steady state surface dust distribution – cannot be claimed until *all* surface grid points are in steady state.

4.4.3. Variation of dust at key grid points during the onset phase of major storms

Here we examine the replenishment of dust in key onset regions for the simulated early and late major storms, and investigate to what extent surface dust availability may be controlling storm onset. Fig. 25 shows the top 100 ranked source grid points during onset of each of the five major storms, grouped according

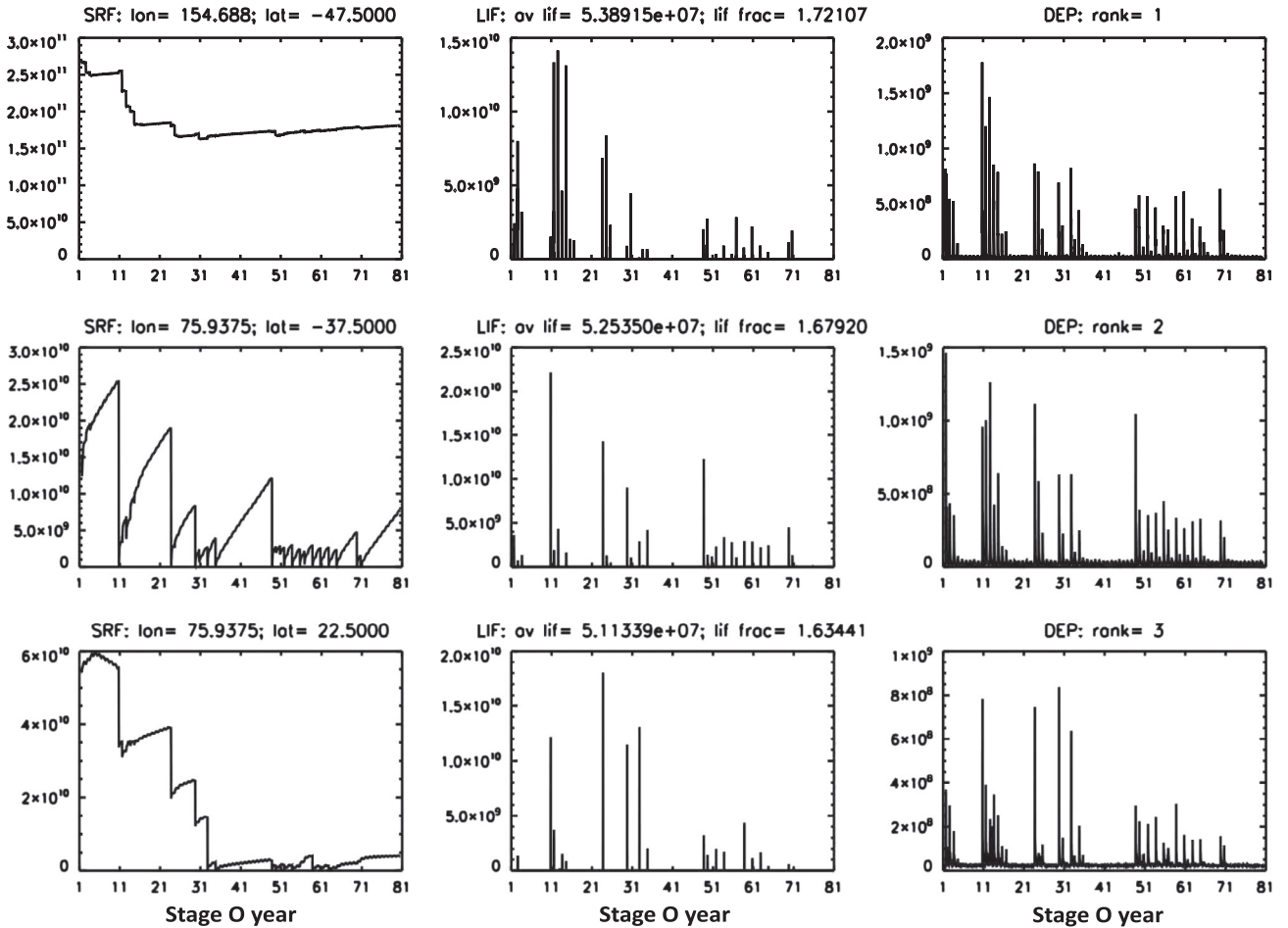


Fig. 23. As Fig. 22 but showing behavior at the same grid points for the whole of FINDUST Stage O.

to storm type. As indicated in Section 4.3.5, there is a clear distinction between the pattern of source regions for the early and late storms. All three early storms have high-ranked grid points in the eastern Noachis (Hellespontus) region, with lower-ranked points on the northern slopes of Hellas, in Acidalia and Utopia, and along the southern cap edge. The year 30 storm has two high-ranked and several lower-ranked points in Isidis, while the year 24 and 25 storms instead have high-ranked grid points in Chryse. The basic pattern is thus of key source grid points in Noachis–Hellas and in at least one of the meridional corridors used by cross-equatorial storms. The onset phases of the two late storms show even more similarities, with all but the lowest-ranked points located in Isidis/Tyrrhena/Hesperia ($\sim 90\text{--}150^\circ\text{E}$, $15^\circ\text{N}\text{--}45^\circ\text{S}$). The main differences between the late storms are the ranking of grid points to the east of Hellas, and the presence of a number of (lower-ranked) source points on the N/NE slopes of Hellas in year 23 versus their location on the E/SE slopes in year 29.

4.4.3.1. Surface dust availability and onset of early major storms. Focusing on the onset phase of the year 24 early storm, surface dust availability is a factor for 86 of the top-100 ranked grid points, which contribute $\sim 76\%$ of the storm onset dust. All 86 are exhausted at least once in years 21–30, 80 during the year 24 storm and many in every year. In the period leading up to the year 24 storm, 81 such points gain net dust due to the year 23 global storm. Two examples are shown in Fig. 26a and b. The 13th ranked point has very little dust at the start of the year 23 storm season, but gains substantial dust during fallout of the year 23 storm, which is then available for onset of the year 24 storm. The 20th

ranked point is exhausted during the growth phase of the year 23 storm, but enough dust is deposited during its decay phase to produce net dust gain overall. Only 10 of the top 100 ranked points have any net dust loss due to the year 23 storm, and in most cases this loss is small. E.g. at the 6th ranked point (Fig. 26c) most of the dust lost to the year 23 storm is replenished during fallout of the same event.

Similar behavior exists between the year 29 late and year 30 early storms. Thus the presence of a late major storm in one year seems vital to replenish key source regions for an early major storm in the next. Fig. 27 demonstrates this further by showing the top 30 ranked grid points for year 24 storm onset, plotted over (a) the mean surface dust cover in years 21–30, and (b) the dust gained due to the year 23 storm (from year 23 $L_s = 180^\circ$ to year 24 $L_s = 180^\circ$) as a percentage of the mean. Most key source grid points for onset of the year 24 storm are in regions with low mean surface dust cover but high percentage gains due to the year 23 late storm. I.e., without the year 23 late storm, the same intensity of early storm lifting in Chryse and Noachis in year 24 could not have occurred.

Even if fallout from a late global storm is necessary to replenish key source regions for early major storm onset, dust availability in such regions may not be sufficient for an early major storm to occur. E.g., no early (or late) major storms occur in years 26–28, yet many key grid points for onset of the year 24 early storm have adequate dust availability (see e.g. Fig. 26a and c). However, some key onset points do lose all their dust cover each storm season in years 26–28, and large-scale fallout following another late global storm (in year 29) appears necessary before they regain the dust

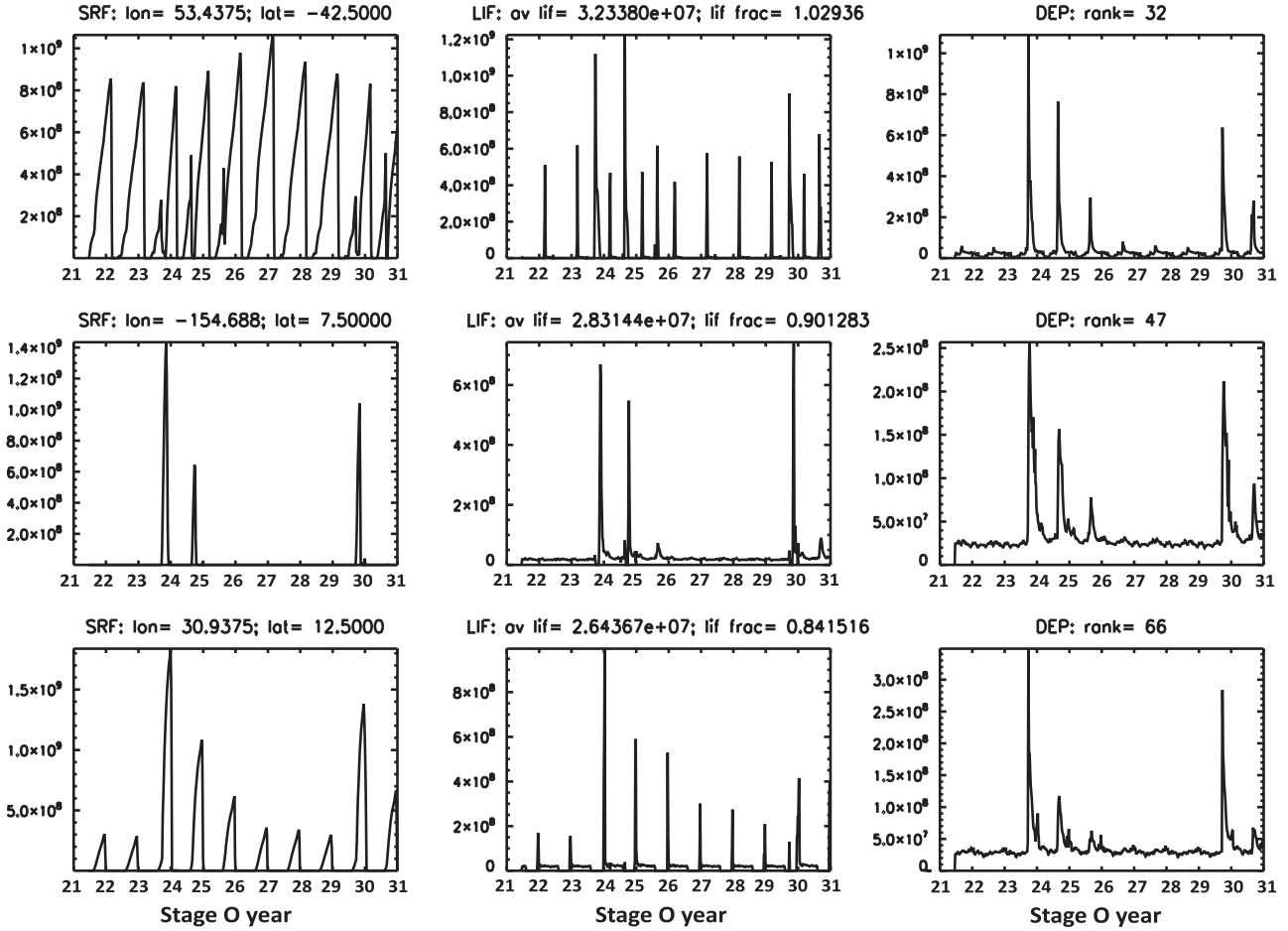


Fig. 24. As Fig. 22 but now showing the 32nd, 47th and 66th ranked grid points for years 21–31.

levels they had prior to the year 24 storm. This is true at 56 of the top 100 ranked points for onset of the year 24 storm, suggesting that lack of surface dust availability may indeed have prevented onset of an early major storm in years 26–28. The non-global nature of the year 25 early major storm may also be due to it following an early (rather than late) global storm in year 24. Differences in pattern, timing and dust load between early and late global storms will clearly impact the pattern of deposition, hence affect replenishment of key regions for early storm onset. It also seems reasonable that global storms of the same type, with similar source regions, are less likely to occur in adjacent years, since source regions have been recently depleted. However, the year 30 early storm also fails to become global, though lack of dust in key regions for early major storm growth may be a bigger factor here (see Section 4.4.4).

4.4.3.2. Surface dust availability and onset of late major storms. Lack of surface dust in key source regions for late major storm onset does not appear to have prevented such a storm occurring in e.g. the period between the year 23 and year 29 late storms. Focusing on the onset phase of the year 23 storm, 13 of the top 14 ranked grid points (contributing ~82% of the storm onset dust supplied) have ample dust in years 24–28, with the remaining point (ranked 9th) only exhausted temporarily in year 25. The situation is very similar when considering the year 29 storm. It is tempting to assume that the ‘recovery time’ needed for key onset (or growth) source regions will prevent the same major storm type from occurring in adjacent or even nearby years. However, replenishment of surface dust appears to be extremely efficient in the key source regions for onset of the late global storms. This suggests

that their onset may be more strongly linked to intrinsic atmospheric variability (e.g. the strength/timing of strong wind stresses SE of Isidis; see discussion in Section 4.3.5) than to surface dust availability.

4.4.4. Variation of dust at key grid points during the growth phase of major storms

Here we examine the replenishment of dust in key growth regions for the simulated early and late major storms, looking at whether dust availability controls storm growth. Fig. 28 shows the top-100 ranked grid points for the growth phases of each of the five major storms, grouped according to storm type. We define the growth phase as the period from when secondary dust lifting regions are first activated to when strong lifting ceases as the storm begins to decay, giving: $L_s \sim 255\text{--}277^\circ$ (year 23), $L_s \sim 222\text{--}264^\circ$ (year 24), $L_s \sim 217\text{--}255^\circ$ (year 25), $L_s \sim 255\text{--}277^\circ$ (year 29), and $L_s \sim 220\text{--}256^\circ$ (year 30). As with storm onset (Fig. 24), there is a clear distinction between the pattern of source regions for growth of early and late major storms. The main differences are more late storm lifting in the Hellas basin (particularly the S and E), in and to the E and NE of Syrtis, and in Aeolis and Elysium. There is also more late storm lifting south of ~70°S and more early storm lifting from ~45 to 70°S, probably reflecting the shifting location of the seasonal cap edge.

Although distinct from that of the early storms, the growth pattern differs between the two late storms. Despite their onset phases being very similar, the year 23 and 29 storms share only 47 top-100 ranked points during their growth phase. Significant lifting occurs in Chryse/Meridiani and little in Amazonis during storm growth in year 23, but this is reversed in year 29. Also, while

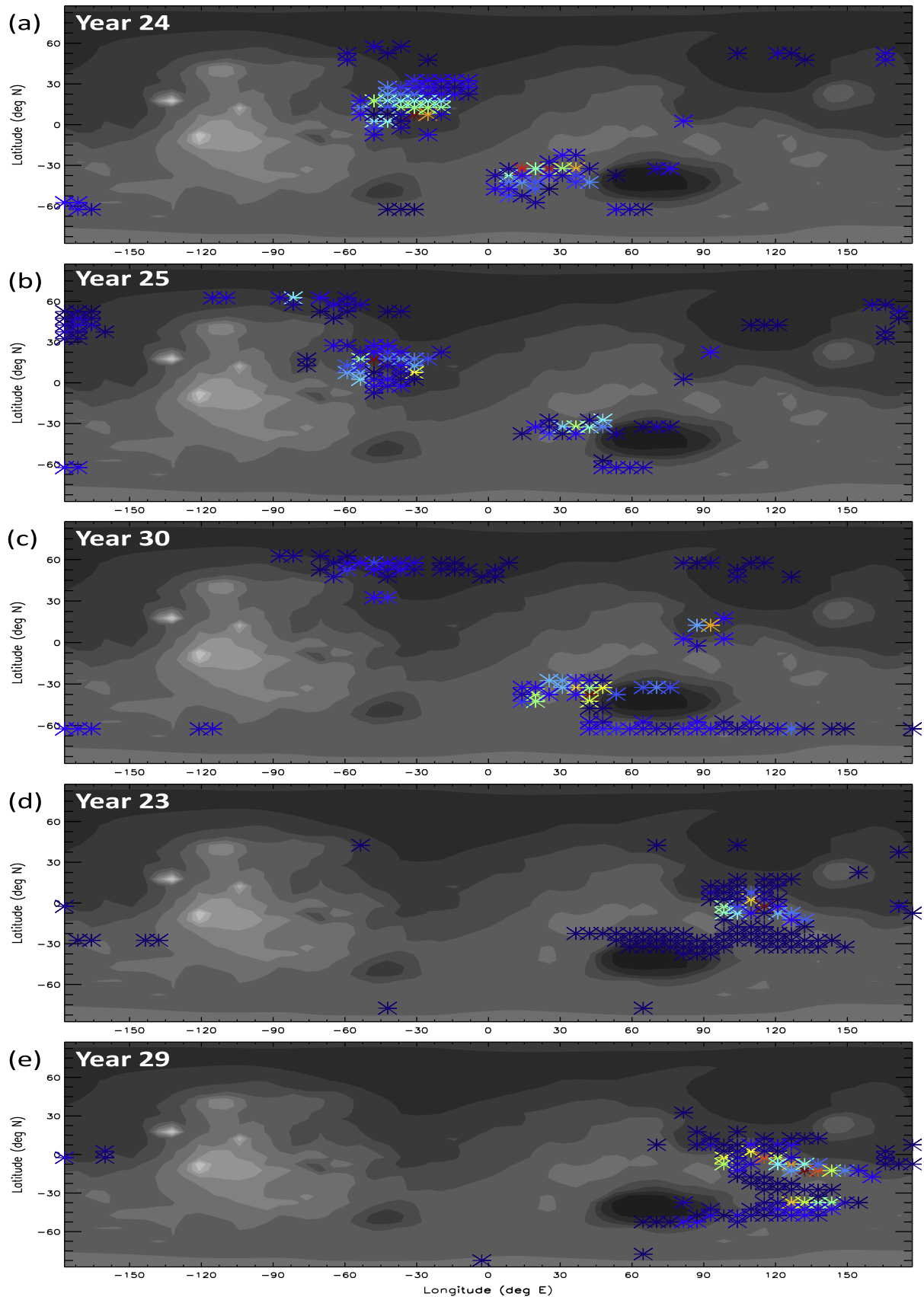


Fig. 25. As in Fig. 5 but showing the top 100 ranked dust source grid points for onset of the five major storms in Stage O years 21–30. (a), (b) and (c) show the top sources for the onset period (lasting respectively ~ 8 , 12 and 10 sols) of respectively the year 24, 25 and 30 early storms. (d) and (e) show the top sources for the onset period (~ 5 sols in both cases) of respectively the year 23 and 29 late storms.

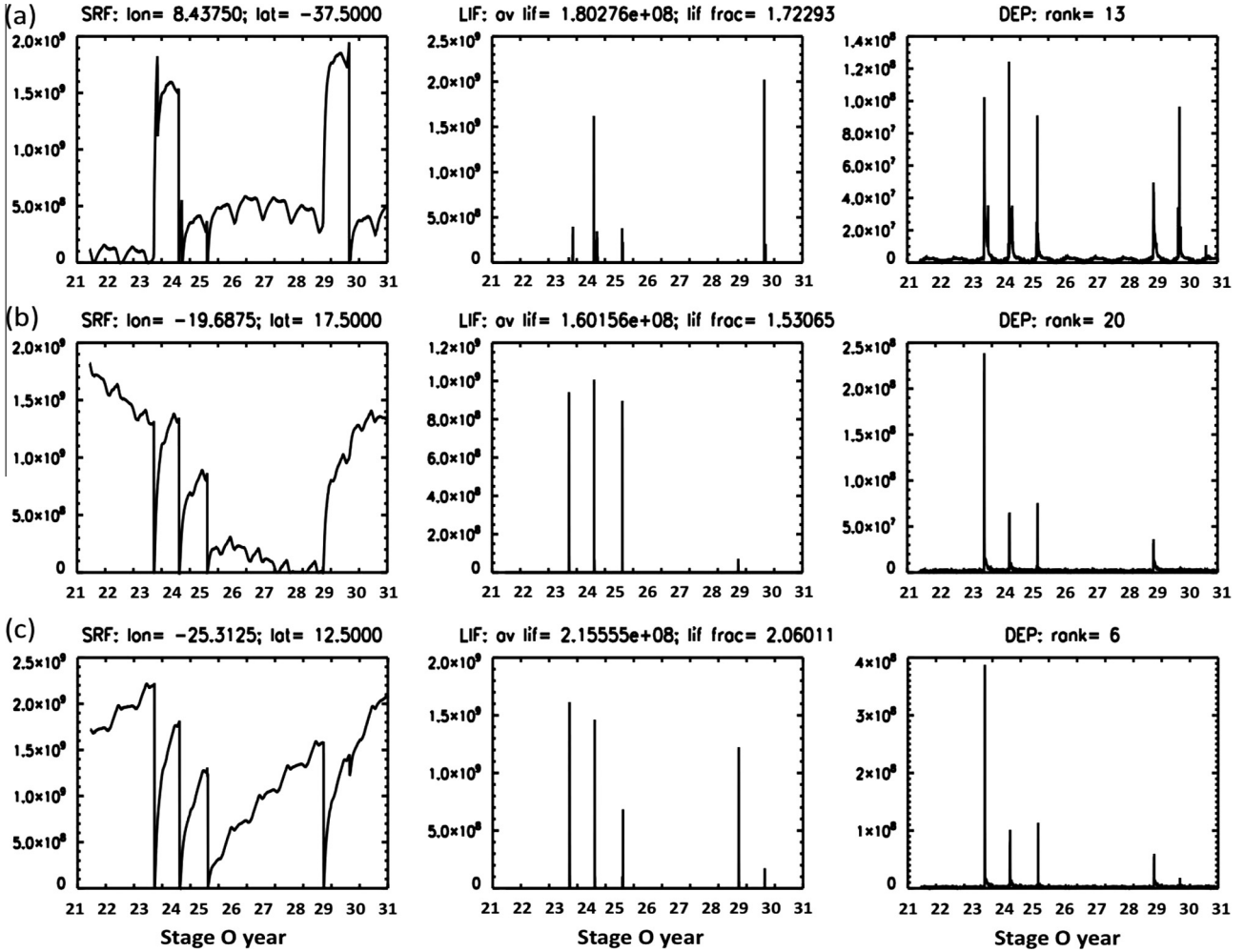


Fig. 26. As in Fig. 22, but now showing the grid points ranked (a) 13th, (b) 20th and (c) 6th in terms of their dust contribution during the onset phase ($L_s \sim 217\text{--}222^\circ$) of the year 24 early global storm.

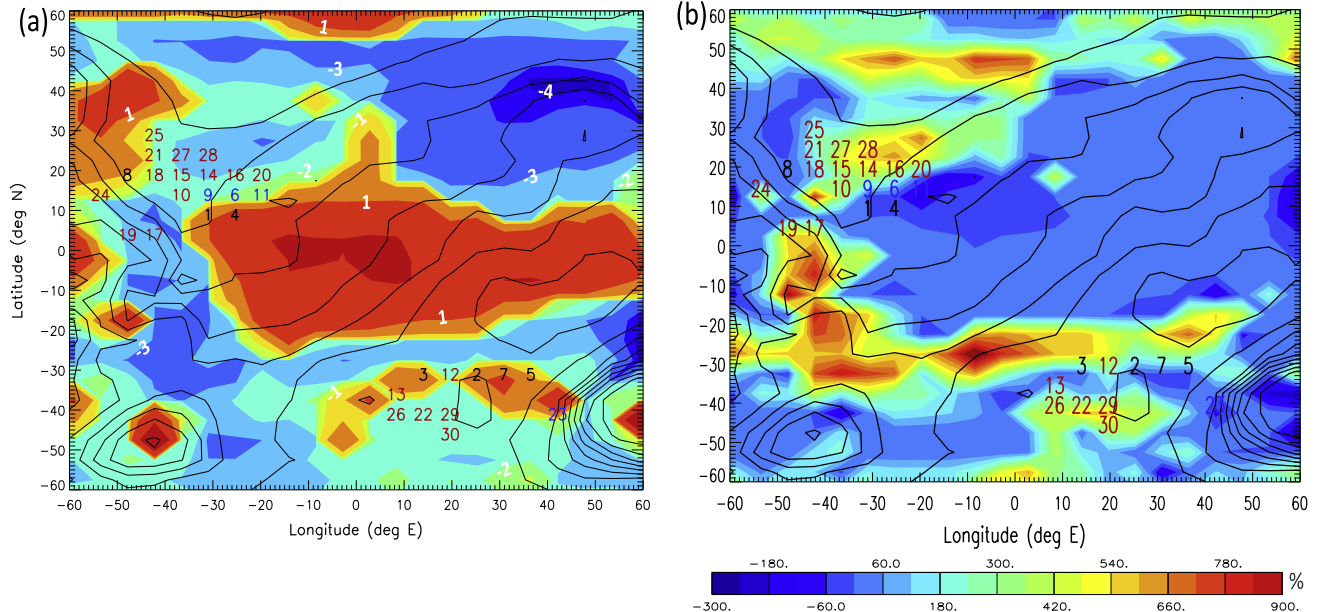


Fig. 27. The area shown covers the main Chryse and Noachis source regions for the year 24 global storm, with topography contours in black. Shaded color contours are (a) log₁₀ of mean surface dust in kg m⁻² over years 21–30 (labeled in white), and (b) surface dust gain from year 23, $L_s = 180^\circ$ to year 24, $L_s = 180^\circ$, as a % of the mean (see color bar). The top 30 dust contributors to year 24 storm onset are also marked: in black if dust loss and replenishment is not a factor (i.e., if they are never exhausted over this time, which is true for the points ranked 1st to 5th, 7th, and 8th); in blue if net dust losses due to the year 23 storm result in less dust being available for the year 24 event (true for the points ranked 6th, 9th, 11th and 23rd); and red if net gains result in more dust being available (true for all other points shown). (For interpretation of the references to color in this figure legend, the reader is referred to the web version of this article.)

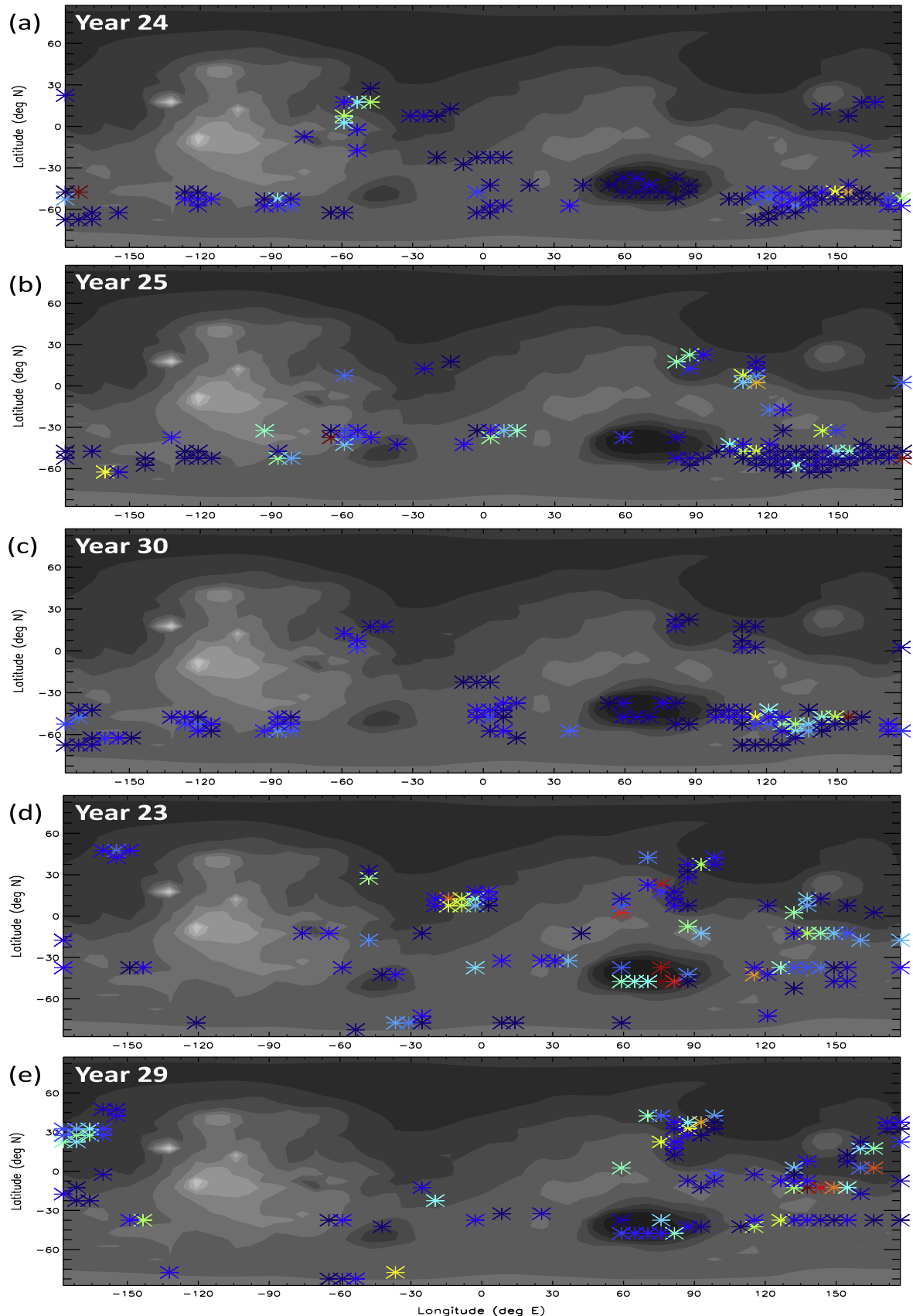


Fig. 28. As in Fig. 24, but now showing the top 100 dust source locations for the growth phases of the five major storms in years 21–30 of Stage O.

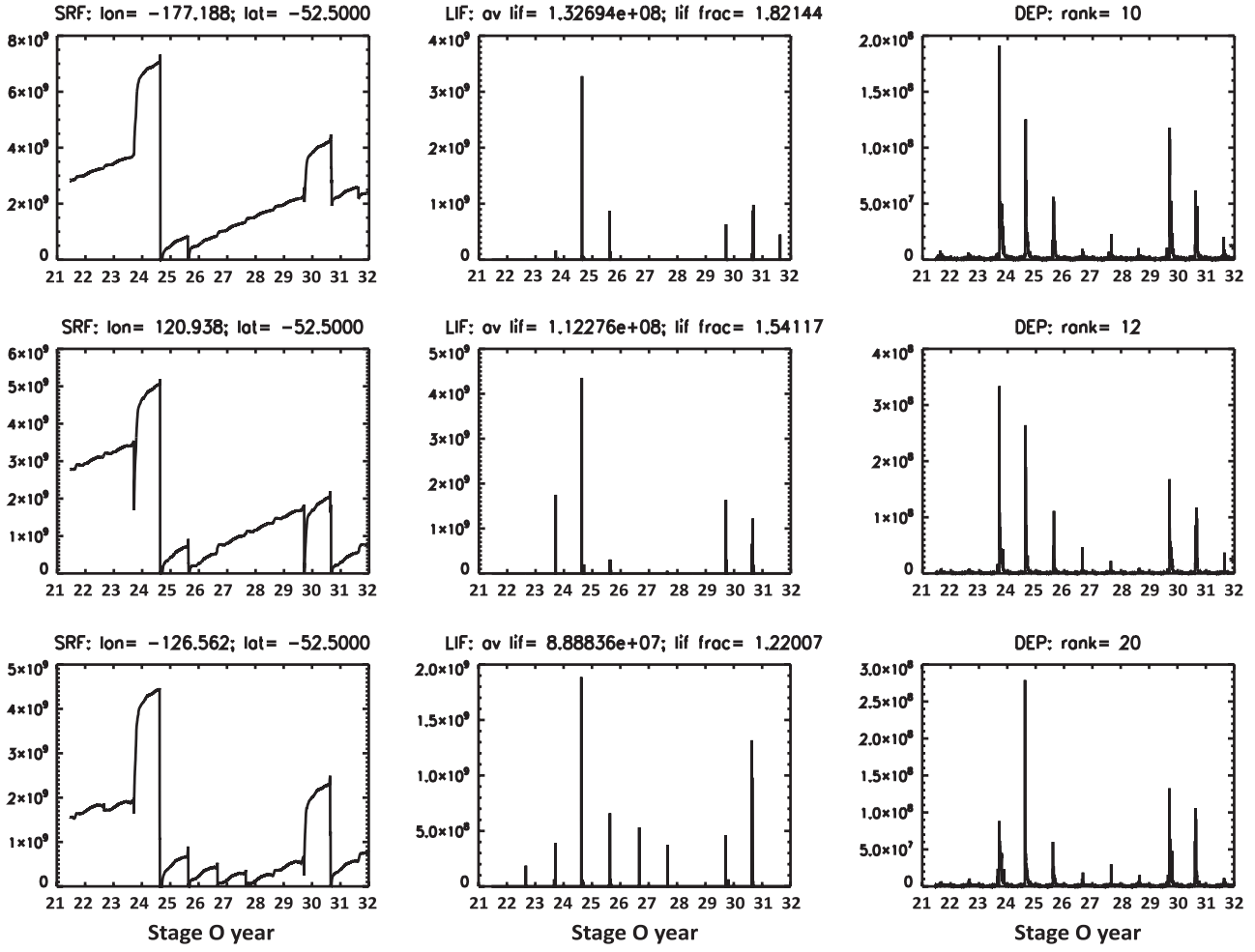


Fig. 29. As in Fig. 22, but showing the grid points ranked 10th, 12th and 20th in terms of their dust contribution during the growth phase ($L_s \sim 222\text{--}264^\circ$) of the year 24 early global storm.

lifting peaks in Hellas, Syrtis and Isidis during storm growth in year 23, it peaks in Hesperia and Aeolis in year 29. Conversely, the growth phases of the early major storms are quite similar to each other, more so even than their onset phases. All three have peak lifting in a southern zonal collar from 35 to 55°S, though the exact location differs, and peak northern lifting in Isidis/Tyrrhena/Hesperia or Chryse.

4.4.4.1. Surface dust availability and growth of early major storms. Focusing on the growth phase of the year 24 early storm, surface dust availability is a factor for well over half of the top-100 ranked grid points, which are exhausted during the storm itself and do not recover immediately. Fig. 29 shows this for three southern mid-latitude grid points, ranked 10th, 12th and 20th. Although the year 23 global storm roughly doubles their surface dust cover, it is still exhausted in year 24, and has only recovered to $\sim 10\%$ of pre-storm levels prior to the year 25 storm season. This may explain why the year 25 early major storm is much smaller than that in year 24, despite the strong similarity in their onset phases. Similar to their onset phase (Section 4.4.3), key source regions for the growth phase of early major storms appear to be replenished far more effectively by fallout of late major storms, particularly in southern mid-latitudes.

4.4.4.2. Surface dust availability and growth of late major storms. As with their onset phase (Section 4.4.3), we find no correlation

between surface dust availability and the growth phase of late major storms. It appears that either no significant dust lifting occurs between $L_s \sim 250^\circ$ and 308° , or lifting SE of Isidis at $L_s \sim 252^\circ$ occurs and leads to a global event. As discussed in Section 4.3.5, the lack of regional storms at this time of year may be due to high background dust levels that suppress the positive feedbacks associated with rapid storm onset. If this can be overcome due to slightly stronger/earlier dust lifting, however, the positive feedbacks on increased dust loading may be larger in this later season (around perihelion, $L_s \sim 251^\circ$, and solstice, $L_s = 270^\circ$) since the circulation is already stronger. I.e., once a storm begins, wind stresses rapidly increase over so much of the planet that the lack of surface dust in some source regions does not prevent the storm from becoming global. This may also explain why the key growth phase source regions differ so much between the year 23 and year 29 storms.

4.5. The long term mean surface dust cover in simulation FINDUST

Section 4.3 compared simulated and observed dust storms, providing some indication of how good a proxy FINDUST Stage O may be for real Mars. We can also assess this by comparing the simulated long-term mean surface dust distribution with indicators of dust cover on Mars. Fig. 30 compares the mean surface dust distribution in Stage O years 21–30 and the observed mean surface albedo over several years from MGS TES (Christensen et al.,

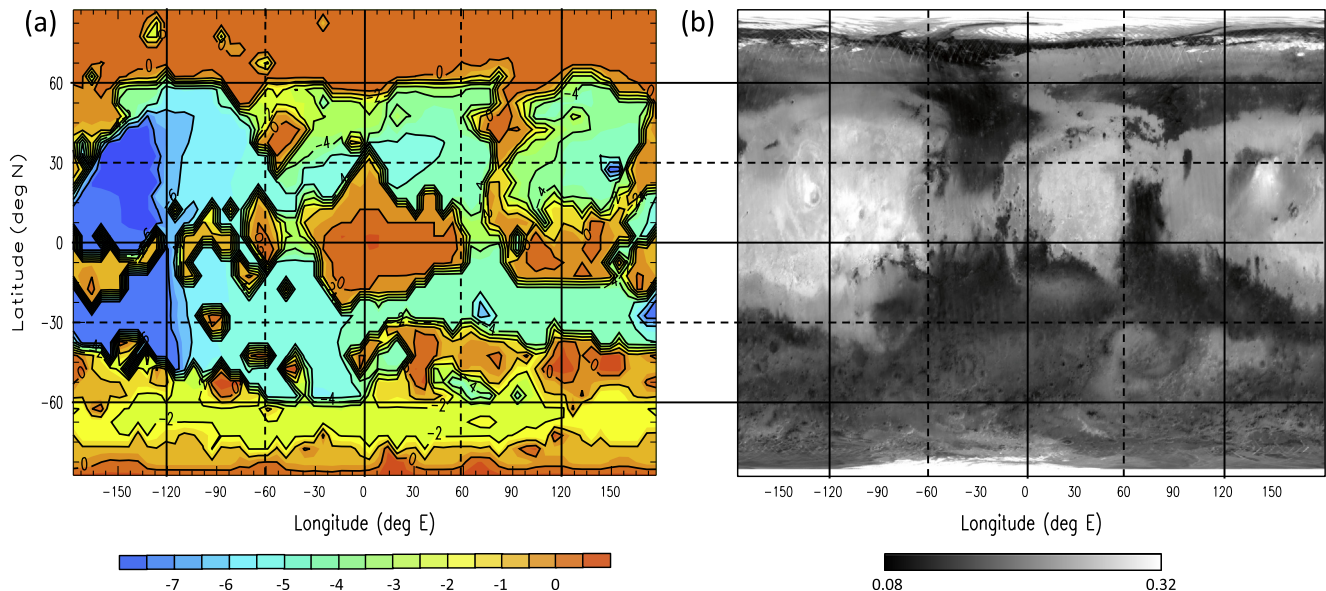


Fig. 30. (a) \log_{10} of the surface dust cover in kg m^{-2} , averaged over years 21–30 of simulation FINDUST Stage O, and (b) the surface albedo averaged over all MGS TES mapping years from the AGU TES website (Christensen et al., 2001). Grid lines have been added to aid comparison between the two plots.

2001). While albedo cannot be mapped to dust thickness, and the same high albedo might be produced by a mm or tens of m of dust, low albedo likely means very little dust. We therefore compare low albedo regions with regions simulated to have low dust cover, and find a reasonable match in the southern hemisphere. Simulated low dust regions largely coincide with a wide collar of low albedo that shifts to higher southern latitudes in the western hemisphere, and extends into the northern hemisphere over Syrtis ($\sim 60\text{--}80^\circ\text{E}$) and to a lesser extent between Arabia and Tharsis ($\sim 0\text{--}60^\circ\text{W}$).

Other than Syrtis, however, there is little agreement in the northern hemisphere between low albedo and low dust regions. The major low albedo regions are located at the northern extent of the WBC meridional corridors: in Acidalia, Utopia, and to a lesser extent Arcadia, suggesting that surface dust is lost here via wind stress lifting associated with the strong WBC flows. However, these regions are simulated to have moderate-to-high dust cover, indicating net dust gain rather than loss. This is odd, given that the simulation produces rather realistic flushing/cross-equatorial storms that evolve through these very corridors. A possible explanation is that both the observed and simulated storms draw most of their source dust from high latitudes (originating as northern frontal storms), but the simulated storms re-deposit more of this dust as they pass down the meridional corridors because the particle size (4 μm diameter) and hence sedimentation rate is larger in the model than in reality. The simulated low dust regions often coincide with regions observed to have high albedos, in particular Tharsis, northern Elysium, and NE Arabia, and a simulated ‘dust continent’ centered at $\sim 10^\circ\text{E}$, 0°N lies $\sim 30^\circ$ to the SW of the Arabia ‘high albedo continent’ observed. While high albedo does not necessarily equate to large amounts of mobile dust (see Section 4.6 iii), some of the regions simulated to have low dust cover have been inferred from observations to have meters to tens of meters of dust (e.g. in NE Arabia, Fassett and Head, 2007; Mangold et al., 2009).

Net dust loss occurs in similar northern regions in INFDUST too (Fig. 4b). We have investigated the cause of the net dust loss over one region – Tharsis – in both our infinite and finite dust runs. As in the infinite dust results of K06, gradual dust loss over Tharsis in INFDUST is dominated by dust devil lifting, except for small regions on the northern flanks of Alba Patera where wind stress lifting dominates and much faster loss occurs. In years 21–30 of

FINDUST Stage O, however, both wind stress and dust devil lifting are important, due to the lower wind stress threshold used. E.g., over central Tharsis – as shown in Fig. 31 – wind stress lifting is responsible for more than a third of the dust removed. Thus wind stress lifting is more responsible for dust removal over Tharsis in FINDUST Stage O than in INFDUST, but in either case there is net dust loss.

4.6. Implications of the surface dust distribution predicted by simulation FINDUST

As discussed in Section 4.5, the quasi-steady state surface dust distribution in Stage O of FINDUST appears to have several differences to the mean distribution inferred on Mars, in particular predicting low dust cover over much of the northern high albedo/low DCI/low thermal inertia ‘continents.’ We have identified four possible explanations:

(i) GCM deficiencies:

The GCM may incorrectly redistribute surface dust over time, due to errors in the predicted patterns of lifting and/or transport. Such errors are likely, given the many assumptions and simplifications inherent in any Mars GCM. The dust lifting schemes used here are very simple, e.g. in reality τ_t may vary spatially and temporally, depending on factors such as particle size distribution, surface roughness, and dust cover thickness (e.g. Gillies et al., 2010). Section 5 explores the potential impact of the latter on threshold. Other potential error sources include using MarsWRF’s built-in advection scheme, which may be less accurate than more advanced methods (e.g. Lian et al., 2012), and advecting only a single particle size, meaning that the evolution of size distribution and its radiative impact are not captured (Murphy et al., 1995; Wolff and Clancy, 2003; K08). Scavenging by ice is not included, nor is a detailed representation of vertical transport and mixing of dust in the PBL by strong organized updrafts, suggested by the presence of high-altitude dust maxima even outside of storms (Heavens et al., 2011). Significant errors may exist due to the lack of water ice microphysics. Ice clouds impact the circulation via radiative heating and cooling of the atmosphere (Wilson et al., 2008), and likely have their most significant impact on traveling

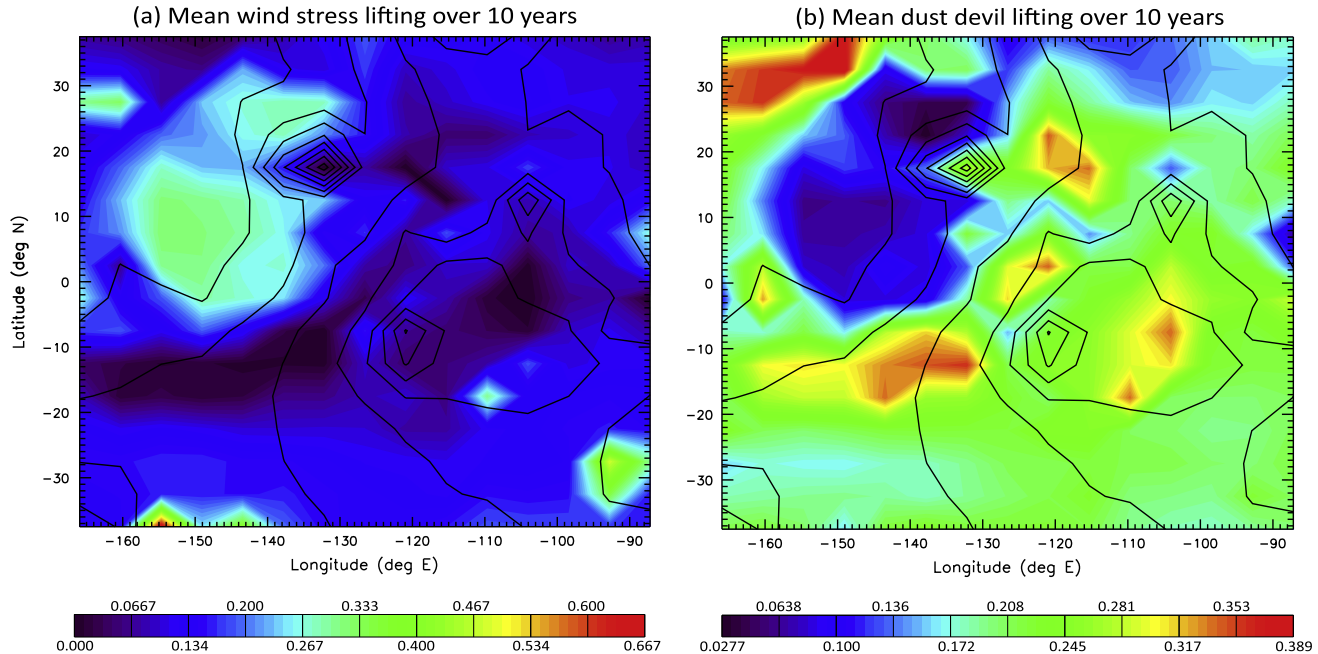


Fig. 31. Mean (a) wind stress and (b) dust devil lifting (in $10^{-3} \text{ kg m}^{-2}$ per 10 sols), averaged over years 21–30 of Stage O of simulation FINDUST. The general anti-correlation between wind stress and dust devil lifting is due to the negative feedback between dust loading and dust devil lifting described in Section 2.2.1.

waves, which are significant for dust lifting (Wilson, 2011; Kahre et al., 2012). Other factors include the radiative transfer scheme, placement of vertical layers, and relatively low horizontal resolution used ($\sim 5^{\circ}$). The latter gives ~ 300 km grid spacing at the equator: far larger than an initial storm cloud, and orders of magnitude larger than individual lifting events. This has implications for capturing both the development of dust storms and the circulations that may be key to replenishing the dust source regions. For example, M13 find that simulated north–south ‘flushing’ storms occur more frequently at higher resolution, while Toigo et al. (2012) find that predicted global wind stress lifting increases with resolution for moderate thresholds and above.

(ii) The iterative approach:

There are two primary – and related – concerns with the approach used in this work. Firstly, the pattern of dust lifting in the early Stages of a simulation will be different to that later on, since the surface initially has dust available everywhere. This means that the early atmospheric dust distribution, and hence the early pattern of dust transport, deposition and hence overall dust rearrangement, will also differ. This may send the simulation down the wrong initial path and impact the final surface dust distribution produced. An alternative would be to impose a plausible mean surface dust distribution, and iterate from there. However, there are major difficulties with such an approach (see Section 4.1 and (iv) below), putting it beyond the scope of the current work. Secondly, the early atmospheric circulation – which is forced by the atmospheric dust distribution in ‘active’ dust simulations – will also be different to that later on. This will further adversely impact the pattern of dust lifting, transport and deposition, and hence surface dust rearrangement. In an attempt to mitigate this we explored using ‘passive’ dust simulations to reach steady state. In this case the atmospheric dust distribution seen by MarsWRF’s radiative transfer scheme is prescribed based on observations, with the distribution produced by lifting, transport and deposition being held separately. Surface dust rearranges itself as described above until a steady state distribution is reached, at

which point active dust is turned on. The advantage is that the circulation even early on is forced by more realistic atmospheric dust distributions, thus is more realistic overall. We did not pursue this approach because the passive dust simulations lacked local or larger-scale positive feedbacks on wind stress lifting, hence the patterns of dust lifting, transport and deposition, and thus surface dust rearrangement, were very different to those in simulations with active dust. This resulted in the surface dust patterns changing rapidly after active dust was switched on. However, the mean distribution produced by a long passive simulation – while not fully realistic – may provide a better starting point for a multi-Stage active simulation than the uniform initial dust cover used here, and such a ‘hybrid’ approach will be explored in future work.

(iii) Ancient deep surface dust deposits:

If the northern high albedo ‘continents’ do have thick dust deposits, MarsWRF’s prediction of net dust loss here could still be correct, provided that the deposits formed during past climate epochs when dust accumulated here instead. Mars undergoes climate cycles which vary the pattern of dust lifting, transport and deposition over periods ranging from 50 kyr to several Myr (Laskar et al., 2002, 2004). Potentially, the changes to the circulation could be such that large dust deposits accumulate during one climate epoch in regions with net dust loss in another, with the current surface dust distribution reflecting this history. If so, then to correctly model the dust cycle we would need to impose such deep surface dust reservoirs in these regions that lifting continues here throughout a simulation, despite the high net loss rates. However, doing so would be contradictory to our goal of finding a self-consistent steady state surface dust distribution for present day Mars. It would also conflict with measurements of radioactive decay products by APXS on the Spirit rover, which indicate that most dust lifted into the atmosphere is not ‘fresh’ dust from a deep reservoir but rather dust previously lifted some time in the past few decades (Melin et al., 2014). This suggests that –

even if ancient deep dust deposits exist on Mars – significant dust lifting cannot be occurring over them.

(iv) High albedo/low thermal inertia regions do not have deep deposits of mobile dust:

Some observations imply deep dust deposits in Arabia and parts of Tharsis (e.g., Fassett and Head, 2007; Mangold et al., 2009; Keszthelyi et al., 2008). E.g., imaging suggests that much of Tharsis is covered with a mantle at least 4 m deep (Keszthelyi et al., 2008). However, imaging of Tharsis aeolian features linked to saltation indicates particle sizes far larger than those of mobile dust, and suggests the presence of dust aggregates instead, which may indurate to become duststone over time and would be consistent with the low thermal inertia observed (Bridges et al., 2010). The significance of this is that high albedo/low thermal inertia surfaces do not always equate to large amounts of mobile dust, and could be composed of duststone or dust aggregates that are too large to be suspended and thus do not participate in the dust cycle or storms. This could potentially explain why some of the northern hemisphere high albedo regions have low predicted dust cover in FINDUST. However, it cannot explain regions with low albedo and high predicted dust.

Without knowing which of these explanations is correct it is difficult to assess the impact on the realism of our results. If Tharsis is not a major source of dust on Mars itself, either because lifting is far weaker than predicted (option i) or because its high albedos are produced by something other than mobile dust (option iv), then FINDUST Stage O correctly predicts little lifting here. I.e., the lack of surface dust here by Stage O actually compensates for these errors. On the other hand, if Tharsis is a major source region on present day Mars, and either the GCM is failing to replenish dust here quickly enough (option i and/or ii) or this region has large ancient dust deposits (option iii), then the dust cycles and storms in FINDUST Stage O will be flawed. Our results make clear the potential for time-evolving, exhaustible surface dust to have a significant impact on dust storm onset, growth and decay, and on interannual variability in major storm type, but such open questions and apparent mismatches to Mars itself compromise the utility of MarsWRF results as a proxy for the real dust cycle. In future work we will explore the impact of more realistic dust lifting, size distributions, and PBL processes on our results. We will also examine how our finite dust simulations change when we run MarsWRF for other orbital settings (e.g., higher obliquity or perihelion during northern summer).

4.7. Could the surface dust distribution be used to make dust storm predictions?

Availability of surface dust at a grid point is a necessary (if not sufficient) condition for lifting to occur there. In Section 4.4 we demonstrated that simulated storms of a particular type often have similar patterns of primary source grid points for their onset and/or growth phase. This suggests that adequate surface dust availability over a *particular set of points* may be a necessary (but not sufficient) condition for a *particular storm type* to occur. The ability to identify such sets of points would have great predictive power. Unfortunately, no two storms have identical lifting patterns during their onset, let alone growth, phase. In INFIDUST a few grid points contribute nearly all of the dust for major storms (Section 3.3.2), but in FINDUST (and most likely in reality) even the top ranked points contribute at most a few percent of the total dust content of major storms (Section 4.4.2). This makes it difficult to attribute the absence (or weakness) of a particular storm type in a given year to the lack of dust over a particular set of points at the start of the storm season.

The fundamental question is whether surface dust availability patterns could be used to provide predictive skill, in a GCM or potentially on Mars itself. More statistics would certainly help. Using a GCM, we could assemble a database containing the immediately pre-storm surface dust cover and top ranked source points for a large number of examples of a particular storm type, and look for statistical correlations to identify necessary conditions for that storm type to occur. This would not be sufficient to guarantee that it *would* occur, but should allow the prediction (with a certain degree of confidence) that it *would not* occur, given the surface dust distribution at a certain time of year. While surface dust availability may be a necessary condition for some storms to occur, the dynamical state of the atmosphere likely has the final word. Thus any database analysis used for storm prediction should include the atmospheric component as well, focusing on statistical correlations between storm types and aspects of the circulation that impact surface wind patterns (e.g., Hadley cell width; strength of different waves modes). Such relationships have already been investigated in relation to e.g. the growth of regional storms in Isidis and Chryse (Wang et al., 2003; Newman et al., 2004). The dynamical analysis required would be the same as in an infinite surface dust simulation, although the added dependence on surface dust availability (both directly and via the many couplings between dust cover and atmospheric state) would complicate the interpretation of results. In Sections 4.4.3 and 4.4.4 we examined a far smaller database than proposed here, and found that simulated early major storms appeared to be influenced by availability of surface dust in key source regions for both onset and growth. Conversely, simulated late storms appeared to be more dependent on interannual variability of peak wind stresses in a key onset region (SE of Isidis), rather than being limited by availability of surface dust.

What about Mars itself? Could we develop an ability to determine which types of storms are likely or unlikely to occur, based on e.g. the observed albedo map prior to the storm season? A major additional difficulty would be that the number of years of data are currently inadequate to produce an observationally-based dataset as large as that described for the GCM. However, the possibility of being able to predict that e.g. no storm will occur before a certain L_s (or occur at all) is very appealing. Szwast et al. (2006) already suggest one region (Daedalia) in which surface dust availability may be critical for the growth of certain storms (see Section 1.2.2). Hence it would be of great interest to demonstrate such predictive skill in a GCM simulation of Mars dust storms, although – as no GCM provides a perfect representation of the system – it would largely indicate the *potential* for storm predictability, rather than having immediate applicability to real Mars.

5. Dust cycle simulations with finite surface dust and a variable stress threshold

Using finite surface dust and a constant wind stress threshold, we are unable to find a self-consistent, steady state solution with continuing major storms. This may indicate that a self-consistent solution does not exist for present day Mars, and that major storms continue to occur only because of deep dust deposits formed over a past climate epoch (see Section 4.6 iii), as suggested by K05. Alternatively, a solution may exist, but we may have failed to locate it because of either deficiencies in our approach or the lack (or incorrect formulation) of key physical processes in MarsWRF. In this section, we investigate the latter possibility, specifically the formulation of the threshold wind stress, which was assumed to be constant in all MarsWRF simulations described above.

Pankine and Ingersoll (2002, 2004) argue that it is suspicious for the martian dust cycle to be so finely tuned, with wind stress

thresholds such that the system has strong interannual variability. They suggest it may be an example of self-organized criticality, in which some negative feedback brings the system to such a state, and would do so even at high obliquities when peak winds are expected to be stronger. They propose a negative feedback in the form of τ_t increasing as dust is removed from the surface, making it more difficult to remove further dust. Such a feedback may be justified in two ways. First, as dust is removed the remaining dust will be lower relative to any non-erodible elements present, making it harder to access (a ‘sheltering’ effect). Though the overall wind stress increases with roughness, the fraction that acts on erodible elements decreases (Greeley and Iversen, 1985). Second, as the surface dust level drops, remaining particles lie lower in the PBL, thus experience slightly lower wind stresses. Both effects result in decreased wind stresses on less dust cover, and can be represented as an increase in threshold there.

5.1. A long-term steady state using variable thresholds: simulation FINDUST_VAR

We have tested such a negative feedback in MarsWRF. We find it possible to reach a long-term steady state surface dust distribution using a formulation in which τ^t varies about its initial value, τ_{init}^t , with a cubic dependence on the fractional change in surface dust relative to its initial value, such that higher dust cover results in lower thresholds and vice versa. We also imposed a lower limit on τ^t to prevent it falling to zero for high dust cover, such that the lowest τ^t possible was 1/8th of τ_{init}^t . The threshold is given by:

$$\tau^t = \min[\tau_{init}^t/8, \tau_{init}^t(1 + [\Psi_{init} - \Psi]/\Psi_{init})^3] \quad (6a)$$

or equivalently:

$$\tau^t = \tau_{init}^t/8 \quad \text{if } \Psi \geq (1 - [(1/8)^{1/3} - 1])\Psi_{init}; \quad \text{i.e., if } \Psi \geq 1.5\Psi_{init} \quad (6b)$$

$$\tau^t = \tau_{init}^t(1 + [\Psi_{init} - \Psi]/\Psi_{init})^3 \quad \text{if } \Psi \\ < (1 - [(1/8)^{1/3} - 1])\Psi_{init}; \quad \text{i.e., if } \Psi < 1.5\Psi_{init} \quad (6c)$$

where Ψ is the surface dust cover (in kg m^{-2}) and Ψ_{init} is its initial, globally-uniform value (2 kg m^{-2} in our simulations). The maximum threshold possible is $8 \times \tau_{init}^t$, achieved when the surface dust cover reaches zero (though in practice this limit is never reached due to the increasing difficulty of lifting dust as it is approached). The minimum threshold of $\tau_{init}^t/8$ is used for all surface dust cover values that exceed Ψ_{init} by 50% or more.

Fig. 32 shows the variation of surface dust at the top three dust contributors over the last 46 years of FINDUST_VAR. This simulation has a variable threshold as shown in Eq. (6), with $\tau_{init}^t = 0.026 \text{ Pa}$. It ran for 147 years over 4 Stages (using the re-tuning method described in Section 4.1) until a steady state with continuing major storms was achieved in Stage D, then run for the additional 46 years shown. Although dust cover varies greatly from year to year, the long-term mean (over several Mars years) stays constant with no persistent trend, unlike some of the top contributors in FINDUST Stage O. By Stage D of FINDUST_VAR, the threshold feedback slows the depletion rate of the primary source regions as their surface dust cover drops, allowing them enough time to be replenished before depletion begins again, even with continuing major dust storms.

Fig. 33 shows global T15 values for the same 46 years. In this particular simulation, global storms occur less frequently than in FINDUST and than on Mars, with one every 5 years or so on average, rather than roughly every 3. However, this varies with the

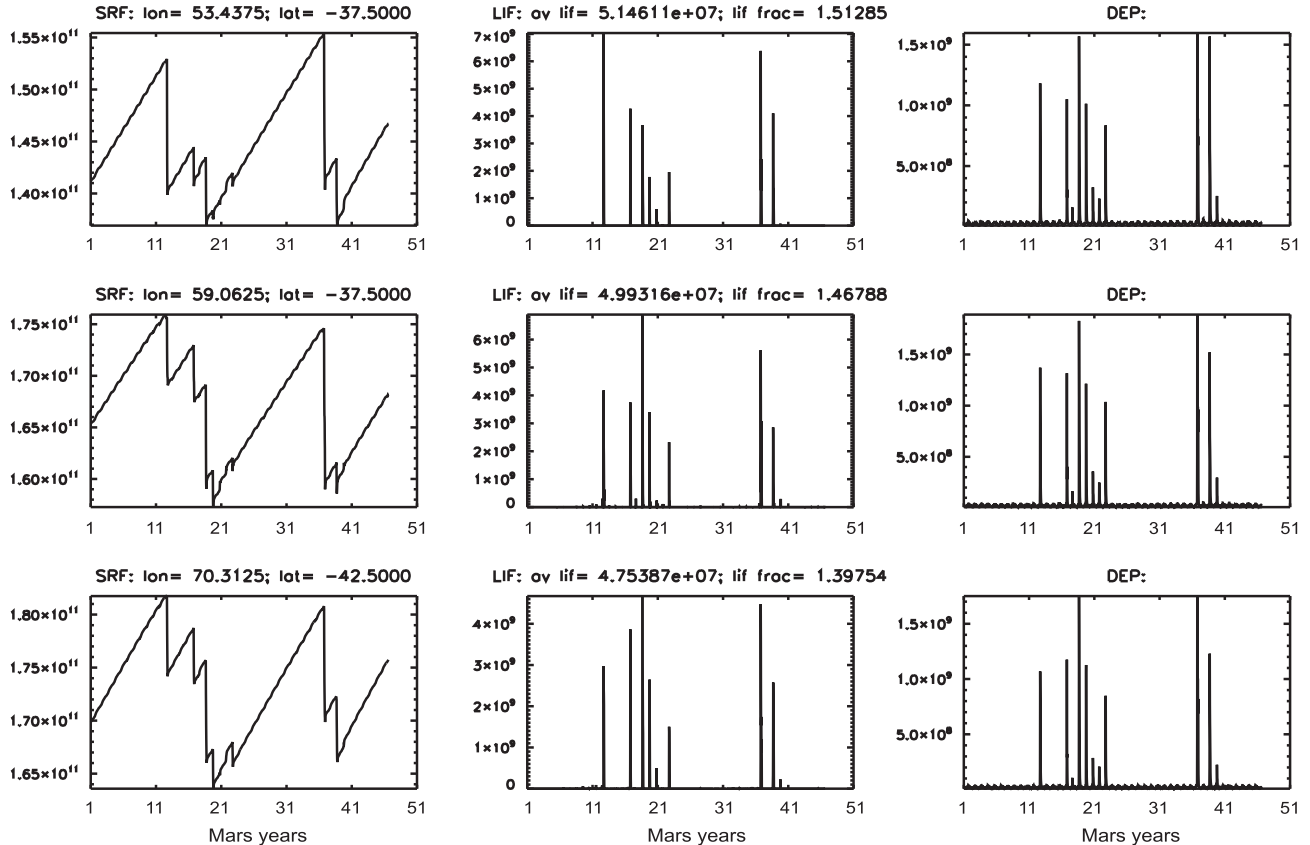


Fig. 32. As Fig. 6, but now for the final 46 years of FINDUST_VAR Stage D, at the 1st (top row), 2nd (middle row) and 3rd (bottom row) ranked grid points in terms of total dust contributed over all years shown. All dust lifting parameters were held constant for the whole of Stage D (including the period shown).

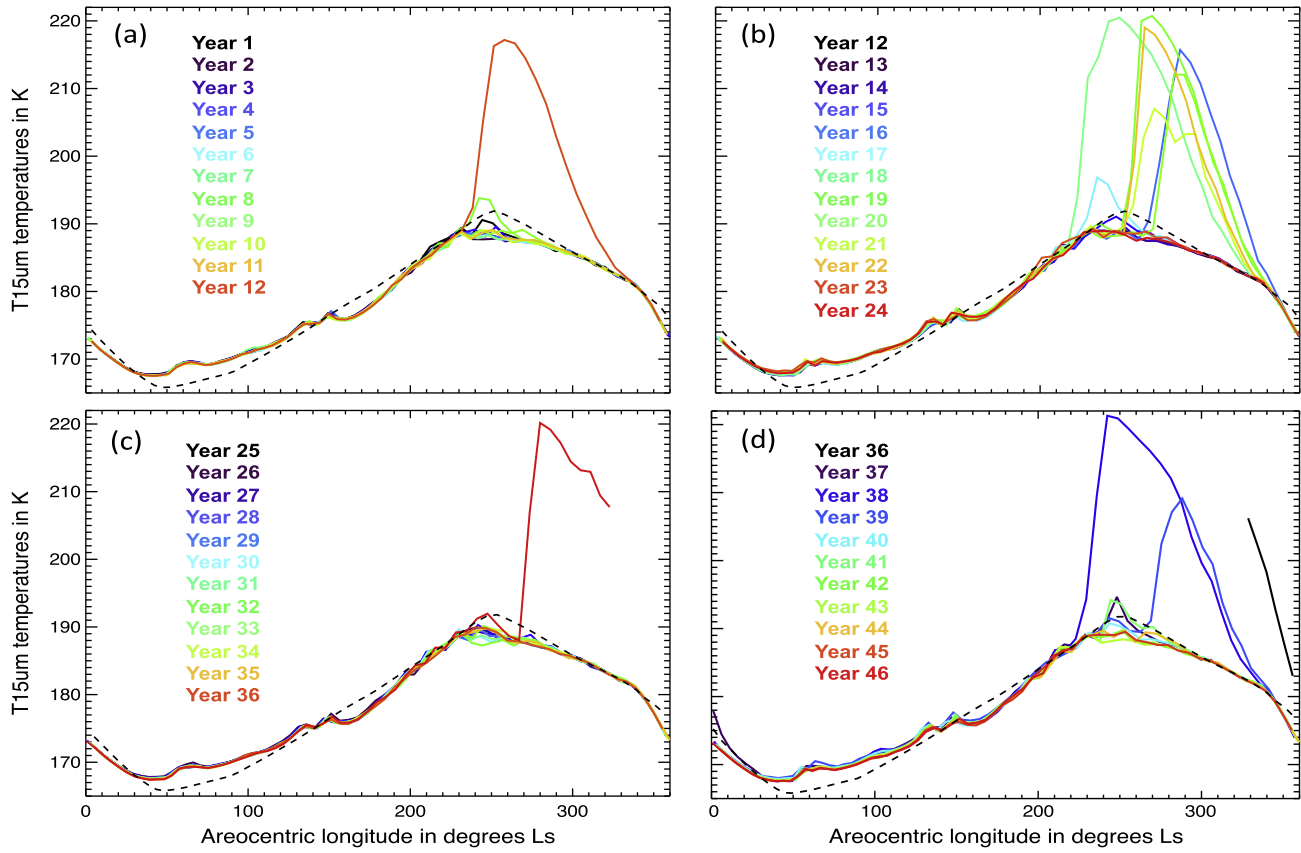


Fig. 33. T15 curves as in Fig. 2, but for the same 46 years of FINDUST_VAR Stage D as in Fig. 32.

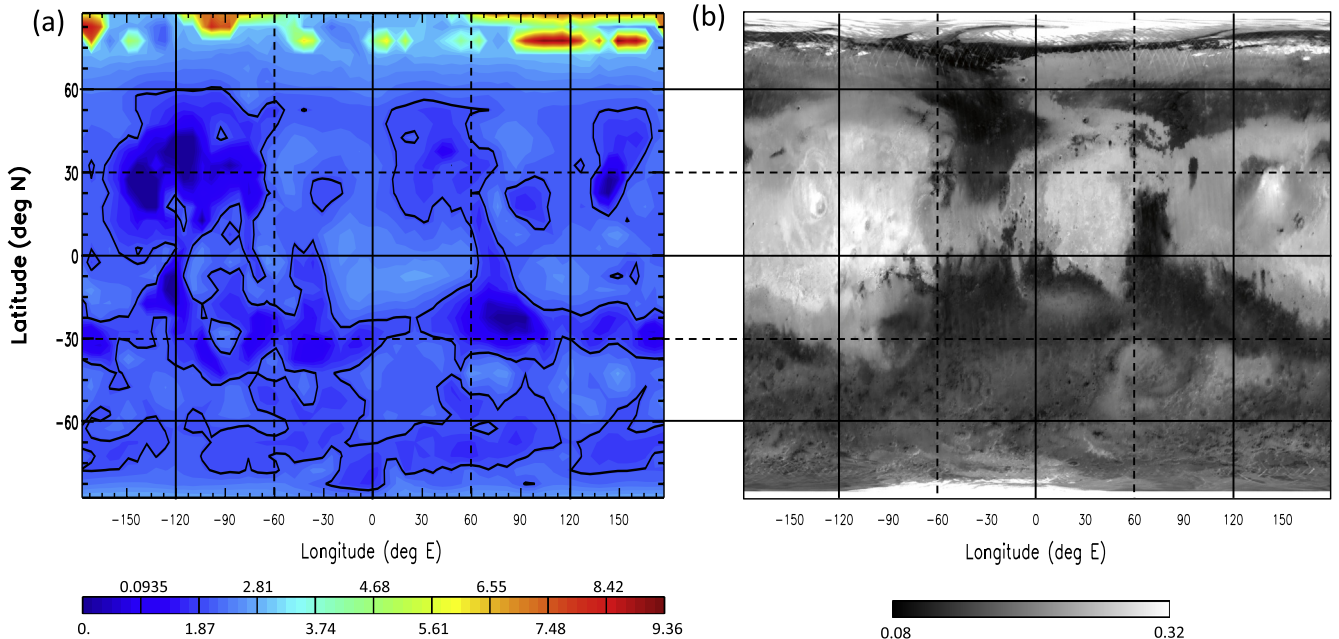


Fig. 34. As Fig. 30 but averaged over the final 46 years of FINDUST_VAR Stage D. Note that unlike Fig. 30 a linear scale is used for plot (a), showing the long-term mean surface dust in kg m^{-2} .

choice of dust lifting parameters and with the exact formulation of the threshold variation used (Eq. (6)), and tuning it to better match observations is left to a follow-up paper. As in the constant

threshold results, FINDUST_VAR does not produce any major storms as early as some are observed ($L_s \sim 184^\circ$), with the earliest at $L_s \sim 216^\circ$ in the 18th year shown. However, it does produce a

range of onset times and locations, both regional and global storms, and significant interannual variability in storm occurrence, type and size.

[Fig. 34](#) shows the long-term mean dust cover by FINDUST_VAR Stage D. As in FINDUST Stage O there is relatively low dust cover predicted over many northern high albedo regions. However, the negative feedback on dust depletion (due to the variable threshold scheme) results in fewer regions losing significant dust. As in FINDUST there is a build-up of dust to the SW of the observed high albedo ‘continent’ in Arabia, and depletion of dust over Tharsis. Unlike FINDUST, however, there is better agreement between predicted dust build-up and high albedos in the general Elysium region, east of Syrtis in the northern hemisphere (except over Elysium Mons itself). Also, the predicted dust depletion in Tharsis peaks over Alba Patera and Olympus Mons, with significant dust retained long-term over much of Tharsis in steady state (albeit less than it began with, since most of the region is inside the solid black contour denoting zero change).

5.2. Significance of simulation FINDUST_VAR

While there is physical justification for the variable threshold feedback mechanism, the exact form used here was not based on theory or laboratory/field measurements. Rather, it was designed to introduce enough ‘sluggishness’ into the system – i.e., to slow the removal rate sufficiently – that a balance could be produced between dust lifting and deposition once the GCM reached steady state, even in the key source regions for major dust storms. Despite these caveats, FINDUST_VAR does produce a truly self-consistent steady state with continuing major storms without requiring either an artificial resupply mechanism or an artificial dust lifting shut-off when some peak opacity is reached.

M13 also appear to produce a steady state surface dust distribution in their GCM by including a variable threshold feedback mechanism, with major storms continuing to occur about every 3 years. In their formulation, τ_t increases linearly with the decrease in surface dust cover, and never drops below its original value of 0.02 Pa (i.e., does not decrease if the surface dust cover increases above its initial value). However, their steady state solution is primarily maintained by the inclusion of a globally-uniform, continuous decrease in τ_t , the magnitude of which is tuned to produce the observed rate of storms. In their simulations, this term dominates over the variable threshold effect, is the primary control on the frequency of global storms, and is equivalent to artificially resupplying surface grid points at a global rate of 4.75 $\mu\text{m}/\text{year}$. M13 describe this resupply term as compensating for apparent GCM biases that result in more net south-to-north transport than on Mars itself, with dust devils and non-dust storm wind stress lifting unable to replace the dust lost during major storms. They justify it physically as (a) representing the small-scale re-distribution of dust within a GCM grid box, effectively the ‘freeing up’ of dust previously unavailable for lifting, and/or (b) representing the production of dust aggregates, which may be needed before dust lifting can occur in saltation-limited areas. However, it is unclear that such processes would be globally uniform, or how they could operate on such short timescales that they would dominate the variability of storms produced. As previously noted, M13 do not re-tune their lifting rate parameters as dust is initially rearranged and high stress source regions exhausted. We suggest this explains why their simulations are so far from being balanced, and why such a large artificial resupply term is required. By contrast, we argue that such re-tuning is fundamental (see Section 1.2.3) and apply it in our constant and variable threshold simulations, although far less time (4 stages and 147 years) is required to reach steady state in the latter case (FINDUST_VAR). In addition, M13 shut off lifting when column visible opacities exceed 10, rather

than allowing the GCM to self-consistently shut down lifting on its own.

WK09 also include a variable threshold scheme in which τ_t is a function of the surface dust depth, varying about a nominal value of 0.028 Pa. Like M13, WK09 also require an artificial dust resupply term to achieve a long-term steady state with continuing major storms. However, in this case the resupply term is only 0.2 $\mu\text{m}/\text{year}$ and is only triggered when the local surface dust falls below the initial value, thus is at least ~ 24 times smaller than that required by M13. For this reason the variable threshold feedback dominates in WK09’s simulations, unlike those of M13. However, WK09 note that the chosen resupply rate still impacts their results, playing a significant role in resupplying source regions in years without major storms, and influencing the frequency of storm activity in their simulations. WK09 describe this replenishment as compensating for the gradual export of dust to the (particularly north) polar regions, where some dust falling on CO_2 ice-covered surfaces is not released again, and gradually accumulates over time. We predict some dust accumulation at northern high latitudes in FINDUST_VAR (see [Fig. 34](#)), but not enough to impact the size of dust storms over time, at least on timescales of about a century. Our simulations conserve total dust mass very well, thus the rate of northern polar dust accumulation appears to be far less than in WK09. They note that their simulations lack regional dust storms with moderate opacities and higher, thus one possibility is that the larger number of regional scale storms in our simulations are able to redistribute northern high latitude dust more effectively. Like M13, WK09 also shut off lifting when column visible opacities exceed some threshold (in this case, an opacity of 5), rather than allowing the model to self-consistently shut down lifting.

Given that FINDUST_VAR appears to produce the most self-consistent steady state dust cycle to date, it is worthy of further investigation. We will examine the behavior of the dust cycle and surface dust rearrangement in more detail in a follow-up paper, and consider the impact of using other forms of the variable threshold parameterization.

6. Summary and conclusions

We have investigated the impact of finite surface dust cover on the martian dust cycle simulated by the MarsWRF GCM, running with radiatively active dust, parameterized dust lifting, and spontaneous dust storms. Specifically, we have tested the hypothesis that a self-consistent, long term steady state surface dust distribution that supports realistic dust cycles exists for present day Mars, and have explored the impact of a quasi-steady state surface dust distribution on dust cycles, storms, and their interannual variability.

As a ‘baseline’ we first ran MarsWRF with infinite surface dust availability, with wind stress lifting set proportional to the predicted saltation flux for stresses above a constant threshold wind stress, τ_t , and with dust devil lifting set proportional to the predicted ‘dust devil activity’ (after [Renno et al., 1998](#)). We ran multiple simulations at different τ_t values, seeking the ‘best fit’ dust lifting parameters (i.e., those giving the dust cycle closest to that observed). We find that MarsWRF results are ‘in family’ with similar work by B04,06, in that relatively high thresholds (~ 0.046 – 0.049 Pa) are required to produce significant interannual variability when the dust supply is unlimited. By contrast, the results of N02a,b and K05 lacked respectively global storms or significant variability, despite including similar dust processes and exploring similar parameter space. The increased variability for high thresholds occurs because the high wind stresses required to overcome them are relatively rare, which introduces more chaotic behavior

into the system, an effect magnified by strong positive feedbacks on wind stress lifting once it begins. Our most realistic simulation, INFIDUST, produces realistically intermittent global storms for $\tau_t = 0.047$ Pa, but as with B04,06 does not capture early storm onset or the full range of storm types observed, and has unrealistically slow storm decay.

The remainder of our simulations used finite surface dust. A complication is that the best fit dust lifting parameters differ depending on the distribution of surface dust. We therefore used MarsWRF to evolve an initially globally uniform surface dust distribution in Stages, updating the dust lifting parameters before each new Stage to provide a new best fit to the observed dust cycle even as more surface grid points became exhausted of dust. The idea was to iterate toward (i) the set of dust lifting parameters and (ii) the long term steady state surface dust distribution that together best captured the present day dust cycle on Mars. K05 and M13 also looked at allowing dust cycles to rearrange an initially uniform surface dust distribution. However, K05 only re-tuned their lifting parameters once as regions were exhausted (equivalent to 2 Stages), and M13 did not re-tune theirs at all before moving on to alternative solutions. We argue that many re-tuning Stages may be required for the surface dust distribution to settle itself into a steady state, in which the remaining source regions receive as much dust long-term as they lose.

We focused on one finite dust simulation, FINDUST, which ran for 374 years over 17 Stages with $\tau_t = 0.02$ Pa. The latter is less than half the threshold used in INFIDUST, thus is exceeded far more often over far more of the surface, spreading wind stress lifting sites more evenly across the surface. Since surface dust replenishment (via deposition) is rather uniform and widespread, this improves the likelihood of a balance being found between dust replenishment and removal (via lifting) on decadal timescales. However, a long term steady state surface dust distribution with continuing major storms still could not be found. Possible explanations include GCM deficiencies (with e.g. the dust lifting parameterizations), problems with the iterative method for seeking a steady state, or the need to include potential ancient deep dust deposits as an effectively infinite dust source.

Despite this, we were able to identify and explore a quasi-steady state period in FINDUST. By its 15th Stage (Stage O), many source grid points had been permanently exhausted of dust, with the remainder exhibiting such slow depletion in mean dust cover that realistic dust cycles and storms continued for the next ~60 years. We therefore treated Stage O years 21–30 as a proxy for a true steady state solution, and used these results to study the impact of finite surface dust on dust cycles and storms. The range of simulated storm onset locations and times, the correlation between simulated and observed storm types, and the amount of interannual variability in FINDUST Stage O are all greatly enhanced compared to our infinite dust results. Years 21–30 capture seven distinct regional storm types with many similarities to observed families of storms, such as northern frontal (sometimes ‘flushing’) storms, as well as an observed gap in regional storms at $L_s \sim 250\text{--}305^\circ$ and a gap in all storms at $L_s \sim 40\text{--}135^\circ$. Hellas regional storms simulated around spring equinox ($L_s \sim 180^\circ$) have similar patterns to some observed, though unlike those observed, none of the simulated storms expand to become global. The lack of very early major storms may be due to the absence or poor representation of a process in the GCM that produces strong wind stresses earlier in the storm season, such as mesoscale circulations (requiring higher horizontal resolution) or radiatively active water ice clouds.

Years 21–30 also contain five major (global or large regional) storms: three ‘early’ storms (onset between $L_s \sim 210^\circ$ and 220°) and two ‘late’ storms (onset at $L_s \sim 252^\circ$). All three early storms develop from combined regional storms (Acidalia–Chryse ‘flushing’ and Noachis/Hellas storms in years 24 and 25; Noachis/Hellas and

southern cap edge/Hellas storms in year 30), with subsequent lifting mostly at southern mid-latitudes and in Isisid/Tyrrhenium or Chryse. Onset of the year 24 and 25 storms is very similar to the MY 1, 9 and 28 storms on Mars, though the latter all occurred at least $30^\circ L_s$ later in the year. Both late storms are global and begin in Isisid/Tyrrhenia/Hesperia at $L_s \sim 252^\circ$ in years 23 and 29, in a period modeled and observed to have only global events. However, while some onset activity is observed here, Noachis/Hellas typically dominates the observed onset of major storms at this time of year, with the western hemisphere dominating later in the storm season, suggesting a possible bias in where the simulation predicts lifting should peak (or dust be exhausted from). Further growth of the simulated late storms involves more high southern latitude lifting than the early storms, due to the poleward movement of the south polar cap edge, producing stronger cap-edge winds at higher latitudes and permitting previously ice-covered dust to be removed there.

Interannual variability is greatly increased in the later Stages of FINDUST, compared to any infinite dust run. The two mechanisms behind this relate to either permanent or temporary exhaustion of source grid points. By FINDUST Stage O, regions that regularly experience high wind stresses have been *permanently* exhausted of dust, and the new primary source regions are those at which τ_t is exceeded only occasionally. This produces enhanced sensitivity to intrinsic atmospheric variability in the primary source regions, just as occurs at very high τ_t for the high wind stress primary source regions when using infinite surface dust. The second mechanism for interannual variability involves the *temporary* exhaustion of a source region, and its replenishment timescale, which produces year-to-year differences in dust availability at a surface grid point at a certain L_s . Hence dust cycle interannual variability is due to atmospheric variability via the first mechanism, and year-to-year differences in surface dust availability via the second. In years 21–30, the occurrence (or at least size) of early major storms appears to be largely controlled by the second mechanism. Fallout from a major late storm appears necessary (though not sufficient) for both onset and growth of early major storms, in order to replenish key source regions in Noachis–Hellas and Chryse or Isisid. This replenishment is weaker during fallout of early storms than late storms, due to differences in the circulation, source regions, and/or storm intensity. By contrast, the occurrence of late major storms appears to be largely unrelated to surface dust availability in either onset or growth source regions, with atmospheric variability dominating instead. Both late storms have nearly identical onset patterns, with very effective subsequent replenishment of dust in their primary onset region (SE of Isisid). Yet despite this, no smaller storms ever occur here in other years at the time when the late major storms begin. This suggests that late storm occurrence is linked to atmospheric variability to the SE of Isisid, resulting in unusually strong wind stresses there in some years, rather than being directly linked to surface dust availability there. Once sufficient initial lifting in this key region has been triggered, a global storm is very likely to occur.

With finite dust and a constant wind stress threshold we were unable to find a true steady state in which major storms would continue for more than a few decades. We therefore explored a variable threshold parameterization, in which τ_t increases locally as surface dust is removed. This provides a negative feedback on wind stress lifting and slows the removal rate sufficiently for deposition to replenish some source regions, enabling a balanced, ‘steady state’ situation to be more easily achieved. Simulation FINDUST_VAR requires only 4 iterative Stages to locate a set of dust lifting parameters and long-term mean surface dust distribution with continuing major storms. Unlike previous studies, FINDUST_VAR achieves a true steady state without requiring an artificial resupply term or a lifting cut-off above some threshold

dust opacity. However, the form of the threshold variation is determined empirically rather than based on theory. We will explore other forms, and examine these results further, in a follow-up paper.

Both the quasi-steady state surface dust distribution in FINDUST Stage 0 and the steady state distribution in FINDUST_VAR have several differences to that observed on Mars. Much of the inferred northern hemisphere ‘dust continents’ are not predicted, with instead net dust loss and hence low dust cover over most of Tharsis and NE Arabia, though this is greatly reduced in FINDUST_VAR. While some of this may be due to erroneous mapping of high albedo, etc. to large amounts of mobile dust, this cannot explain all of the mismatches. If the lack of source dust here is unrealistic – whether due to net loss being incorrectly predicted here, or due to these being ancient deep dust deposits that continue to provide dust despite net loss – then our simulations may be compromised in terms of their relation to real Mars. However, the results of FINDUST and FINDUST_VAR demonstrate some of the mechanisms at work when surface dust availability is a factor, and show their potential for impacting dust storms and interannual variability. These results also demonstrate the risk of relying on infinite surface dust simulations to assess dust sources and sinks, or to predict dust cycles in the past.

Acknowledgments

Portions of this work were funded through NASA's Planetary Atmospheres (PATM) program, grant numbers NNG06GF27G and NN10AB42G. The simulations presented were largely performed on NASA's High End Computing Pleiades cluster at NASA Ames, and we would like to express our gratitude for the excellent resources and support provided there. We would also like to thank Francois Forget for permitting us to use his one-dimensional sedimentation scheme, and Shabari Basu and Helen Wang for their assistance with Fig. 1 and Fig. 20, respectively. Finally, many thanks go to our two reviewers, Nathan Bridges and John Wilson, for their careful and insightful reviews.

References

- Ayoub, F. et al., 2014. Threshold for sand mobility on Mars calibrated from seasonal variations of sand flux. *Nat. Geosci.* <http://dx.doi.org/10.1038/ncomms6096>.
- Basu, S., Richardson, M.I., Wilson, R.J., 2004. Simulation of the martian dust cycle with the GFDL Mars GCM. *J. Geophys. Res.* 109, E11006. <http://dx.doi.org/10.1029/2004JE002243>.
- Basu, S. et al., 2006. Simulation of spontaneous and variable global dust storms with the GFDL Mars GCM. *J. Geophys. Res.* 111, E09004. <http://dx.doi.org/10.1029/2005JE002660>.
- Bridges, N.T. et al., 2010. Aeolian bedforms, yardangs, and indurated surfaces in the Tharsis Montes as seen by the HiRISE Camera: Evidence for dust aggregates. *Icarus* 205, 165–182. <http://dx.doi.org/10.1016/j.icarus.2009.05.017>.
- Briegleb, B.P., 1992. Delta-Eddington approximation for solar radiation in the NCAR community climate model. *J. Geophys. Res.* 97, 7603–7612.
- Cantor, B.A., 2007. MOC observations of the 2001 Mars planet-encircling dust storm. *Icarus* 186, 60–96. <http://dx.doi.org/10.1016/j.icarus.2006.08.019>.
- Cantor, B.A. et al., 2001. Martian dust storms: 1999 Mars Orbiter Camera observations. *J. Geophys. Res.* 106 (E10), 23653–23687.
- Christensen, P.R., 1988. Global albedo variations on Mars: Implications for active aeolian transport, deposition, and erosion. *J. Geophys. Res.* 93 (B7), 7611–7624. <http://dx.doi.org/10.1029/JB093B07p07611>.
- Christensen, P.R. et al., 2001. Mars global surveyor thermal emission spectrometer experiment: investigation description and surface science results. *J. Geophys. Res.* 106 (E10), 23823–23871. <http://dx.doi.org/10.1029/2000JE01370>.
- Clancy, R.T. et al., 2000. An intercomparison of ground-based millimeter, MGS TES, and Viking atmospheric temperature measurements: Seasonal and interannual variability of temperatures and dust loading in the global Mars atmosphere. *J. Geophys. Res.* 105 (E4), 9553–9571. <http://dx.doi.org/10.1029/1999JE001089>.
- Colburn, D.S., Pollack, J.B., Haberle, R.M., 1989. Diurnal variations in optical depth at Mars. *Icarus* 79 (1), 159–189. [http://dx.doi.org/10.1016/0019-1035\(89\)90114-0](http://dx.doi.org/10.1016/0019-1035(89)90114-0).
- Davy, R. et al., 2009. A model of dust in the martian lower atmosphere. *J. Geophys. Res.* 114, D04108.
- Fassett, C.I., Head III, J.W., 2007. Layered mantling deposits in northeast Arabia Terra, Mars: Noachian–Hesperian sedimentation, erosion, and terrain inversion. *J. Geophys. Res.* 112, E08002. <http://dx.doi.org/10.1029/2006JE002875>.
- Fenton, L.K., Geissler, P.E., Haberle, R.M., 2007. Global warming and climate forcing by recent albedo changes on Mars. *Nature* 446 (5). <http://dx.doi.org/10.1038/nature05718>.
- Forget, F. et al., 1999. Improved general circulation models of the martian atmosphere from the surface to above 80 km. *J. Geophys. Res.* 104, 24155–24175.
- Garvin, J.B., Frawley, J.J., Abshire, J.B., 1999. Vertical roughness of Mars from the Mars Orbiter Laser Altimeter. *Geophys. Res. Lett.* 26, 381–384.
- Geissler, P.E., 2005. Three decades of martian surface changes. *J. Geophys. Res.* 110, E02001. <http://dx.doi.org/10.1029/2004JE002345>.
- Geissler, P.E. et al., 2008. First in situ investigation of a dark wind streak on Mars. *J. Geophys. Res.* 113, E12S31. <http://dx.doi.org/10.1029/2008JE003102>.
- Gierasch, P.J., Goody, R.M., 1973. A model of a martian great dust storm. *J. Atmos. Sci.* 30, 169–179.
- Gillies, J.A. et al., 2010. Modeling aeolian sediment transport thresholds on physically rough martian surfaces: A shear stress partitioning approach. *Geomorphology* 121, 15–21. <http://dx.doi.org/10.1016/j.geomorph.2009.02.016>.
- Goldenson, N., Desch, S., Christensen, P., 2008. Non-equilibrium between dust and gas temperatures in the Mars atmosphere. *Geophys. Res. Lett.* 35 (8), L08813.
- Greeley, R., Iversen, J.D., 1985. Wind as a Geological Process: Earth, Mars, Venus, and Titan. Cambridge University Press, New York, p. 333.
- Greeley, R. et al., 1980. Threshold wind speeds for sand on Mars: wind tunnel simulations. *Geophys. Res. Lett.* 7, 121–124.
- Guo, X. et al., 2009. Fitting the Viking Lander surface pressure cycle with a Mars General Circulation Model. *J. Geophys. Res.* 114, E07006. <http://dx.doi.org/10.1029/2008JE003302>.
- Guzewich, S.D. et al., 2013a. The impact of realistic vertical dust distribution on the simulation of the martian general circulation. *J. Geophys. Res.: Planets.* <http://dx.doi.org/10.1002/jgre.20084>.
- Guzewich, S.D. et al., 2013b. High-altitude dust layers on Mars: Observations with the Thermal Emission Spectrometer. *J. Geophys. Res.* 118 (6), 1177–1194. <http://dx.doi.org/10.1002/jgre.20076>.
- Haberle, R.M., Levy, C.B., Pollack, J.B., 1982. Some effects of global dust storms on the atmospheric circulation of Mars. *Icarus* 50, 322–367.
- Heavens, N.G., Richardson, M.I., Toigo, A.D., 2008. Two aerodynamic roughness maps derived from Mars Orbiter Laser Altimeter (MOLA) data and their effects on boundary layer properties in a Mars General Circulation Model (GCM). *J. Geophys. Res.* 113, E02014. <http://dx.doi.org/10.1029/2007JE002991>.
- Heavens, N.G. et al., 2011. Vertical distribution of dust in the martian atmosphere during northern spring and summer: High-altitude tropical dust maximum at northern summer solstice. *J. Geophys. Res.* 116, E01007. <http://dx.doi.org/10.1029/2010JE003692>.
- Hong, S.-Y., Pan, H.-L., 1996. Nonlocal boundary layer vertical diffusion in a medium-range forecast model. *Mon. Weather Rev.* 124, 2322–2339.
- Hourdin, F., 1992. A new representation of the absorption by the CO₂ 15-μm band for a martian general circulation model. *J. Geophys. Res.* 97, 18319–18335.
- Jimenez, P.A., Dudhia, J., 2012. Improving the representation of resolved and unresolved topographic effects on surface wind in the WRF model. *J. Appl. Meteorol. Clim.* 51, 300–316.
- Joshi, M.M. et al., 1997. Low-level jets in the NASA Ames Mars General Circulation Model. *J. Geophys. Res.* 102 (E3), 6511–6523. <http://dx.doi.org/10.1029/96JE03765>.
- Kahre, M.A. et al., 2005. Simulating the martian dust cycle with a finite surface dust reservoir. *Geophys. Res. Lett.* 32. <http://dx.doi.org/10.1029/2005GL023495.20204>.
- Kahre, M.A., Murphy, J.R., Haberle, R.M., 2006. Modeling the martian dust cycle and surface dust reservoirs with the NASA Ames General Circulation Model. *J. Geophys. Res.* 111, E06008. <http://dx.doi.org/10.1029/2005JE002588>.
- Kahre, M.A. et al., 2008. Investigations of dust particle sizes in the martian atmosphere using the NASA Ames General Circulation Model. *Icarus* 195, 576–597. <http://dx.doi.org/10.1016/j.icarus.2008.01.023>.
- Kahre, M.A. et al., 2009. An inverse approach to modeling the dust cycle with two Mars General Circulation Models. In: Mars Dust Cycle Workshop, Mountain View, CA, pp. 125–129. <http://spacescience.arc.nasa.gov/mars-climate-modeling-group/documents/mars_dust_cycle_workshop_abstracts.pdf>.
- Kahre, M.A., Hollingsworth, J.L., Haberle, R.M., 2012. Simulating Mars' dust cycle with a Mars General Circulation Model: Effects of water ice cloud formation on dust lifting strength and seasonality. Comparative Climatology of Terrestrial Planets Meeting. LPI Contribution No. 1675, id.8062.
- Keszthelyi, L. et al., 2008. High Resolution Imaging Science Experiment (HiRISE) images of volcanic terrains from the first 6 months of the Mars Reconnaissance Orbiter primary science phase. *J. Geophys. Res.* 113, E04005. <http://dx.doi.org/10.1029/2007JE002968>.
- Kok, J.F., 2010. Difference in the Wind Speeds Required for Initiation versus Continuation of Sand Transport on Mars: Implications for Dunes and Dust Storms. *Phys. Rev. Lett.* 104, 074502. <http://dx.doi.org/10.1103/PhysRevLett.104.074502>.
- Laskar, J., Levrard, B., Mustard, J.F., 2002. Orbital forcing of the martian polar layered deposit. *Nature* 419, 375–377.
- Laskar, J. et al., 2004. Long term evolution and chaotic diffusion of the insolation quantities of Mars. *Icarus* 170, 343–364.

- Lewis, S.R. et al., 1999. A climate database for Mars. *J. Geophys. Res.* 104 (E10), 24177–24194. <http://dx.doi.org/10.1029/1999JE001024>.
- Lian, Y. et al., 2012. The Ashima/MIT Mars GCM and argon in the martian atmosphere. *Icarus* 218, 1043–1070.
- Liu, J., Richardson, M.I., Wilson, R.J., 2003. An assessment of the global, seasonal, and interannual spacecraft record of martian climate in the thermal infrared. *J. Geophys. Res.* 108 (E8), 5089. <http://dx.doi.org/10.1029/2002JE001921>.
- Mangold, N. et al., 2009. Estimate of aeolian dust thickness in Arabia Terra, Mars: Implications of a thick mantle (>20 m) for hydrogen detection. *Géomorphol.: Relief, Process., Environ.* 1, 23–32.
- Martin, T.Z., Kieffer, H., 1979. Thermal infrared properties of the martian atmosphere, 2: The 15 μm band measurements. *J. Geophys. Res.* 84, 2843–2852.
- Martin, L.J., Zurek, R.W., 1993. An analysis of the history of dust activity on Mars. *J. Geophys. Res.* 98 (E2), 3221–3246. <http://dx.doi.org/10.1029/92JE02937>.
- McKim, R., 1999. *Telescopic Martian Dust Storms: A Narrative and Catalogue, Memoirs of the British Astronomical Association*, p. 44. ISBN 0-902749-13-7.
- Meslin, P.-Y. et al., 2014. Detection of polonium-210 on Spirit dust magnets and implications for the global martian dust cycle. In: Forget, F., Millour, M. (Eds.), The Fifth International Workshop on the Mars Atmosphere: Modelling and Observation, id.3401.
- Michaels, T.I., Colaprete, A., Rafkin, S.C.R., 2006. Significant vertical water transport by mountain-induced circulations on Mars. *Geophys. Res. Lett.* 33, L16201. <http://dx.doi.org/10.1029/2006GL026562>.
- Montmessin, F. et al., 2004. Origin and role of water ice clouds in the martian water cycle as inferred from a general circulation model. *J. Geophys. Res.* 109, E10004. <http://dx.doi.org/10.1029/2004JE002284>.
- Mulholland, D.P., Read, P.L., Lewis, S.R., 2013. Simulating the interannual variability of major dust storms on Mars using variable lifting thresholds. *Icarus* 223, 344–358. <http://dx.doi.org/10.1016/j.icarus.2012.12.003>.
- Murphy, J.R. et al., 1990. Numerical simulations of the decay of martian global dust storms. *J. Geophys. Res.* 95 (B9), 14629–14648. <http://dx.doi.org/10.1029/JB095iB09p14629>.
- Murphy, J.R. et al., 1993. Martian global dust storms: Zonally symmetric numerical simulations including size-dependent particle transport. *J. Geophys. Res.* 98, 3197–3220.
- Murphy, J.R. et al., 1995. Three dimensional numerical simulation of martian global dust storms. *J. Geophys. Res.* 100, 26357–26376.
- Newman, C.E., 2001. Modelling the Dust Cycle in the Martian Atmosphere. D.Phil. Thesis, University of Oxford.
- Newman, C.E. et al., 2002a. Modeling the martian dust cycle. 1: Representations of dust transport processes. *J. Geophys. Res.: Planets* 107 (E12). <http://dx.doi.org/10.1029/2002JE001920>. Art. No. 5123.
- Newman, C.E. et al., 2002b. Modeling the martian dust cycle. 2: Multi-annual radiatively active dust transport simulations. *J. Geophys. Res.: Planets* 107 (E12). <http://dx.doi.org/10.1029/2002JE001910>. Art. No. 5124.
- Newman, C.E., Read, P.L., Lewis, S.R., 2004. Investigating atmospheric predictability on Mars using breeding vectors in a general-circulation model. *Q. J. R. Meteorol. Soc.* 130, 2971–2989. <http://dx.doi.org/10.1256/qj.03.209>.
- Pankine, A.A., Ingersoll, A.P., 2002. Interannual variability of martian global dust storms simulations with a low-order model of the general circulation. *Icarus* 155, 299–323. <http://dx.doi.org/10.1006/icar.2001.6757>.
- Pankine, A.A., Ingersoll, A.P., 2004. Interannual variability of Mars global dust storms: An example of self-organized criticality? *Icarus* 170, 514–518. <http://dx.doi.org/10.1016/j.icarus.2004.04.006>.
- Rafkin, S.C.R., 2012. The potential importance of non-local, deep transport on the energetics, momentum, chemistry, and aerosol distributions in the atmospheres of Earth, Mars, and Titan. *Planet. Space Sci.* 60, 147–154.
- Rafkin, S.C.R., Maria, M.R.V., Sta, M., Michaels, T.I., 2002. Simulation of the atmospheric thermal circulation of a martian volcano using a mesoscale numerical model. *Nature* 419, 697–699. <http://dx.doi.org/10.1038/nature01114>.
- Renno, N.O., Burkett, M.L., Larkin, M.P., 1998. A simple thermodynamical theory for dust devils. *J. Atmos. Sci.* 55, 3244–3252.
- Richardson, M.I., 1998. Comparison of microwave and infrared measurements of martian atmospheric temperatures: Implications for short-term climate variability. *J. Geophys. Res.* 103 (E3), 5911–5918. <http://dx.doi.org/10.1029/97JE03372>.
- Richardson, M.I., Toigo, A.D., Newman, C.E., 2007. PlanetWRF: A general purpose, local to global numerical model for planetary atmospheric and climate dynamics. *J. Geophys. Res.: Planets* 112, E09001. <http://dx.doi.org/10.1029/2006JE002825>.
- Rossow, W.B., 1978. Cloud microphysics: Analysis of the clouds of Earth, Venus, Mars and Jupiter. *Icarus* 36, 1–50.
- Ruff, S.W., Christensen, P.R., 2002. Bright and dark regions on Mars: Particle size and mineralogical characteristics based on Thermal Emission Spectrometer data. *J. Geophys. Res.* 107 (E12), 5127. <http://dx.doi.org/10.1029/2001JE001580>.
- Schneider, E.K., 1983. Martian great dust storms: Interpretive axially symmetric models. *Icarus* 55, 302–331. [http://dx.doi.org/10.1016/0019-1035\(83\)90084-2](http://dx.doi.org/10.1016/0019-1035(83)90084-2).
- Shin, H.H., Hong, S.-Y., Dudhia, J., 2012. Impacts of the lowest model level height on the performance of planetary boundary layer parameterizations. *Mon. Weather Rev.* 140, 664–682. <http://dx.doi.org/10.1175/MWR-D-11-00027.1>.
- Skamarock, W.C. et al., 2008. A Description of the Advanced Research WRF Version 3. NCAR Tech. Rep. TN-4751STR. 113pp.
- Smith, M.D., 2004. Interannual variability in TES atmospheric observations of Mars during 1999–2003. *Icarus* 167, 148–165. <http://dx.doi.org/10.1016/j.icarus.2003.09.010>.
- Smith, M.D., 2009. THEMIS observations of Mars aerosol optical depth from 2002–2008. *Icarus* 202, 444–452. <http://dx.doi.org/10.1016/j.icarus.2009.03.027>.
- Sorbjan, Z., Wolff, M., Smith, M.D., 2009. Thermal structure of the atmospheric boundary layer on Mars based on Mini-TES observations. *Q. J. R. Meteorol. Soc.* 135 (644), 1776–1787. <http://dx.doi.org/10.1002/qj.510>.
- Strausberg, M.J. et al., 2005. Observations of the initiation and evolution of the 2001 Mars global dust storm. *J. Geophys. Res.* 110, E02006. <http://dx.doi.org/10.1029/2004JE002361>.
- Szwast, M.A., Richardson, M.I., Vasavada, A.R., 2006. Surface dust redistribution on Mars as observed by the Mars Global Surveyor and Viking Orbiters. *J. Geophys. Res.* 111, E11008. <http://dx.doi.org/10.1029/2005JE002485>.
- Toigo, A.D. et al., 2012. The impact of resolution on the dynamics of the martian global atmosphere: Varying resolution studies with the MarsWRF GCM. *Icarus* 221 (1), 276–288. <http://dx.doi.org/10.1016/j.icarus.2012.07.020>.
- Wang, H., Richardson, M.I., 2013. The origin, evolution, and trajectory of large dust storms on Mars during Mars years 24–30 (1999–2011). *Icarus*. <http://dx.doi.org/10.1016/j.icarus.2013.10.033>.
- Wang, H. et al., 2003. Cyclones, tides, and the origin of a cross-equatorial dust storm on Mars. *Geophys. Res. Lett.* 30 (9), 1488. <http://dx.doi.org/10.1029/2002GL16828>.
- Wang, H., Zurek, R.W., Richardson, M.I., 2005. Relationship between frontal dust storms and transient eddy activity in the northern hemisphere of Mars as observed by Mars Global Surveyor. *J. Geophys. Res.* 110, E07005. <http://dx.doi.org/10.1029/2005JE002423>.
- White, B.R., 1979. Soil transport by wind on Mars. *J. Geophys. Res.* 84, 4643–4651.
- Wilson, R.J., 2011. Dust cycle modeling with the GFDL Mars General Circulation Model. In: 4th International Workshop on the Mars Atmosphere: Modeling and Observations, Paris. <http://www-mars.lmd.jussieu.fr/paris2011/abstracts/wilson_rj3_paris2011.pdf>.
- Wilson, R.J., Hamilton, K.P., 1996. Comprehensive model simulation of thermal tides in the martian atmosphere. *J. Atmos. Sci.* 53, 1290–1326.
- Wilson, R.J., Kahre, M.A., 2009. The role of spatially variable surface dust in GCM simulations of the martian dust cycle. In: Mars Dust Cycle Workshop, Mountain View, CA, pp. 108–112. <http://spacescience.arc.nasa.gov/mars-climate-modeling-group/documents/mars_dust_cycle_workshop_abstracts.pdf>.
- Wilson, R.J., Richardson, M.I., 2000. The martian atmosphere during the Viking mission, 1. Infrared measurements of atmospheric temperatures revisited. *Icarus* 145, 555–579.
- Wilson, R.J., Lewis, S.R., Montabone, L., 2008. Influence of water ice clouds on martian tropical atmospheric temperatures. *Geophys. Res. Lett.* 35, L07202.
- Wolff, M.J., Clancy, R.T., 2003. Constraints on the size of martian aerosols from Thermal Emission Spectrometer observations. *J. Geophys. Res.* 108 (E9), 5097. <http://dx.doi.org/10.1029/2003JE002057>.